

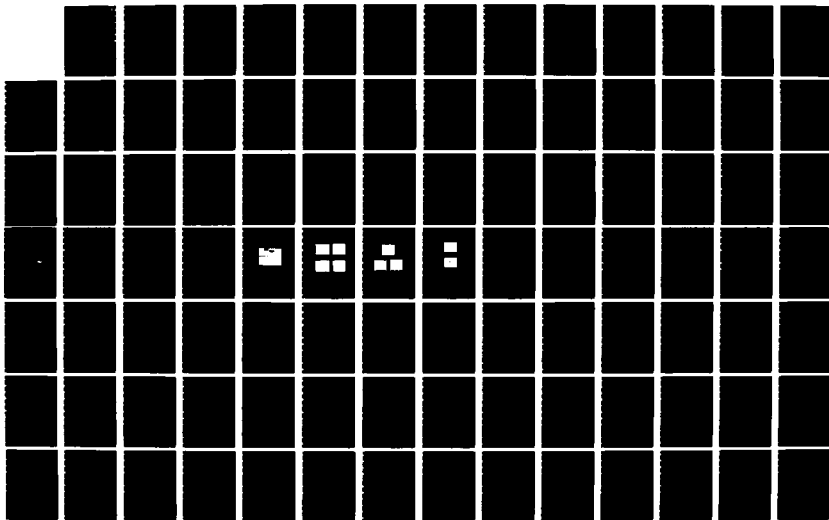
98-0772 THEORETICAL AND EXPERIMENTAL STUDIES TO DEVELOP A
PIEZOELECTRIC SHEAR STR. (U) SRI INTERNATIONAL MENLO
PARK CA Y N GUPTA ET AL 31 AUG 84 DNA-TR-84-342

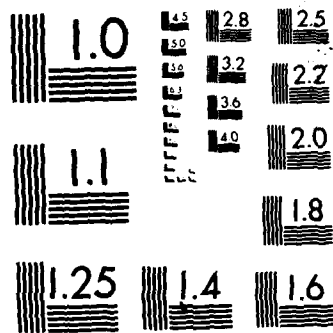
1/2

UNCLASSIFIED DNA001-80-C-0145

F/G 9/5

NL





MICROCOPY RESOLUTION TEST CHART
NATIONAL BUREAU OF STANDARDS 1963-A

AD-A172 414

12

DNA-TR-84-342

THEORETICAL AND EXPERIMENTAL STUDIES TO DEVELOP A PIEZOELECTRIC SHEAR STRESS INTERFACE GAGE

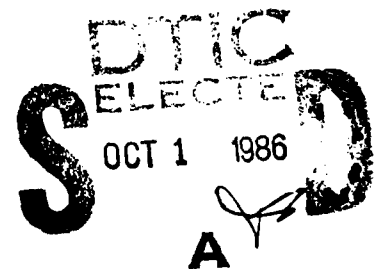
Y. M. Gupta
SRI International
333 Ravenswood Avenue
Menlo Park, CA 94025-3434

31 August 1984

Technical Report

CONTRACT Nos. DNA 001-80-C-0145
DNA 001-82-C-0297

Approved for public release;
distribution is unlimited.



THIS WORK WAS SPONSORED BY THE DEFENSE NUCLEAR AGENCY
UNDER RDT&E RMSS CODES B344080462 H53BAXYX93814 H2590D
AND B344082466 Y99QAXSD00034 H2590D.

DTIC FILE COPY

Prepared for
Director
DEFENSE NUCLEAR AGENCY
Washington, DC 20305-1000

86

255

DISTRIBUTION LIST UPDATE

This mailer is provided to enable DNA to maintain current distribution lists for reports. We would appreciate your providing the requested information.

- Add the individual listed to your distribution list.
- Delete the cited organization/individual.
- Change of address.

NAME: _____

ORGANIZATION: _____

OLD ADDRESS

CURRENT ADDRESS

TELEPHONE NUMBER: () _____

SUBJECT AREA(S) OF INTEREST:

DNA OR OTHER GOVERNMENT CONTRACT NUMBER: _____

CERTIFICATION OF NEED-TO-KNOW BY GOVERNMENT SPONSOR (if other than DNA):

SPONSORING ORGANIZATION: _____

CONTRACTING OFFICER OR REPRESENTATIVE: _____

SIGNATURE: _____

UNCLASSIFIED

SECURITY CLASSIFICATION OF THIS PAGE

AD-A112414
REPORT DOCUMENTATION PAGE

1a. REPORT SECURITY CLASSIFICATION UNCLASSIFIED		1b. RESTRICTIVE MARKINGS	
2a. SECURITY CLASSIFICATION AUTHORITY N/A since UNCLASSIFIED		3. DISTRIBUTION/AVAILABILITY OF REPORT Approved for public release; distribution is unlimited.	
2b. DECLASSIFICATION/DOWNGRADING SCHEDULE N/A since UNCLASSIFIED			
4. PERFORMING ORGANIZATION REPORT NUMBER(S) PYU-1766 and PYU-4680		5. MONITORING ORGANIZATION REPORT NUMBER(S) DNA-TR-84-342	
5a. NAME OF PERFORMING ORGANIZATION SRI International	6b. OFFICE SYMBOL (if applicable)	7a. NAME OF MONITORING ORGANIZATION Director Defense Nuclear Agency	
5c. ADDRESS (City, State, and ZIP Code) 333 Ravenswood Avenue Menlo Park, CA 94025-3434		7b. ADDRESS (City, State, and ZIP Code) Washington, DC 20305-1000	
8a. NAME OF FUNDING/SPONSORING ORGANIZATION	8b. OFFICE SYMBOL (if applicable)	9. PROCUREMENT INSTRUMENT IDENTIFICATION NUMBER DNA 001-80-C-0145 and DNA 001-82-C-0297	
9c. ADDRESS (City, State, and ZIP Code)		10. SOURCE OF FUNDING NUMBERS	
		PROGRAM ELEMENT NO. 62715H 62715H	PROJECT NO H53BAXY Y99QAXS
		TASK NO X D	WORK UNIT ACCESSION NO DH004745 DH004745
11. TITLE (Include Security Classification) THEORETICAL AND EXPERIMENTAL STUDIES TO DEVELOP A PIEZOELECTRIC SHEAR STRESS INTERFACE GAGE			
12. PERSONAL AUTHOR(S) Gupta, Y. M.; Contributors: Murri, W.J. and Aidun, J.B.			
13a. TYPE OF REPORT Technical	13b. TIME COVERED FROM 800101 TO 840830	14. DATE OF REPORT (Year, Month, Day) 840831	15. PAGE COUNT 142
16. SUPPLEMENTARY NOTATION This work was sponsored by the Defense Nuclear Agency under RDT&E RMSS Codes B344080462 H53BAXYX93814 H2590D and B344082466 Y99QAXSD00034 H2590D.			
17. COSATI CODES		18. SUBJECT TERMS (Continue on reverse if necessary and identify by block number)	
FIELD	GROUP	SUB-GROUP	
20	14	-	Shear Stress Gage
14	03	-	Impact Response
			Piezoelectric Analysis <i>doc</i>
			Piezoelectric Measurements
			Dynamic Loading
			Wave Propagation
19. ABSTRACT (Continue on reverse if necessary and identify by block number) Theoretical developments to analyze the impact response of rotated-cut piezoelectric gages are presented. Requirements for an ideal shear gage are outlined, and a theoretical framework to incorporate more realistic response is developed. Impact experiments to determine the current output from 163°- and 165.5°-rotated Y-cut shorted LiNbO ₃ gages have been performed. The experimental results show that the 163° Y-cut orientation is more sensitive to shear than compression and has no cross-axis shear sensitivity. As expected, the compression response is higher for the 165.5° Y-cut orientation. Experimental results suggest the importance of accounting for the effects of anisotropy, impact tilt, and minor variations in the orientations of the crystals. In detailed comparisons of theory and experiment, these effects were included. These comparisons showed that for shear loading the agreement between theory and experiment is good (within 3 percent); for compression loading the agreement is only to within 10 to 15 percent. An accurate determination of the			
20. DISTRIBUTION AVAILABILITY OF ABSTRACT <input type="checkbox"/> UNCLASSIFIED/UNLIMITED <input checked="" type="checkbox"/> SAME AS RPT <input type="checkbox"/> DPC USERS		21. ABSTRACT SECURITY CLASSIFICATION UNCLASSIFIED	
22a. NAME OF RESPONSIBLE INDIVIDUAL Betty L. Fox		22b. TELEPHONE (include Area Code) (202) 325-7042	22c. OFFICE SYMBOL DNA/STTI

DD FORM 1473, 34 MAR

33 APR edition may be used until exhausted
All other editions are obsolete

SECURITY CLASSIFICATION OF THIS PAGE

UNCLASSIFIED

UNCLASSIFIED

10-20-50

SECURITY CLASSIFICATION OF THIS PAGE

19. ABSTRACT (Concluded)

piezoelectric constant e_{22} and the elastic constant C_{12}^D , with precise measurements of the orientation of crystals to be used in the experiments, is needed before drawing further conclusions about the causes for the disagreement between theory and experiment. Specific recommendations for future theoretical and experimental efforts are suggested.

SEARCHED
SERIALIZED
INDEXED
FILED

By _____
Distribution _____
Availability _____
Dist _____

AI



UNCLASSIFIED
SECURITY CLASSIFICATION OF THIS PAGE

SUMMARY

The ability to make dynamic shear stress measurements is an important need in both laboratory and fielding applications. In a preliminary study, the feasibility of developing a piezoelectric shear stress gage that would be insensitive to compressive stresses was demonstrated. The objectives of the present work were to perform detailed analyses to understand the response of such a gage, perform laboratory calibration experiments, and check cross-axis shear effects, all as an intermediate step for developing a gage package for field use. Because the piezoelectric constants are important in determining the optimal gage orientation, a related objective was to verify the constants reported in the literature.

To meet these objectives, theoretical analyses and laboratory experiments were performed. Impact experiments, designed to provide temporal separation between the compression and shear response of the gage, were performed on 163°- and 165.5°-rotated Y-cut Lithium Niobate (LiNbO_3) gages. The 163° Y-cut orientation was chosen because it is the optimal orientation for shear-stress-induced response based on the existing set of piezoelectric constants. The 165.5° Y-cut orientation is a specific direction and provides a uniaxial strain response under compression-only loading.

The experimental results showed that the 163° Y-cut orientation is considerably more sensitive to shear loading than to compressive loading. Also, the 163° Y-cut orientation appears to be insensitive to cross-axis shear. The experimental results suggested that impact misalignment (or tilt) and crystalline anisotropy effects need to be taken into account in analyzing the experimental data. As expected, the 165.5° Y-cut orientation showed a considerably larger response to compression than did the 163° Y-cut orientation. The large current rise that occurs following the initial jump in current suggests the need for

modeling the effects of electromechanical coupling. Some of the experimental results showed scatter, which could be attributed to variations in tilt between experiments, minor variations in the orientations of the crystals, or both.

In analyzing the gage response, we examined only the initial jump in current to avoid complexity due to electromechanical coupling. Quantitative methods were developed to include crystalline anisotropy and impact tilt contributions because these were determined to be significant. Detailed comparisons between the experimental results and theoretical predictions were attempted. For the shear loading, the agreement between theory and experiment is good (within 3 percent). On the other hand, for compression loading theory and experiment agree only to within 10 to 50 percent; not all the differences have been resolved. Two potential sources of errors that need to be examined in future studies are the accuracy limits on the value of the piezoelectric constant e_{22} and the uncertainty in the orientation of the rotated-cut crystals. Also, the value of the elastic constant C_{12}^D needs to be established accurately. In future studies an accuracy to within $\pm 0.1^\circ$ is required. A detailed electrostatic analysis for rotated-cut crystals has been presented. To apply this analysis to experimental data requires solutions for the two-dimensional electrostatic problem. Unless this analysis is carefully applied to data on rotated-cut crystals, interpretations based on these data are suspect. Theoretical expressions describing the effects of electromechanical coupling under combined compression and shear loading are derived; however, these expressions were not used in analyzing the data. This latter task requires further numerical effort.

The present work has provided a detailed examination of the shear gage concept, and on the basis of the work described in this report, we believe that the development of the shear stress gage is a realistic undertaking. An important conclusion is that improved reconciliation between theory and experiment is necessary before developing a field gage, and this task will require further theoretical analyses and more

precise experimental work. Specific steps for future work are outlined in this report. An important change from the earlier conclusions of the feasibility study is the redefinition of the criteria for the optimal gage orientation. The sensitivity of the gage output to compression loading varies markedly with small deviations of the crystal orientation from the optimum orientation for measuring shear stress. This behavior, combined with practical limitations to the accuracy with which the crystal orientation can be determined, suggests that the crystal orientation to be used in a field gage should be chosen as a compromise between minimizing its compression sensitivity and accommodating the practical constraints of crystal orientation accuracy.

PREFACE

The work presented in this report was performed under two successive contracts, the experimental portion primarily under Contract DNA-80-C-0145 and the theoretical portion primarily under Contract DNA-82-C-0297. The reports have been combined because the analyses of the experiments depend on the theoretical development.

The program was initially monitored by Lt. Col. Eric Furbee and later monitored by Lt. Col. William Heuser.

The author is thankful to the following individuals for their contributions: Robert Graham of Sandia Laboratories is acknowledged for many helpful discussions; his considerable experience in shock-induced piezoelectric response has been useful to the author. The contribution of W. J. Murri in performing the impact experiments is acknowledged; he obtained the tilt values for each of the experiments, and B. Y. Lew helped with data reduction and the numerical work. D. Henley and D. Walter provided able technical assistance with the experiments. D. D. Keough was a source of constant encouragement and discussions with him were very helpful. J. Aidun's careful reading of the report and help with the report preparation deserve a special acknowledgement.

The author is grateful to the late Nate Brown who supplied all the crystals and whose dedication to this work was invaluable to the present effort.

The author's present address is Department of Physics, Washington State University, Pullman, WA 99164.

CONVERSION TABLE

Conversion factors for U.S. Customary to metric (SI) units of measurement

MULTIPLY $\xrightarrow{\hspace{2cm}}$ BY $\xrightarrow{\hspace{2cm}}$ TO GET
 TO GET $\xleftarrow{\hspace{2cm}}$ BY $\xleftarrow{\hspace{2cm}}$ DIVIDE

angstrom	1.000 000 X E -10	meters (m)
atmosphere (normal)	1 013 25 X E +2	kilo pascal (kPa)
bar	1 000 000 X E +2	kilo pascal (kPa)
barn	1 000 000 X E -28	meter ² (m ²)
British thermal unit (thermochemical)	1.054 350 X E +3	joule (J)
calorie (thermochemical)	4 184 000	joule (J)
cal (thermochemical) cm ²	4 184 000 X E -2	mega joule/m ² (MJ/m ²)
curie	3 700 000 X E +1	*giga becquerel (GBq)
degree (angle)	1 745 329 X E -2	radian (rad)
degree Fahrenheit	$t_c = (t_f + 459.67)/1.8$	degree kelvin (K)
electron volt	1 602 19 X E -19	joule (J)
erg	1.000 000 X E -7	joule (J)
erg/second	1.000 000 X E -7	watt (W)
foot	3 048 000 X E -1	meter (m)
foot-pound-force	1.355 818	joule (J)
gallon (U.S. liquid)	3 785 412 X E -3	meter ³ (m ³)
inch	2 540 000 X E -2	meter (m)
jerk	1 000 000 X E +9	joule (J)
joule/kilogram (J/kg) (radiation dose absorbed)	1.000 000	Gray (Gy)
kilotons	4 183	terajoules
kip (1000 lbf)	4 448 222 X E +3	newton (N)
kip/inch ² (ksi)	6 894 757 X E +3	kilo pascal (kPa)
ktap	1 000 000 X E +2	newton-second/m ² (N-s/m ²)
micron	1 000 000 X E -6	meter (m)
mil	2 540 000 X E -5	meter (m)
mile (international)	1 609 344 X E +3	meter (m)
ounce	2 934 952 X E -2	kilogram (kg)
pound-force (lbf avoirdupois)	4.448 222	newton (N)
pound-force inch	1 129 848 X E -1	newton-meter (N·m)
pound-force/inch	1 751 268 X E +2	newton-meter (N/m)
pound-force/foot ²	4 798 026 X E -2	kilo pascal (kPa)
pound-force/inch ² (psi)	6 894 757	kilo pascal (kPa)
pound-mass (lbm avoirdupois)	4 535 924 X E -1	kilogram (kg)
pound-mass-foot ² (moment of inertia)	4 214 011 X E -2	kilogram-meter ² (kg·m ²)
pound-mass/foot ³	1 601 846 X E +1	kilogram/meter ³ (kg/m ³)
rad (radiation dose absorbed)	1 000 000 X E -2	*Gray (Gy)
roentgen	2 579 760 X E -4	coulomb/kilogram (C/kg)
shake	1 000 000 X E -8	second (s)
slug	1 459 390 X E +1	kilogram (kg)
torr (mm Hg, 0° C)	1 333 22 X E -1	kilo pascal (kPa)

*The becquerel (Bq) is the SI unit of radioactivity; 1 Bq = 1 event/s
 **The Gray (Gy) is the SI unit of absorbed radiation.

TABLE OF CONTENTS

Section	Page
SUMMARY.....	iii
PREFACE.....	vi
CONVERSION TABLE.....	vii
LIST OF ILLUSTRATIONS.....	x
LIST OF TABLES.....	xi
1 INTRODUCTION.....	1
1.1 Background.....	1
1.2 Objectives and Approach.....	2
2 THEORETICAL DEVELOPMENTS.....	4
2.1 Elastic-Dielectric Analysis for Combined Compression and Shear Loading.....	5
2.2 Elastic-Dielectric Analysis for a Rotated-Cut Gage.....	10
2.3 Linear Coupled Response of a Rotated-Cut Gage to Combined Compression and Shear Loading.....	15
2.4 Implications for Experiments.....	20
3 EXPERIMENTAL METHOD AND RESULTS.....	22
3.1 Experimental Design and Method.....	22
3.2 Experimental Results.....	29
4 ANALYSIS AND DISCUSSION.....	43
4.1 Numerical Simulation of the Experiments (Mechanical Variables).....	43
4.2 Analysis of the Polarization Measurements.....	47
4.3 Assessment of Tilt Effects.....	50
4.4 Discussion.....	54
5 CONCLUSIONS AND RECOMMENDATIONS.....	57
6 LIST OF REFERENCES.....	62

TABLE OF CONTENTS (Concluded)

APPENDICES	Page
A Synopsis of the Feasibility Study.....	65
B Wave Propagation Along Nonspecific Directions.....	71
C Determination of Piezoelectric Constants for LiNbO_3	83
D Transformation of Piezoelectric Constants.....	91
E Oblique Impact of Elastic Plates.....	97
F Details of Measured Wave Profiles.....	119

LIST OF ILLUSTRATIONS

<u>Figure</u>		<u>Page</u>
1	Compression and Shear Wave Fronts in a Piezoelectric Disk.....	7
2	Schematic View of the Impact Experiment.....	25
3	The Projectile and Target Assembly Used in the Impact Experiments.....	28
4	Voltage-Time Profiles from Experiment 1 (78-2-46) with 163° Y-Cut ($Z' = 0^\circ$) LiNbO ₃ Gage.....	32
5	Voltage-Time Profiles from Experiment 2 through 8 with Rotated Y-Cut LiNbO ₃ Gages.....	33
6	Impact Closure as Seen from the Projectile Side.....	36
B.1	Free-Surface Velocity in Y-Cut Quartz Impacted by X-Cut Quartz.....	80
E.1	Experimental Configuration for Evaluating Tilt Effects....	98
E.2	Oblique Impact of Two Elastic Plates.....	100
E.3	P-Wave Interaction with the Interface.....	109
E.4	S-Wave Interaction with the Interface.....	112
F.1	Voltage-Time Profile for Experiment 1 (78-2-46).....	120
F.2	Voltage-Time Profiles for Experiment 2 (81-2-15).....	121
F.3	Current-Time Profiles for Experiment 3 (81-2-22).....	122
F.4	Current-Time Profiles for Experiment 4 (81-2-23).....	123
F.5	Current-Time Profiles for Experiment 6 (81-2-43).....	124

LIST OF TABLES

<u>Table</u>		<u>Page</u>
1	Details of LiNbO ₃ gages.....	23
2	Summary of impact experiments.....	30
3	Numerical simulation of LiNbO ₃ experiments using C _{ij} ^D from reference 5.....	44
4	Numerical simulation of LiNbO ₃ experiments using C _{ij} ^D from reference 4.....	46
5	Comparison of polarization values.....	48
6	Tilt contribution to polarization.....	53
B-1	Elastic constants at constant displacement.....	82
C-1	Second-order piezoelectric stress constants.....	84
C-2	Numerical simulation of Graham's LiNbO ₃ data.....	87
D-1	Transformed piezoelectric constants for rotated Y-cut LiNbO ₃ (old set).....	95
D-2	Transformed piezoelectric constants for rotated Y-cut LiNbO ₃ (new set).....	96

SECTION 1

INTRODUCTION

1.1 BACKGROUND

The measurement of dynamic stresses and loads is an important aspect of the DNA experimental effort. Many different types of transducers have been developed and are in use in both laboratory and field programs. Proceedings of a recent DNA conference describe the status of instrumentation currently in use.¹ The development of a shear stress transducer for dynamic measurements is recognized as an important need by workers associated with dynamic load measurements.

In 1978, we proposed the idea of developing a piezoelectric shear stress gage that would be insensitive to compressive stresses. A small effort was undertaken to determine the feasibility of developing such a gage.² Theoretical conditions for developing the desired gage were formulated and quantified, and idealized mathematical relations were derived for using this gage. The analytic work indicated that of the various orientations in alpha quartz and lithium niobate (LiNbO_3) only the 163° -rotated Y-cut orientation* appeared to be suitable for use as a shear gage. Experiments were performed to confirm that the gage had a high sensitivity to shear stresses and a low sensitivity to compressive stresses. Although this work was mostly qualitative, it demonstrated the theoretical and experimental feasibility of developing a piezoelectric shear gage. For readers not familiar with the feasibility study,² a synopsis of the past work is presented in Appendix A. A brief background pertinent to the feasibility study is also included in this synopsis.

*We are using the Institute of Radio Engineers (IRE) nomenclature,³ which is recommended for piezoelectric crystals. Rotated Y-cut orientation denotes rotation about the crystallographic X-axis.

1.2 OBJECTIVES AND APPROACH

The objectives of the present effort* were to perform more detailed theoretical calculations to better understand the gage response, perform laboratory experiments to calibrate both the compression and shear response of the gage, check cross-axis shear effects, estimate uncertainties in gage measurements, and suggest guidelines for developing a gage package for field use. The present work was envisioned as a detailed examination of the shear gage concept and an intermediate step toward developing a field gage package. Because of the extensive characterization of LiNbO_3 both in ultrasonics^{4,5} and in compressive shock wave experiments,⁶ no serious problems were anticipated.† Although the objectives of these earlier ultrasonic and shock wave measurements were different from our current objectives, we felt that the fundamental constants of LiNbO_3 were sufficiently well known to permit a straightforward calibration. The experimental effort was to provide a quantitative check for our initial ideas. As discovered during our work, not all of fundamental material constants (elastic and piezoelectric) are known with sufficient accuracy.

For our laboratory experiments, we chose two orientations: 163° Y-cut and 165.5° Y-cut. The 163° Y-cut was chosen as the optimal direction for a shear stress gage. The 165.5° Y-cut orientation was chosen because it is a "specific direction"‡ and theoretical analysis is easier for this orientation. The 165.5° Y-cut orientation was also intended to confirm the piezoelectric constants reported in the literature.⁴⁻⁶ We felt that this conformation would be useful because

*Discussions with AFWL personnel were helpful in determining the field requirements for a shear stress gage.

†As described in Reference 6, rotated-cut gage data under compression had also been analyzed.

‡A direction in which propagated waves are purely longitudinal or purely transverse is a specific direction. Also see Appendix B.

the optimal orientation for the shear gage is sensitive to the value of these constants.

The theoretical work was intended to extend the analysis presented in our feasibility study to provide sufficiently accurate quantitative interpretation of our experimental data. A secondary objective of the theoretical effort was to identify additional analyses that might be important for the subsequent effort of developing a field gage package.

The approach we used in this project had one main theme: to work out as many of the quantitative details about the gage response as possible to minimize ambiguities and difficulties with data interpretation once the gage is used in field experiments. In most applications the gage will be subjected to complex loading. This fact, coupled with the fact that compressive loads are considerably higher than shear loads in most applications, requires that the gage response be well understood. Hence, it is necessary that in well-defined laboratory experiments the gage response be modeled quantitatively.

The remainder of the report consists of four sections and several appendices. Readers desiring an overview of this work should read Appendix A, the first few pages of Section 2, the Summary at the end of Section 3, Section 4.4, and Section 5. The experimental work is described in Section 3 and Appendix F. Readers interested in the theoretical developments and analysis should read Sections 2 and 4 and Appendices B, C, D, and E.

SECTION 2

THEORETICAL DEVELOPMENTS

In this section we present theoretical analyses describing compression and shear wave propagation in piezoelectric crystals and develop criteria for selecting the optimal gage design. The first theoretical analysis is an idealized calculation that indicates the requirements for an ideal shear gage. After identifying these requirements, we present two, more general, theoretical analyses that consider conditions that are closer to those for a real shear gage. Although these two analyses have not been fully used in the present work because of their complexity, they provide considerable insight into the gage response. Numerical methods to implement these general analyses should be considered in future studies.

Since Nielson's initial derivation of the expressions for the short-circuit current for a quartz gage,⁷ Graham and others at Sandia Laboratories have performed an extensive series of studies on the response of piezoelectric gages subjected to dynamic uniaxial strain loading.⁸⁻¹³ Their papers demonstrate the extensive developments in both theory and experiment over the past 20 years. In contrast to α -quartz the behavior of LiNbO_3 is considerably more complex and requires a careful understanding of the electromechanical coupling, which is discussed in Section 3 of Reference 6. The papers by Chen et al.¹⁴ and Lawrence and Davison¹⁵ are important contributions to this problem.

Despite the many developments over the past two decades, two features are common to all the studies cited above: the condition of uniaxial strain and the assumption of coincidence of the electric fields with the gage thickness direction (also the wave propagation direction). These restrictions, although reasonable for the earlier work, are not valid for analyzing the shear gage response.

All the theoretical analyses presented here assume that the gage material is elastic and has zero conductivity. In addition, all the dependent variables are assumed to have a one-dimensional variation. This last assumption is questionable for the electrical variables in certain situations, as discussed later.

2.1 ELASTIC-DIELECTRIC ANALYSIS FOR COMBINED COMPRESSION AND SHEAR LOADING

Expressions describing the response of an idealized gage are obtained by extending the elastic-dielectric analysis for uniaxial strain¹⁶ to combined compression and shear loading. We make the following assumptions: (1) the gage thickness direction is a specific direction, (2) there is no electromechanical coupling, (3) finite strain and nonlinear electrical effects can be neglected, (4) the electrical permittivity tensor has only diagonal elements* and their variations with strain can be neglected, and (5) the electrical fields are parallel to the gage thickness direction.

With these assumptions, we consider the propagation of a compression and a shear wave through the gage as shown in Figure 1. Region I is unstressed, Region II has undergone compressive deformation, and Region III has undergone compressive and shear deformation. The two faces of the gage are short-circuited through a low resistance to measure the current due to gage deformation. The thicknesses of each of these regions and the electrical variables for the three regions are indicated in Figure 1. Because there is no free charge (i.e., the gage has zero conductivity), the gradient of the displacement field \vec{D} is zero.¹⁷

$$\frac{\partial D_2}{\partial X_2} = 0 \quad (2-1)$$

*This assumption although not explicitly stated, has been made in past work.

where X_2 is the coordinate through the gage thickness; the gage is assumed to be infinite along the other two directions. Equation (2-1) shows that D_2 is only a function of time t , and at any instant we can write

$${}^{(1)}D_2 = {}^{(2)}D_2 = {}^{(3)}D_2 \quad (2-2)$$

Writing this in terms of polarization, \vec{P} , and electric field, \vec{E} , we have

$${}^{(1)}\epsilon {}^{(1)}E_2 = {}^{(2)}\epsilon {}^{(2)}E_2 + {}^{(2)}P_2 = {}^{(3)}\epsilon {}^{(3)}E_2 + {}^{(3)}P_2 \quad (2-3)$$

where ${}^{(i)}\epsilon$ is the permittivity in the i^{th} region. The short-circuit condition is given by

$$\int_0^{\lambda} E_2 dX_2 = {}^{(1)}E_2 \lambda_1 + {}^{(2)}E_2 \lambda_2 + {}^{(3)}E_2 \lambda_3 = 0 \quad (2-4)$$

At any instant the thickness λ_1 , λ_2 , λ_3 can be expressed in terms of the total thickness λ and the wave velocities:

$${}^{(1)}E_2(\lambda - U_c t) + {}^{(2)}E_2(U_c - U_s)t + {}^{(3)}E_2 U_s t = 0 \quad (2-5)$$

where the subscripts "c" and "s" refer to the compression and the shear wave, respectively. Because we are considering infinitesimal strains, we take ${}^{(1)}\epsilon = {}^{(2)}\epsilon = {}^{(3)}\epsilon$ and use equation (2-5) with equation (2-3) to eliminate ${}^{(2)}E_2$ and ${}^{(3)}E_2$. We can then write

$${}^{(1)}D_2 = \epsilon {}^{(1)}E_2 = \frac{1}{\lambda} [{}^{(2)}P_2(U_s - U_c)t + {}^{(3)}P_2 U_s t] \quad (2-6)$$

The current in the external circuit is written as

$$i = A \frac{dD_2}{dt} = \frac{A}{\lambda} [{}^{(2)}P_2 U_c + U_s ({}^{(3)}P_2 - {}^{(2)}P_2)] \quad (2-7)$$

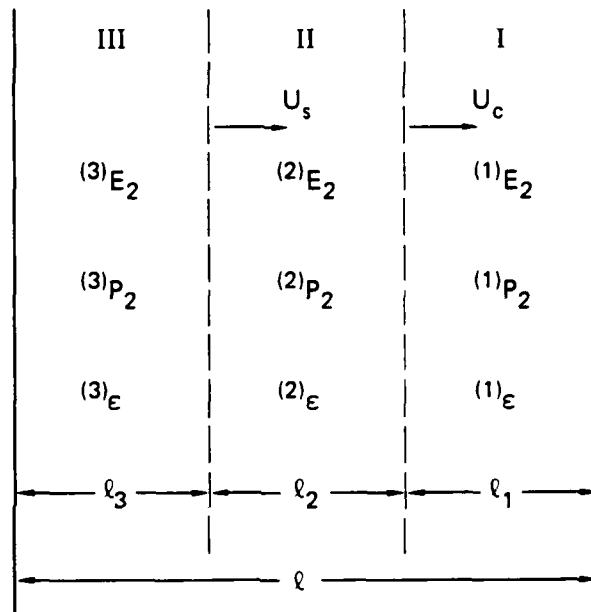


Figure 1. Compression and shear wave fronts in a piezoelectric disk. [The wave velocities U_c and U_s and the electrical variables in the three regions are shown. The gage thickness direction is X_2 (or X'_2) as explained in the text. The polarization in region I is zero.]

where A is the area of the electrode. In equation (2-7), $^{(2)}P_2$ is the polarization due to the compressive wave only, but $^{(3)}P_2$ is the polarization due to both waves. Rewriting equation (2-7), we have

$$i = \frac{A}{\lambda} [P_c U_c + P_s U_s] \quad (2-8)$$

The polarization is related to the mechanical strains (in the gage) through the relation¹⁸

$$P_i = e_{ijk} \epsilon_{jk} \quad (2-9)$$

If X_2 is the wave propagation direction and the direction of shear loading is X_3 , we can rewrite equation (2-9), in the matrix notation, in Region III as

$$^{(3)}P_2 = P_c + P_s = e_{22} \epsilon_2 + e_{24} \epsilon_4 \quad (2-10)$$

In equation (2-10) and throughout the report, we follow the commonly used convention for equivalence of the subscripts in matrix and tensor notation:

<u>Stress Convention</u>	<u>Strain Convention</u>	<u>Piezoelectric Constant Convention (i = 1 to 3)</u>
$\sigma_1 = \sigma_{11}$	$\epsilon_1 = \epsilon_{11}$	$e_{11} = e_{111}$
$\sigma_2 = \sigma_{22}$	$\epsilon_2 = \epsilon_{22}$	$e_{12} = e_{122}$
$\sigma_3 = \sigma_{33}$	$\epsilon_3 = \epsilon_{33}$	$e_{13} = e_{133}$
$\sigma_4 = \sigma_{23} = \sigma_{32}$	$\epsilon_4 = 2 \epsilon_{23} = 2 \epsilon_{32}$	$e_{14} = e_{123} = e_{132}$
$\sigma_5 = \sigma_{13} = \sigma_{31}$	$\epsilon_5 = 2 \epsilon_{13} = 2 \epsilon_{31}$	$e_{15} = e_{113} = e_{131}$
$\sigma_6 = \sigma_{12} = \sigma_{21}$	$\epsilon_6 = 2 \epsilon_{12} = 2 \epsilon_{21}$	$e_{16} = e_{112} = e_{121}$

Substituting equation (2-10) into equation (2-8), we can write

$$i = \frac{A}{\lambda} [U_c e_{22} \epsilon_2 + U_s e_{24} \epsilon_4] \quad (2-11)$$

Equation (2-11) can be used to discuss the criteria for selecting a gage subjected to combined compression and shear loading. For a gage sensitive only to normal strains, e_{24} should be zero. In contrast, an ideal shear gage should have $e_{22} = 0$. To satisfy these conditions, we need to consider rotated cuts for the crystals.

We choose the following notation to avoid confusion with the axes used in the crystallographic system: X_2' defines the direction of wave propagation, X_3' is the direction of the imposed shear motion, and X_1' is chosen such that X_1' -axes form a right-handed coordinate system. Hence, an important requirement for an ideal shear gage is that $e_{22}' = 0$ and e_{24}' be large. For the most general case, we have shear along the X_1' - and X_3' -axes. For an ideal gage there should be no cross-axis shear effect and $e_{26}' = 0$. For the situation shown in Figure 1, the current output can then be uniquely related to the shear strain in the gage. The use of this idealized gage would be analogous to the piezoelectric compression gage.

Having established the main criterion for the shear gage, we now examine the various assumptions made in deriving equation (2-11). Of the five assumptions listed earlier, the most important one is the need for the wave propagation direction to be a specific direction¹⁹ with regard to both compression and shear waves (see Appendix B). If the direction of wave propagation is not a specific direction, the various strains (or stresses) in the gage will be coupled, all three strains (ϵ_2' , ϵ_4' , ϵ_6') will be produced, and the polarization can have several contributions.

Thus, the two most important criteria for the shear gage are as follows: (1) the electrical polarization is caused only by the shear strain (or stress) of interest and (2) the gage thickness direction is a specific direction. In the earlier feasibility study,² these criteria were used to examine both α -quartz and lithium niobate crystals. Only the 163° Y-cut orientation of LiNbO_3 approached optimal conditions (see Appendix D). For this orientation, using the constants cited in the literature,⁴⁻⁶ we find that the ratio e_{24}'/e_{22}' is 470. Although this

direction is not a specific direction, it is close to the specific direction (165.5° Y-cut, see Appendix B). The particle motion, for wave propagation along the 163° Y-cut in LiNbO_3 , is along the 161.7° Y-cut direction. Hence, the mechanical coupling of the strains due to crystal anisotropy was expected to be small.

Note that the values cited above were based on the values for elastic constants (C_{ij}^D) and piezoelectric constants (e_{ijk}) for LiNbO_3 cited in the literature. The extreme sensitivity of the ratio e'_{24}/e'_{22} to the crystal orientation* requires that both the e_{ijk} values and the crystal orientation be known very accurately. During the work described in this report, we discovered that the values cited in the literature were incorrect. We have reanalyzed past shock wave data for LiNbO_3 ⁶ to determine the "correct" values (see Appendix C).†

In the present work we also found that small deviations from the specific direction and the effects of impact tilt need to be included for analysis of experimental data. Analytic methods to incorporate these effects are described in Appendices B and E.

In the next two subsections, we present more general theoretical developments that are closer to the conditions of the experiments.

2.2 ELASTIC-DIELECTRIC ANALYSIS FOR A ROTATED-CUT GAGE

In this subsection, we restrict ourselves to only two assumptions: (1) electromechanical coupling is not considered and (2) finite strain and nonlinear electrical effects are neglected. The first assumption is relaxed in the next subsection. Eliminating the second assumption does not pose any conceptual problems, but makes the analysis

*The ratio e'_{24}/e'_{22} for 162° Y-cut is -28.8 and the ratio e'_{24}/e'_{22} for 164° Y-cut is 25.9 . Note, e_{24} is nearly constant, but the e_{22} value changes dramatically with orientation.

†This question has not been resolved satisfactorily.

more complicated. For the small strains considered in our work, the second assumption is reasonable.

Because we are not considering wave propagation in a specific direction, each of the Regions II and III in Figure 1 will have both compressive and shear deformations. In general, there will be three regions; however, to simplify the algebra, we initially consider only two regions: an unstressed region, Region I, and a region undergoing both compressive and shear deformation, Region II. Thus, Region II in this analysis is similar to Region III of Figure 1. Extending this analysis to three regions is straightforward and the final expressions are presented. The two-region situation arises when a quasi-longitudinal wave propagates in the crystal; this situation is encountered in many of our experiments described in Section 3. Below we derive the equations for a rotated Y-cut crystal of LiNbO_3 with the X_2' -axis defined to be the wave propagation direction in Figure 1.

Proceeding as before, the absence of free charge in the crystal provides

$$\frac{\partial D_2'}{\partial X_2'} = 0 \quad ; \quad (1)_{D_2'} = (2)_{D_2'} \quad (2-12)$$

Thus, D_2' is only a function of time. Writing equation (2-12) in terms of \vec{P} and \vec{E} does not produce equation (2-3) as before because for rotated Y-cut LiNbO_3 crystals the permittivity tensor has the form

$$\epsilon'_{ij} = \begin{bmatrix} \epsilon_{11} & 0 & 0 \\ 0 & \cos^2\theta\epsilon_{22} + \sin^2\theta\epsilon_{33} & \frac{\sin 2\theta}{2}(\epsilon_{33} - \epsilon_{22}) \\ 0 & \frac{\sin 2\theta}{2}(\epsilon_{33} - \epsilon_{22}) & \cos^2\theta\epsilon_{33} + \sin^2\theta\epsilon_{22} \end{bmatrix} \quad (2-13)$$

where θ is the angle of rotation about the X_1 -axis. It is the non-diagonal form of the permittivity tensor that introduces most of the complexities in the analysis of these rotated-cut crystals. Using the form of ϵ_{ij} in equation (2-13), we can rewrite equation (2-12) as

$$\begin{aligned} (1)P_2' + (1)\epsilon_{22}' (1)E_2' + (1)\epsilon_{23}' (1)E_3' = (2)P_2' + (2)\epsilon_{22}' (2)E_2' \\ + (2)\epsilon_{23}' (2)E_3' \end{aligned} \quad (2-14)$$

In the unstressed region, the polarization $(1)P_2'$ is zero. In accordance with assumption (2) above, we neglect changes in the permittivity due to small strains. The continuity of the tangential component of the \vec{E} field across the wave front gives

$$(1)E_3' = (2)E_3' \quad (2-15)$$

Equation (2-14) can now be solved to give

$$(2)E_2' = (1)E_2' - \frac{(2)P_2'}{\epsilon_{22}'} \quad (2-16)$$

The short-circuit condition across the electrodes on the gage faces is written as

$$\int_0^{\ell'} E_2' dx_2' = (1)E_2' \ell_1' + (2)E_2' \ell_2' = 0 \quad (2-17)$$

Solving equations (2-16) and (2-17) gives

$$(1)E_2' = \frac{(2)P_2' \ell_2'}{\ell' \epsilon_{22}'} \quad (2-18a)$$

$$(2)E_2' = - \frac{(2)P_2' \ell_1'}{\ell' \epsilon_{22}'} \quad (2-18b)$$

In the small strain approximation, we are neglecting particle velocity u_2' in comparison with the wave velocity U_c' , and we can write

$$\lambda_1' = \lambda' - U_c' t \quad \text{and} \quad \lambda_2' = U_c' t \quad (2-19)$$

Here the subscript "c" refers to the quasi-longitudinal wave. From equation (2-17) we see that the electric fields depend on the external circuit condition; equation (2-19) shows that they are strongly time-dependent. Combining equations (2-18) and (2-19), we can write

$${}^{(1)}D_2' = \frac{{}^{(2)}P_2' U_c' t}{\lambda'} + \epsilon_{23}' {}^{(1)}E_3' \quad (2-20)$$

Note, in contrast to equation (2-6), the displacement field in the gage thickness direction depends on the electric field along the X_3' -direction. The current in the external circuit is the displacement current, which is given by

$$i = A \frac{dD_2'}{dt} = \frac{A}{\lambda'} [{}^{(2)}P_2' U_c' + \lambda' \epsilon_{23}' \dot{{}^{(1)}E_3'}] \quad (2-21)$$

where the dot denotes a time derivative. We write the expression for current as

$$i = \frac{{}^{(2)}P_2' A U_c'}{\lambda'} + i_E \quad (2-22)$$

where the current $i_E = A \epsilon_{23}' \dot{{}^{(1)}E_3'}$. For a rotated Y-cut LiNbO_3 crystal the only nonzero strain components are ϵ_2' , ϵ_4' , and ϵ_6' . Hence, the expression for polarization along the X_2' -direction is given by

$${}^{(2)}P_2' = e_{22}' \epsilon_2' + e_{24}' \epsilon_4' + e_{26}' \epsilon_6' \quad (2-23)$$

It can be shown that, for a rotated Y-cut LiNbO_3 crystal, the constant $e_{26}' = 0$. Hence, the last term on the right side of equation (2-23) is zero. Substituting equation (2-23) in (2-22) produces

$$i = \frac{AU'_c}{\lambda'} [e'_{22} \epsilon'_2 + e'_{24} \epsilon'_4] + i_E \quad (2-24)$$

From equation (2-24) we see that, in the approximation of no electro-mechanical coupling, except for i_E , the current produced by wave propagation in a nonspecific direction is similar in form to the previous derivation in Section 2.2. The simpler relationship holds for Y-cut LiNbO_3 crystals; the term i_E is zero because ϵ'_{ij} only has diagonal terms.

To determine the effect of $^{(2)}\epsilon'_3$ on the current in equation (2-21) is an involved problem.* It will depend on the electrical boundary condition along the X'_3 -direction. For a truly infinite disk, this term will not contribute. However, for a finite disk, the shunted and shorted gages may show markedly different behavior. Further analysis of this problem requires a two-dimensional electrostatic analysis and is not attempted here. In future work this issue needs to be carefully examined.

For Y-cut and rotated Y-cut LiNbO_3 crystals there is an additional factor influencing $^{(2)}\epsilon'_3$ and i_E . For these orientations there is also a nonzero polarization in the X'_3 -direction, even for compression-only loading. This polarization may alter the electrical boundary condition. Thus its magnitude is also needed to solve the electrostatic problem to determine $^{(2)}\epsilon'_3$.

If we consider three regions[†] as shown in Figure 1, we can write

$$\lambda'_1 = \lambda' - U'_c t \quad ; \quad \lambda'_2 = (U'_c - U'_s) t \quad ; \quad \lambda'_3 = U'_s t \quad (2-25)$$

*Discussions with Mr. R. A. Graham of Sandia National Laboratory on this problem have been helpful.

†The most general case would have four regions because there will be two quasi-shear waves. For the present problem, one quasi-shear wave is sufficient.

Here, U'_c and U'_s are the wave velocities of the quasi-longitudinal and quasi-shear wave, respectively. Proceeding as before, the displacement field can be written as

$${}^{(1)}D'_2 = \frac{1}{\lambda'} [{}^{(2)}P'_2 (U'_c - U'_s)t + {}^{(3)}P'_2 U'_s t] + \epsilon'_{23} {}^{(1)}E'_3 \quad (2-26)$$

Comparing equations (2-6) and (2-26) we see that the two are similar except for the E'_3 term. The current in the external circuit can be written as

$$\begin{aligned} i &= A \frac{dD'_2}{dt} = \frac{A}{\lambda'} \{ {}^{(2)}P'_2 U'_c + [{}^{(3)}P'_2 - {}^{(2)}P'_2] U'_s + \lambda' \epsilon'_{23} \dot{E}'_3 \} \\ &= \frac{A}{\lambda'} [P'_{2c} U'_c + P'_{2s} U'_s] + i_E \end{aligned} \quad (2-27)$$

The values of i_E in equations (2-22) and (2-27) will be different because the polarization fields in the X'_3 -direction will be different in the two cases.

2.3 LINEAR COUPLED RESPONSE OF A ROTATED-CUT GAGE TO COMBINED COMPRESSION AND SHEAR LOADING

We now present the theoretical formalism for including electro-mechanical coupling in the gage output analysis. The theoretical developments for compression-only loading and without the complexity introduced by rotated cuts can be found in the paper by Chen et al.¹⁴ However, these authors include finite strain and more general external electrical circuit conditions in their work.

The experimental situation analyzed here is comparable to that shown in Figure 1. The approach to solving the coupled problem is similar to that for other wave propagation problems. The constitutive equation in combination with the governing equations yields a wave equation, which is then solved to provide the wave profiles at different positions in the sample. Except for a linear elastic solid, a numerical

method is needed to obtain the wave profiles. In the coupled problem, the constitutive equation has both mechanical and electrical terms. Hence, the external circuit conditions can influence the wave profiles. A comprehensive discussion of this topic is presented in an article by Thurston.²⁰

For the one-dimensional problem of interest, we can write the governing equations as²⁰

$$\left(\frac{\partial \sigma'_{2i}}{\partial X'_2}\right) = \rho_o \left(\frac{\partial u'_i}{\partial t}\right)_{X'} \quad (2-28)$$

$$\left(\frac{\partial \epsilon'_{22}}{\partial t}\right)_{X'} = \left(\frac{\partial u'_2}{\partial X'_2}\right)_t \quad (2-29)$$

$$\left(\frac{\partial \epsilon'_{2i}}{\partial t}\right)_{X'} = \frac{1}{2} \left(\frac{\partial u'_i}{\partial X'_2}\right)_t ; \quad i \neq 2 \quad (2-30)$$

$$\rho_o \left(\frac{\partial \underline{\epsilon}}{\partial t}\right)_{X'} = \sigma_{1i} \left(\frac{\partial u'_i}{\partial X'_2}\right) \quad (2-31)$$

Here ρ_o is the initial density, u'_i is the particle velocity in the X'_i -direction, and $\underline{\epsilon}$ is the specific internal energy. We are using the small strain approximation and considering stresses and strains to be positive in tension.

By choosing the strain (ϵ_{ij}) and the displacement field (D_m) as independent variables, we can write the constitutive equation for a linear piezoelectric solid in the matrix notation [see the matrix and tensor notation following equation (2-10)]^{*}

*The constitutive equations are in the X_i system unlike the governing equations (2-28) through (2-31).

$$\sigma_{\alpha} = C_{\alpha\lambda}^D \epsilon_{\lambda} - h_{m\alpha} D_m \quad (2-32)$$

$$E_i = -h_{i\alpha} \epsilon_{\alpha} + \beta_{ij}^{\epsilon} D_j \quad (2-33)$$

where

$$\beta_{ij}^{\epsilon} = \left(\frac{\partial E_i}{\partial D_j} \right)_{\epsilon}, \quad -h_{ikm} = \left(\frac{\partial \sigma_{km}}{\partial D_i} \right) \quad (2-34)$$

and C_{ij}^D are the elastic stiffness constants in a constant \vec{D} field. We assume isentropic deformation and recognize that the Maxwell relations can be written as

$$-\left(\frac{\partial \sigma_{ij}}{\partial E_m} \right) = \left(\frac{\partial D_m}{\partial \epsilon_{ij}} \right) \quad (2-35)$$

Further details about the constitutive equations can be found in Chapter 4 of Mason's book²¹ or Section 14 of Thurston's review article.²⁰ The constitutive equations clearly show the dependence of the elastic moduli and, hence, the wave velocities on the electrical variables. In Appendix B, the relation between C_{ij}^D and C_{ij}^E is derived.

In the absence of electromechanical coupling, equations (2-28) through (2-31) in conjunction with the constitutive equations can be solved for a particular initial condition using a generalized one-dimensional wave propagation program.²² Such calculations are described in Appendix B. For the electromechanical problem we need to specify the external electrical conditions. A simple resistive circuit is considered.

The current flowing in the external circuit is given by

$$i(t) = A \frac{dD_2'}{dt} \quad (2-36)$$

The voltage, across a resistor R , in the external circuit is

$$V(t) = AR\dot{D}_2 = - \int_0^{\ell'} E_2' dx_2' \quad (2-37^*)$$

For a rotated-cut crystal, we have

$$D_i' = P_i' + \epsilon_{ij}' E_j' \quad (2-38)$$

We can eliminate E_2' between equations (2-37) and (2-38) and write a differential equation for $D_2(t)$. We consider the specific situation of a rotated Y-cut LiNbO_3 crystal and use the permittivity tensor from equation (2-13). Combining equations (2-37) and (2-38), the voltage in the external circuit is

$$AR\dot{D}_2 = - \int_0^{\ell'} \frac{D_2' - P_2' - \epsilon_{23}' E_3'}{\epsilon_{22}'} dx_2' \quad (2-39)$$

Because of equation (2-12), D_2' is only a function of time. The tangential component of the \vec{E} field is continuous through the thickness of the disk. As before, we assume the permittivity to be unchanged by the small strain. Hence,

$$AR\dot{D}_2 = - \frac{(D_2' - \epsilon_{23}' E_3')\ell'}{\epsilon_{22}'} + \frac{1}{\epsilon_{22}'} \int_0^{\ell'} P_2' dx_2' \quad (2-40)$$

P_2' in the disk depends on all three strain components (ϵ_2' , ϵ_4' , and ϵ_6') as indicated in equation (2-23).

The general solution of the coupled problem is obtained by solving equations (2-28) through (2-30), (2-32), and (2-40) simultaneously. Lawrence and Davidson¹⁵ presented a numerical method for solving the coupled problem for the simpler uniaxial strain loading. This solution will be useful as a guide in developing the solution for the more complex situation considered here.

*The form of this equation is identical to Eq. (3.2) in the paper by Chen et al. in the limit of small strains.¹⁴ A similar equation was derived 20 years ago by Jones et al.⁹

In the short-circuit approximation ($R \approx 0$), we obtain the results derived in the last subsection.

$$D_2' = \frac{1}{\ell'} \int_0^{\ell'} P_2' dX_2' + \epsilon_{23}' E_3' \quad (2-41)$$

Although this expression is the same as that derived for the elastic-dielectric medium in the uncoupled approximation, the similarity is somewhat misleading because the values of the \vec{D} field at any instant determine the mechanical variables through equation (2-32). Hence, the electrical and mechanical variables need to be calculated simultaneously. Figure 4 in Reference 15 shows clearly the effect of electro-mechanical coupling on the current output from a Z-cut LiNbO₃ gage. The electrical field variations can produce stresses in regions where the mechanical wave has not reached. To include electromechanical coupling in the analysis of wave propagation (presented in Appendix B) in rotated-cut crystals is a time-consuming but straightforward procedure. However, before such a task is attempted, the importance of the two-dimensional electrical field effects indicated at the end of the last subsection needs to be determined.

The electromechanical coupling effects can be neglected in two situations: in the analysis of the initial current jump as discussed by Graham⁶ and in the open-circuit mode where no current is allowed to flow in the external circuit. This latter situation arises in the field usage of piezoelectric gages. In the open-circuit mode, $i = 0$ in equation (2-36). Hence, D_2' is independent of time.* Thus, the mechanical variables can be calculated in the usual manner by using C_{ij}^D as the elastic moduli. For the open-circuit case, the mechanical boundary conditions and their effects on the electrical fields may be important.

* Because of zero conductivity, D_2' is independent of X_2' .

2.4 IMPLICATIONS FOR EXPERIMENTS

It is desirable to find a gage whose output can be modeled using the idealized elastic dielectric analysis presented in Section 2.2. Such a gage would have to meet the following three requirements: (1) its electrical polarization must be due solely to the shear stress of interest (no cross-axis shear effect), (2) this polarization must be one-dimensional and along the gage thickness direction, and (3) the gage thickness direction must be a specific direction.

As indicated in our previous study,² none of the principal cuts in α -quartz or LiNbO_3 satisfy all of these requirements. Even when rotated-cuts are used* only the 163° Y-cut LiNbO_3 crystal approaches the desired requirements. As indicated earlier, the optimal orientation depends strongly on the values of the piezoelectric constants e_{ij} . Also, for the gage to be useful the crystal orientation has to be matched accurately to its optimal value. Practical usage always involves some error or variation. Hence, laboratory experiments are required to assess the gage response, to verify the theoretically predicted behavior, and to determine the tolerance limits for the gage response. Because the output of the rotated-cut crystals is not easily analyzed, the experiments are designed using the idealized analysis. Subsequently, the gage output is carefully analyzed to assess the deviation from the idealized behavior.

Although the current or short-circuit mode is more complex, it is ideally suited for laboratory calibration studies. The initial jump can be analyzed without the complexity of electromechanical coupling. The results can then be used in developing a gage package for field applications.

Our feasibility study indicated that the specific direction closest to the 163° Y-cut orientation was the 165.5° Y-cut orientation.² The

*The accepted nomenclature for piezoelectric crystals is presented in Reference 3.

closeness of these two orientations suggested that they both should be examined in the laboratory experiments. The one-dimensional compression and shear experiments we performed on gages with these orientations are described in the next section. These experiments allowed us to quantitatively measure the shear-to-compression sensitivity ratio (163° Y-cut orientation), check the piezoelectric constants by performing experiments along a specific direction (165.5° Y-cut orientation), and determine the effect of small deviations from a specific direction. In addition, detailed analysis of the gage response can be used to ascertain the need to model the more complex phenomena indicated in this section.

SECTION 3

EXPERIMENTAL METHOD AND RESULTS*

3.1 EXPERIMENTAL DESIGN AND METHOD

All the LiNbO_3 gages used in our work were fabricated by Specialty Engineering Associates according to our specification. The LiNbO_3 crystals were cut to the desired orientation to within $\pm 0.5^\circ$.[†] The gages were parallel to within $\pm 2.5 \mu\text{m}$ and were planar to within $\pm 1 \mu\text{m}$. These values are typical of piezoelectric gages used in shock wave experiments. The wraparound (or shorted gage) configuration²³ was used in all the experiments described here. A few experiments were performed with the shunted-gage configuration, but it was difficult to maintain a ground connection with the gage front surface. Because the shunted gage configuration is a superior configuration,²³ the possibility of using shunted gages in future experiments should be examined.

Guard rings, nominally 0.08 mm wide, were cut on the back side, and a 50- Ω resistor was connected across the inner electrode and the ground (or outer) electrode. The gages were enclosed in an aluminum housing with epoxy potting at the rear of the gage. The nominal values for gage diameter, gage thickness, and the inner electrode diameter were 26 mm, 5 mm, and 8 mm, respectively. The exact values for the different gages along with the experiment number are presented in Table 1. Some of the columns in Table 1 are explained in the following paragraphs.

*The work described in this section was performed in collaboration with W. J. Murri.

†The supplier indicated that the orientations were good to within $\pm 0.2^\circ$. We now believe that future work will require that the orientations be known with better accuracy.

Table 1. Details of LiNbO_3 gages.

Experiment No.	Gage Type	Z'-Axis Orientation ^a	Gage Diameter (mm)	Gage Thickness (mm)	Inner Electrode Diameter (mm)	Guard Ring Width (mm)	Gage Resistor (Ω)	Effective Resistance (Ω)	Thickness Area x Wave Vel. (s/m^2) ^c
1 (78-2-46)	163.0° Y-cut	0°	26.00	5.00	4.00	0.102	~50	~25	5.611×10^{-2}
2 (81-2-15)	163.0° Y-cut	0°	26.05	5.02	7.98	0.081	50.7	24.3	1.459×10^{-2}
	163.0° Y-cut	90°	26.05	5.02	7.99	0.080	53.0	26.8	1.456×10^{-2}
3 (81-2-22)	163.0° Y-cut	0°	26.05	5.02	7.98	0.079	50.7	26.1	1.459×10^{-2}
	165.5° Y-cut	0°	26.04	4.99	8.01	0.081	52.2	25.0	1.439×10^{-2}
4 (81-2-23)	163.0° Y-cut	0°	26.04	4.98	8.00	0.1	51.2	26.4	1.433×10^{-2}
	165.5° Y-cut	0°	26.04	4.99	8.01	0.09	50.4	26.0	1.436×10^{-2}
5 (81-2-24)	163.0° Y-cut	0°	26.05	5.02	7.99	0.081	49.90	26.05	1.455×10^{-2}
	163.0° Y-cut	90°	26.05	5.02	7.98	0.086	51.81	26.37	1.457×10^{-2}
6 (81-2-43)	165.5° Y-cut	0°	26.04	4.99	8.00	0.086	52.25	25.05	1.441×10^{-2}
	165.5° Y-cut	90°	26.04	4.99	7.99	0.093	52.4	25.9	1.442×10^{-2}
7 (84-542)	165.5° Y-cut	90°	26.04	4.99	7.99	0.09	52.6	26.25	1.443×10^{-2}
8 (84-543)	163.0° Y-cut	0°	26.04	4.98	8.00	0.094	53.76	26.16	1.435×10^{-2}
	163.0° Y-cut	90°	26.04	4.98	8.00	0.09	52.75	26.05	1.437×10^{-2}

^aThis column refers to the orientation of the Z'-axis on the gage housing in the impact experiment:

Z' = 0° indicates that the Z'-axis was along the vertical direction (direction of shear);

Z' = 90° indicates that the Z'-axis was along the horizontal direction (perpendicular to shear).

^bThis value takes into account the termination at the oscilloscope.

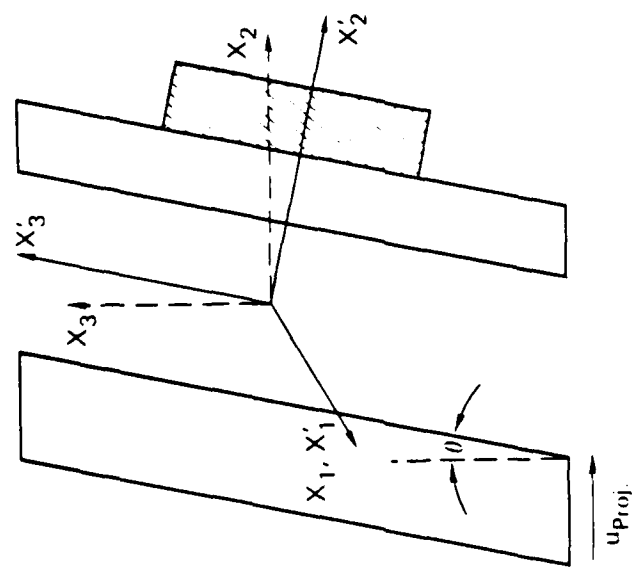
^cThis is (t/AU_c) defined in equation (2-8) of Section 2.

The back surface gage configuration shown in Figure 2 was used in all the experiments. A flyer plate inclined at an angle of $90^\circ - \theta$ to the direction of projectile motion impacts a parallel specimen plate backed by the LiNbO_3 gage. To distinguish from the laboratory coordinate system (X_1 -system), we define a X_1' -system with the X_2' -axis parallel to the gage thickness direction, and the X_1' -axis coincident with the X_1 -axis.

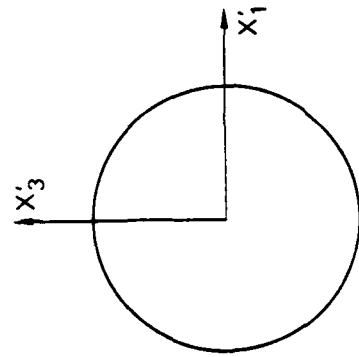
For a general impact ($\theta \neq 0^\circ$), two waves are propagated into the flyer plate and the sample plate: a compressive wave and a shear wave. The compressive wave, which travels at a faster velocity through the sample plate, impacts the specimen-gage interface, producing a transmitted wave in the LiNbO_3 and a reflected wave in the sample plate. The slower traveling shear wave in the sample plate interacts* with the reflected compressive wave before arriving at the specimen-gage interface.

The use of a back surface gage for determining gage calibrations is not an optimal arrangement because of the need for an accurate knowledge of the shear response of the specimen, the wave interactions in the specimen, and the shear strength of the specimen-gage interface. The advantage of using the specimen (or buffer) plate is that it provides a temporal separation between the compression and the shear wave. This separation permits an evaluation of the gage response to each wave and is useful in modeling the response of a rotated-cut crystal. If the intent is to measure the piezoelectric constants, then compression-only ($\theta = 0^\circ$) experiments with no buffer plates, such as those performed by Graham,⁶ are desirable. In our experiments, the flyer and specimen plates were made of PMMA (Rohm and Haas Type II UVA Plexiglass). This material has been studied both under compression²⁴ and shear loading.²⁵ The specimen plate thickness was typically 1 mm.

*In the present case, we assume linearity and ignore this interaction.



(a) The piezoelectric gage is bonded to the rear surface of the PMMA specimen. Note that X'_2 is normal to the gage and X'_3 is parallel to the shear direction; X_i define the laboratory coordinate system.



(b) The primed axes as viewed from the impact side. The X'_2 axis is into the plane of the paper.

Figure 2. Schematic view of the impact experiment.

For experiments where a shear wave was introduced in the sample plate ($\theta \neq 0^\circ$), the direction of the shear motion was always along the X_3' -axis. The two coordinate systems shown in Figure 2 are related to the crystal orientation in the following manner. The rotated Y-cut crystals involve rotations about the crystallographic X-axis. We denote a new set of axes relative to the disk of the cut crystal by X' , Y' , and Z' . The Y' -axis is normal to the crystal disk, and is related to the crystallographic Y-axis by a rotation of 163° or 165.5° about the crystallographic X-axis. As a result the X' -axis coincides with the crystallographic X-axis, with the Z' -axis normal to it in the plane of the disk. The supplier had marked both the X' - and Z' -axes on the sides of the crystals. As indicated earlier, the optimal gage is one that produces an electrical output only when sheared along the Z' -direction.

In Table 1, $Z' = 0^\circ$ means that the Z' -axis marked on the gage housing was oriented along the X_3' -axis; $Z' = 90^\circ$ indicates that it was aligned with the X_1' - and X_1 -axes. The purpose of the $Z' = 90^\circ$ alignment in combined compression and shear experiments was to check the cross-axis shear effects. For this alignment, the X' - (or X -) axis is along the X_3' -axis, which is the direction of shear. A signal for this alignment would imply a cross-axis shear effect. Most of our experiments were compression-only ($\theta = 0^\circ$) experiments. Aligning the Z' -axis along either the X_3' - or X_1' -axis, was advantageous because it permitted us to evaluate the effect of impact tilt, as discussed later.

The impact experiments were performed using the SRI gas-gun facility for studying large-amplitude one-dimensional compression and shear wave propagation in solids.²⁶ Details of the gun barrel, target holder, and related instrumentation for measuring particle velocities, projectile velocities, and impact misalignment are presented in Reference 26.

The target assembly for the impact experiments was constructed by bonding the LiNbO_3 gage to a PMMA specimen plate that was typically 5 mm thick. Epon 815 epoxy resin and hardner were used for bonding, and the epoxy layer was made very thin (less than 1-2 μm). The PMMA specimen-

gage assembly was potted in aluminum target ring as shown in Figure 3. The front face of the target assembly was machined and ground to achieve a 1 mm thickness for the PMMA plate. The completed projectile and target assembly shown in Figure 3 are for a single-gage, compression-only experiment.

The U-shaped vapor-deposited gage on the PMMA surface is used to measure the particle velocity at the impact surface. For compression-only experiments, this measurement is not necessary because the particle velocity is one-half the projectile velocity. However, in combined compression and shear experiments, this measurement is essential for determining the shear particle velocity at the impact face. The three sets of vapor-deposited tilt pins, at 120° intervals, are used to measure the impact misalignment. The fourth set of metallic leads are 0.001-inch-thick copper foils used to trigger the electronics. The long outrigger on the projectile is necessary for the particle velocity measurements, as indicated in Reference 26. The target assembly for the combined compression and shear experiments reported here is identical to that for the compression-only experiments. The projectile assembly is also similar except that the flyer plate is mounted by cutting the outrigger at an angle. All components are precisely aligned using the three holes in the target ring, shown in Figure 3.

When we first began these experiments, we measured the tilt only to ensure that the impact misalignment was small. However, we later found that the tilt measurements were of particular importance because an accurate quantitative analysis of the data needs to incorporate the effects of tilt, as described in Section 4.3. We recommend that in future experiments the impact misalignment be measured with an even higher degree of accuracy.

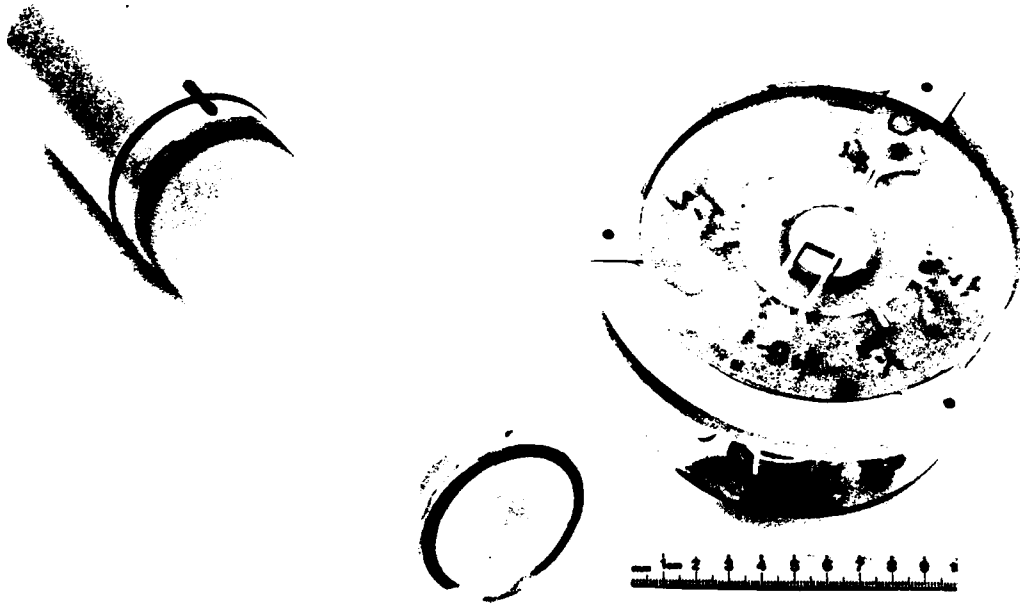


Figure 3. The projectile and target assembly used in the impact experiments. (The vapor-deposited metallic coating on the projectile shorts the vapor-deposited tilt pins on the target to provide a measurement of the impact alignment.)

3.2 EXPERIMENTAL RESULTS

Table 2 summarizes the eight experiments performed, which involved 14 gages.* Of these experiments, only Experiment 1 is taken from our feasibility study reported earlier.² The voltage-time profiles from all eight experiments are shown in Figures 4 and 5 and are discussed individually in this subsection. Appendix F shows more detailed current- or voltage-time plots prepared after digitizing the data.

In Table 2 the impact angle refers to the value of θ as defined in Figure 2(a). Impact tilt is based on the closure time across the three sets of pins shown in Figure 3. Although the absolute values of the tilt measurements are probably accurate to within only 10 to 15 percent, the values cited in Table 2 are good representations of the relative differences between the shots. The fifth column of Table 2 lists the orientation of the normal to the line of contact during closure relative to the X_1' -axis as defined in Figure 6. For example, a nonzero value of the tilt in Experiment 3 implies that the impact was not simultaneous over the entire face of the specimen plate; the 90° value in the fifth column indicates that the closure between the flyer and sample plate proceeded along the X_3' -axis. Effectively, this results in a shear deformation along the X_3' -direction even for a compression-only ($\theta = 0^\circ$) experiment. As discussed later, this effect is significant and needs to be accounted for in the data analysis.

The next three columns of Table 2 are defined as in Table 1. The measured current, in column nine, is calculated using the voltage value at the first jump and the effective resistance values cited in Table 1. In using piezoelectric gages, it is generally preferable to use current calibration steps rather than voltage calibration steps; this procedure

*Several other experiments were performed, but they did not yield meaningful data, and the results are not listed here. In these experiments either the gage broke or foam impactors were used. The intent of using the foam impactor was to obtain low stresses without lowering the impact velocity.

Table 2. Summary of impact experiments.

Experiment No.	Impact Velocity (mm/ μ s)	Impact Angle	Impact Tilt	Impact Closure Direction ϕ	Gage Type	2'-Axis Orientation ^a	PMMA Buffer Thickness (mm)	Measured Current ^b (mA)	Shock Velocity (mm/ μ s)	Polarization ^c (mC/m ²)
1 (78-2-46)	0.2	20°	0.105°	150°	163.0° Y-cut	0°	1.41	5.6 (37.8)	-	0.31 (2.66)
2 (81-2-15)	0.154	15°	0.087°	140°	163.0° Y-cut 163.0° Y-cut	0° 90°	0.838 0.838	38.1 (152) 80.6	6.75 6.72	0.56 (2.45) 1.17
3 (81-2-22)	0.213	0°	0.016°	90°	163.0° Y-cut 165.5° Y-cut	0° 0°	0.953 1.029	27.1 115	6.72 6.79	0.395 1.65
4 (81-2-23)	0.152	0°	0.04°	90°	163.0° Y-cut 165.5° Y-cut	0° 0°	0.927 0.902	29 85.1	6.76 6.7	0.415 1.22
5 (81-2-24)	0.217	15°	0.122°	129°	163.0° Y-cut 163.0° Y-cut	0° 90°	0.991 1.029	80 (241) -	6.72 -	1.16 (3.45) -
6 (81-2-43)	0.206	0°	0.1°	109°	165.5° Y-cut 165.5° Y-cut	0° 90°	0.94 0.94	134 173	6.6 -	1.93 2.49
7 (84-542)	0.2	0°	.0395°	246°	165.5° Y-cut	90°	0.98	92.5	-	1.33
8 (84-543)	0.203	0°	.055°	300°	163.0° Y-cut 163.0° Y-cut	0° 90°	1 1	15.5 22.8	- -	0.22 0.33

^aSee Table 1, footnote a, for explanation of 2' values.

^bThe values in parentheses correspond to the values after the shear wave arrival at

the specimen-gage interface and include both compression and shear wave contributions.

^cThe values in parentheses are due solely to the shear wave.

avoids measuring the effective resistance separately. We believe our calibration procedure is reasonable (within 1-2 percent) because the effective resistance was carefully measured. In fact, the largest error occurs in reading the voltage jump. Because of the significant current ramping following the initial jump and because of the rounding, seen in most of the records, it is difficult to identify the first jump. This error is significant for Experiment 6 as seen in Figure 5(f). The three current values shown in parenthesis in the current column correspond to the jump following the shear signal and include the contributions from both the compression and shear waves.

The duration of the signal, shown in Figures 4 and 5, permits a measurement of the quasi-longitudinal wave (shock) velocity in the LiNbO_3 crystals, which is indicated in the second-to-last column. Averaging the five 163° Y-cut values and the three 165.5° Y-cut values, we obtain the following wave velocities:

163° Y-cut:	6.73 mm/ μ s
165.5° Y-cut:	6.72 mm/ μ s

Using the C_{ij}^D values derived from Smith and Welsh's paper,⁵ we calculated the quasi-longitudinal wave velocity, as outlined in Appendix B. The calculated wave velocities for these two orientations are within 0.1 percent of each other, and we cite an average calculated value of 6.743 mm/ μ s for both orientations. Given an experimental scatter of ± 1 percent in the data, the measured wave velocities agree with the calculated wave velocities. To be consistent with our numerical calculations, we used the 6.743 mm/ μ s value in analyzing the current data.

In Section 2.1, the current output for the idealized situation was derived as

$$i = \frac{A}{l} [P_c U_c + P_s U_s] \quad (2-8)$$

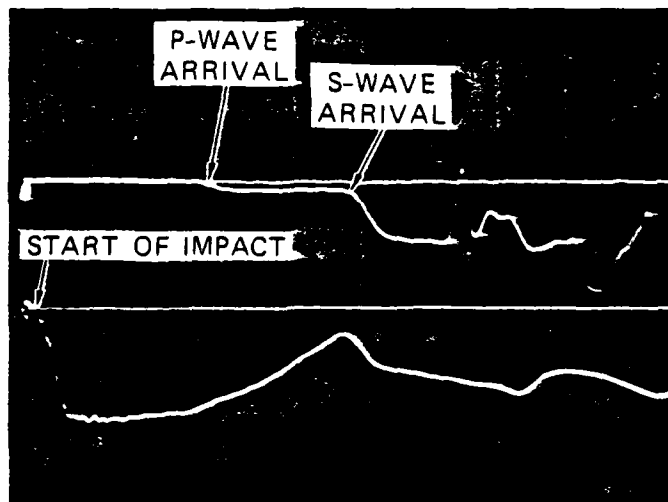
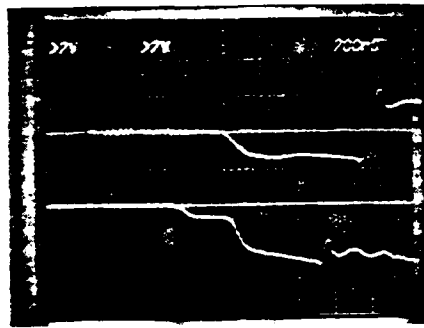
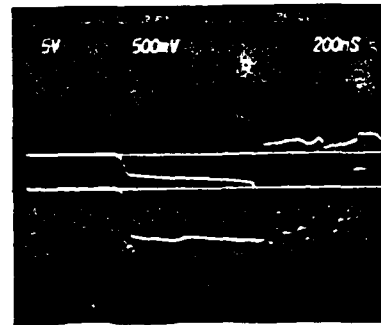


Figure 4. Voltage-time profiles from experiment 1 (78-2-46) with 163° Y-cut ($Z' = 0^\circ$) LiNbO_3 gage. [The top trace represents output from the LiNbO_3 gage (1 V/div). The bottom trace represents transverse particle velocity imparted to the PMMA (0.05 V/div). Time scale is common to both traces (0.2 $\mu\text{s}/\text{div}$)].



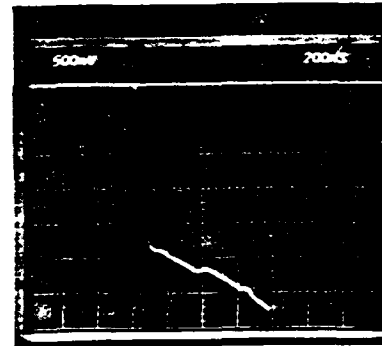
(a) 2 (81-2-15)
 Upper Trace: 163° ($Z' = 90^\circ$)
 Lower Trace: 163° ($Z' = 0^\circ$)



(b) 3 (81-2-22)
 Upper Trace: 165.5° ($Z' = 0^\circ$)
 Lower Trace: 163° ($Z' = 0^\circ$)

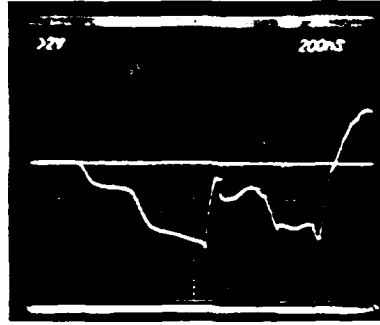


(c) 4 (81-2-23)
 163° ($Z' = 0^\circ$)

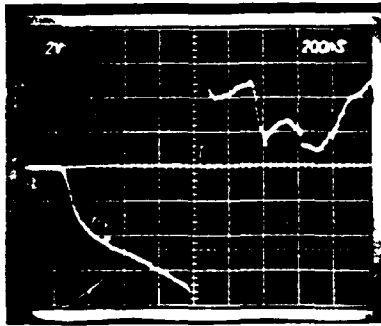


(d) 4 (81-2-23)
 165.5° ($Z' = 0^\circ$)

Figure 5. Voltage-time profiles from experiments 2 through 8 with rotated Y-cut LiNbO_3 gages. [The voltage and time scale per division are shown in the photographs. The voltage scale in (a) was 3 V/div.]



(e) 5 (81-2-24)
163° ($Z' = 0^\circ$)

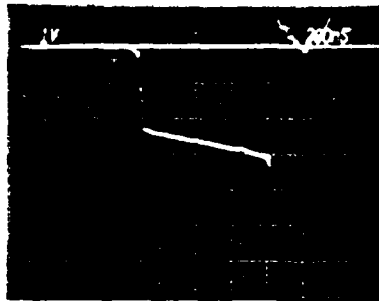


(f) 6 (81-2-43)
165.5° ($Z' = 0^\circ$)

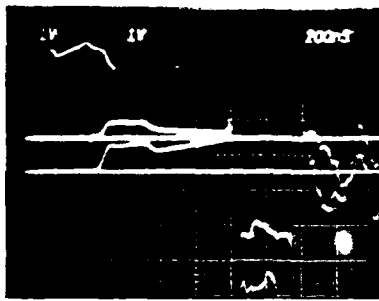


(g) 6 (81-2-43)
165.5° ($Z' = 90^\circ$)

Figure 5. Voltage-time profiles from experiments 2 through 8 with rotated Y-cut LiNbO_3 gages. [The voltage and time scale per division are shown in the photographs. The voltage scale in (e) was 3 V/div. The voltage and time setting in (f) and (g) are alike.] (Continued).



(h) 7 (84-542)
 165.5° ($Z' = 90^\circ$)



(i) 8 (84-543)
 Upper Trace: 163° ($Z' = 0^\circ$)
 Lower Trace: 163° ($Z' = 90^\circ$)

Figure 5. Voltage-time profiles from experiments 2 through 8 with rotated Y-cut LiNbO_3 gages. (The voltage and time scale per division are shown in the photographs.) (Concluded).

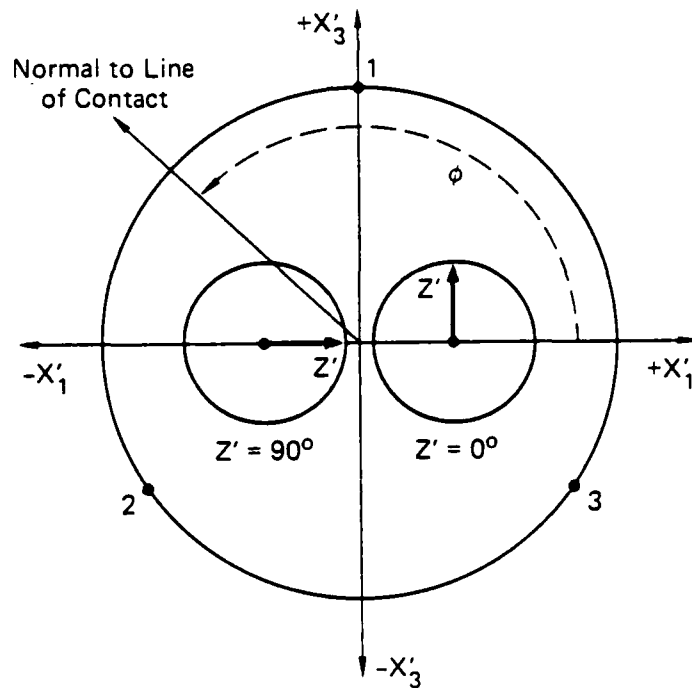


Figure 6. Impact closure as seen from the projectile side. [The X'_i axes are the same as shown in Figure 2(b). The points 1, 2, and 3 refer to the tilt pins. The two axes labeled Z' represent the orientations of the projection of the Z' -axis onto the plane of the crystal disk in the two gage orientations typically used in our experiments. For a nonsimultaneous closure, the line of contact is defined by the angle ϕ .]

where l is the gage thickness, A is the effective electrode area, U_c is the longitudinal wave velocity, and U_s is the shear wave velocity. Using the data given in Table 1 and the value of U_c cited above, we calculated the compressive polarization (P_c), listed in the last column of Table 2. The polarization due to shear (P_s) is shown in parenthesis for the three compression-and-shear experiments along the 163° Y-cut orientation. A calculated U_s value of $4.58 \text{ mm}/\mu\text{s}$ was used in determining the P_s value. Note that, unlike the current values in parenthesis, the shear polarization values are due only to the shear deformation.[†] That is, the shear polarization values were calculated from the difference in the current values.

The method used to analyze the current data at the initial jump in our experiments is similar to that used by Graham for his LiNbO_3 data.⁶ The one minor difference is that Graham incorporates finite strain correction in his results. In our experiments, the strain values are less than 0.2 percent, and this correction is ignored in calculating the polarization.

As mentioned earlier, the effect of tilt is an important factor. As shown in Figure 6, not only is the tilt angle (column 4 in Table 2) important, but the orientation of the line of closure with respect to the X_1' -axis (column 5 in Table 2) also influences the result in two ways. First, the angle ϕ determines the relative magnitude of the shear strains ϵ'_{23} ($= \epsilon'_{32}$) and ϵ'_{31} ($= \epsilon'_{13}$); second, for two-gage experiments, the time correlation between the two sets of signals depends on the angle ϕ . A general theoretical analysis for quantitatively incorporating the effects of impact tilt by assuming the LiNbO_3 as an isotropic, elastic plate is presented in Appendix E. Further discussion of tilt effects using this analysis is presented in Section 4.

* A is computed using a diameter that extends to the center of the insulating gap in conformity with Graham's method.⁶

[†] This is only approximately true because we have not subtracted the small ramping contribution of the compression wave.

Results from the individual experiments (Figures 4 and 5) are discussed qualitatively below. These data are analyzed and the piezoelectric constants are calculated in Section 4.

Experiment 1 (78-2-46): Figure 4, taken from our earlier work,² shows the shear particle velocity at the impact surface along with the LiNbO_3 output on a common time scale. The measured shear particle velocity was approximately 90 percent of the value expected from the "no slip" condition. The LiNbO_3 signal shows a small signal from the compression wave and a larger signal for the shear wave. We did not have the precise resistance values and hence the current values cited in Table 2 are good to only 4 or 5 percent. However, the ratio of the compression signal to shear signal does not depend on the resistance and should be fairly accurate. On the basis of the tilt angle and the ϕ value in Table 2, we expect some shear contribution even for the compression wave.

Experiment 2 (81-2-15): This experiment was designed to address an important objective of this study: the effect of cross-axis shear. The two gages were oriented with their Z' -axis parallel ($Z' = 0^\circ$) and perpendicular ($Z' = 90^\circ$) to the X_3' -axis. In Figure 5(a), a clear two-step signal, similar to that in Figure 4, is seen for the $Z' = 0^\circ$ gage; the $Z' = 90^\circ$ gage does not show a two-step signal. This result confirms the theoretical predictions that the shear gage should display no cross-axis effect. Because of the direction of the impact closure line ($\phi = 140^\circ$), the $Z' = 0^\circ$ gage signal began earlier, as expected. There are two features of this experiment that we believe are caused by the impact tilt: the difference in the compression signal between the $Z' = 90^\circ$ and the $Z' = 0^\circ$ gage (see Table 2), and the small decrease in the $Z' = 90^\circ$ signal at the time of the shear wave arrival at the specimen-gage interface. We address these issues in the next section.

Experiment 3 (81-2-22): This experiment was designed to compare the output of 163° and 165.5° Y-cut crystals in a compression-only experiment. Such an experiment is also useful in checking the piezoelectric constants because the 165.5° Y-cut is a specific direction

on the basis of the literature C_{ij}^D values. Fortunately, this experiment also had the lowest tilt and ϕ was 90° . Thus, the gages were subjected to identical loading. In Figure 5(b), the initial current output of the 165.5° Y-cut gage is higher than that of the 163° Y-cut gage (also see Figure F.3). As expected for $\phi = 90^\circ$, both gage signals begin at nearly the same time. The 165.5° Y-cut gage signal actually begins earlier even though it had a thicker specimen plate. This suggests that the correlation with our tilt measurements is reasonably good but not exact. For an exact correlation, the centers of the two gages should be emplaced completely symmetric to the tilt pins.

The signals drop at a time that corresponds to the arrival of a shear wave at the specimen-gage interface. Because of the higher voltage sensitivity for the 163° Y-cut gage, this drop is more discernible in the record. Because no shear deformation was introduced into the specimen, the small shear wave generated due to tilt (see Appendix E) may be the cause of this drop in the signal. An estimate of this drop is made in the next section. (This is the same as the tilt correction).

Experiment 4 (81-2-23): This experiment was performed to confirm the findings of Experiment 3 and provide data at a different compressive level for calculating the piezoelectric constants. Unfortunately, the impact tilt was nearly 2.5 times the tilt in Experiment 3 although ϕ was 90° . Because ϕ was 90° , we expected the two gage signals to begin simultaneously. The signal of the 163° Y-cut gage is observed to start slightly early, confirming our remarks earlier concerning the limited accuracy of our tilt measurements. The overall features of the gage records are similar to those shown in Figure 5(b) for Experiment 3. The drop in the signal, discussed above, occurs in both gage records. Linearly scaling the results of Experiment 3, we expected a current jump of 82 mA for the 165.5° Y-cut gage. Instead, the observed jump was 85 mA. The current jump for the 163° Y-cut gage was 5 to 7 percent higher than the jump in Experiment 3 although linear scaling suggests a decrease of 30 percent. Again, the influence of tilt is at least a

qualitative explanation for this because it would have a larger relative effect for the 163° Y-cut orientation. However, without a quantitative analysis this is only conjecture.

Experiment 5 (81-2-24): This experiment was designed to provide data similar to that from Experiment 2 but at a higher stress. Unfortunately, the tilt was 40% higher than in Experiment 2, and the $Z' = 90^\circ$ gage did not produce any meaningful data. The $Z' = 0^\circ$ gage again shows the characteristic two-step signal expected for combined compression and shear loading. The shear polarization value, P_s , scales very well between this experiment and Experiment 2. This value, measured as the difference between the two current steps, is largely unaffected by tilt. The current jump due to compression for this experiment is larger than expected from linear scaling with Experiment 2. However, the tilt value in Experiment 5 was higher than that in Experiment 2 (the ϕ value was comparable) and this can influence the results.

Experiment 6 (81-2-43): This experiment was designed to examine the differences in the effect of tilt, if any, in a compression-only experiment. Both gages had the 165.5° Y-cut orientation. One was aligned with $Z' = 0^\circ$ and the other with $Z' = 90^\circ$. As seen in Figures 5(f) and 5(g), the two voltage-time profiles are quite different. We have spent considerable time in trying to understand this result but have had little success. The marked roundedness of the initial jump in both records adds uncertainty to a comparison of their magnitudes, and the profiles beyond the first jump are markedly different. One is forced to conclude that tilt and variations in gages must be the cause because there is no other way to distinguish between these gages in a compression-only experiment. The impact tilt and the ϕ value in Table 2 suggest that the shear generated by the tilt will increase the polarization for the $Z' = 0^\circ$ gage. The $Z' = 0^\circ$ gage profile from this experiment is comparable to the 165.5° Y-cut ($Z' = 0^\circ$) gage profile from Experiment 3, shown in Figure 5(b). The higher initial jump in Experiment 6 compared with the initial jump in Experiment 3 also

suggests tilt effects. It is the $Z' = 90^\circ$ gage profile in this experiment that remains a mystery.

Experiment 7 (84-542)*: This experiment was performed to reproduce and, we hoped, provide understanding of the response observed for the 165.5° ($Z' = 90^\circ$) gage in Experiment 6. The measured voltage-profile shown in Figure 5(h) is considerably different from the profile in Figure 5(g). Because the tilt for this experiment was small, the rise time in Figure 5(h) is smaller than Experiment 6. The tilt result from this experiment is comparable to Experiment 3 and the overall profiles in Figure 5(d) and Figure 5(g) are similar. The measured current jump of 92.5 mA is markedly different from the values in Experiment 6 but is closer to the current values in Experiments 3 and 4. Before drawing any final conclusions, the tilt analysis needs to be incorporated. On the basis of this experiment, and the similarity with Experiments 3 and 4, we conclude that the results from the 165.5° ($Z' = 90^\circ$) gage in Experiment 6 are anomalous. The cause of the anomaly is presently unknown.

Experiment 8 (84-543)*: Because the results from Experiment 6 were not useful, we performed a compression-only experiment with $Z' = 0^\circ$ and $Z' = 90^\circ$ gages to examine the effects of tilt. In the absence of tilt these gages should provide identical response. The only gages that were available to us from the original batch were 163° Y-cut crystals. The measured voltage profiles are shown in Figure 5(i). As indicated in Table 2, the current and polarization at the first jump are 50 percent different. This difference can be due to two factors: tilt effects or variations in gage orientations. These data are analyzed in the next section and compared with theoretical predictions incorporating tilt effects to determine the cause of the observed difference.

*Experiments 7 and 8 were performed at the Shock Dynamics Laboratory of Washington State University. The assistance of Pete Majewski and Martin Williams is gratefully acknowledged.

The experimental results from all the experiments are summarized as follows:

- (1) The 163° Y-cut LiNbO_3 crystals show considerably larger sensitivity to shear loading than to compressive loading.
- (2) The 163° Y-cut LiNbO_3 does not appear to be sensitive to cross-axis shear.
- (3) There is considerable experimental evidence to suggest that, because of the large shear sensitivity of these gages, we need to account for tilt effects in data analysis. Not only is the magnitude of the tilt angle important, but the relative orientation of the impact closure line can also make a difference.
- (4) The response of the crystal in the Y-cut 165.5° orientation to compression loading is considerably higher than the response of the crystal in the 163° Y-cut orientation.
- (5) The results of Experiment 6, in which two 165.5° Y-cut gages ($Z' = 0^\circ$ and $Z' = 90^\circ$) were subjected to compression-only loading, are not currently understood. Based on the results of Experiment 7, the $Z' = 90^\circ$ result in Experiment 6 is believed to be anomalous.
- (6) The large current rise beyond the initial jump suggests the importance of modeling electromechanical coupling at late times.
- (7) Some of the experimental results do not scale with projectile velocity, suggesting effects of tilt or variability of the orientation of the crystals. The latter effect would be particularly important for the 163° orientation.
- (8) The wave velocity measurements, inferred from the duration of the signal, show a ± 1 percent scatter. Within this scatter, these values match the calculations.

SECTION 4
ANALYSIS AND DISCUSSION

This section compares the experimental results with the theoretical predictions using the uncoupled elastic-dielectric model outlined in Sections 2.1 and 2.2. We believe that the uncoupled approximation is appropriate for analyzing the initial jump in our experiments. Potential causes for discrepancy between the theory and experiment are examined. Tilt effects, using the theoretical developments presented in Appendix E, are estimated. The overall findings are discussed at the end of the section.

4.1 NUMERICAL SIMULATION OF THE EXPERIMENTS (MECHANICAL VARIABLES)

One-dimensional wave propagation code calculations were performed using the subroutine ANELAS described in Appendix B for computing the stress in anisotropic LiNbO_3 crystals. The pertinent mechanical variables in the LiNbO_3 for each of our experiments are listed in Table 3. The LiNbO_3 elastic constants, C_{ij}^D , used in these calculations are from the work of Smith and Welsh.^{5*} The PMMA was modeled as a nonlinear elastic material using the following material properties:

$$\begin{aligned} \text{Initial density:} & \quad \rho_0 = 1.185 \text{ g/cm}^3 \\ \text{Pressure-volume relation:} & \quad P \text{ (kbar)} = 62 \mu + 295 \mu^2 + 134 \mu^3 \\ & \quad \text{where } \mu = \frac{\rho}{\rho_0} - 1 \\ \text{Shear modulus:} & \quad G \text{ (kbar)} = 22.5 + P \end{aligned} \tag{4-1}$$

*These authors report only C_{ij}^E constants in their paper. These constants were converted to C_{ij}^D using the procedure indicated in Appendix B.

Table 3. Numerical simulation of LiNbO₃ experiments using C¹_{ij} from reference 5.

Experiment No.	Impact Velocity (mm/μs)	Gage Type ^a	LiNbO ₃ Strains			LiNbO ₃ Stresses (kbar)			LiNbO ₃ Particle Velocities (mm/μs)		
			ε ₂	ε ₄	ε ₆	σ ₂	σ ₄	σ ₆	u ₂	u ₃	u _i
Compression-Only Experiments											
3	0.213	163.0° Y-cut	-3.41 x 10 ⁻³	-5.45 x 10 ⁻⁵	0	-7.19	5.32 x 10 ⁻³	0	2.295 x 10 ⁻²	2.85 x 10 ⁻⁴	0
(81-2-22)	0.213	165.5° Y-cut	-3.41 x 10 ⁻³	4.2 x 10 ⁻⁷	0	-7.19	-4.08 x 10 ⁻⁵	0	2.296 x 10 ⁻²	-2.21 x 10 ⁻⁶	0
4	0.152	163.0° Y-cut	-2.35 x 10 ⁻³	-3.76 x 10 ⁻⁵	0	-4.95	3.54 x 10 ⁻³	0	1.58 x 10 ⁻²	1.97 x 10 ⁻⁴	0
(81-2-23)	0.152	165.5° Y-cut	-2.35 x 10 ⁻³	2.9 x 10 ⁻⁷	0	-4.95	-2.72 x 10 ⁻⁵	0	1.583 x 10 ⁻²	-1.53 x 10 ⁻⁶	0
6 ^b	0.206	165.5° Y-cut									
(81-2-43)											
7 ^b	0.2	165.5° Y-cut									
(84-542)											
8 ^b	0.203	163.0° Y-cut									
(84-543)											
Combined Compression and Shear Experiments ^c											
1	0.2	163.0° Y-cut	-2.97 x 10 ⁻³	-4.76 x 10 ⁻⁵	0	-6.26	4.38 x 10 ⁻³	0	1.998 x 10 ⁻²	2.47 x 10 ⁻⁴	0
(78-2-46)	(20°) ^d		-2.98 x 10 ⁻³	-6.26 x 10 ⁻⁴	0	-6.26	-1.12	0	2.002 x 10 ⁻²	5.54 x 10 ⁻³	0
2	0.154	163.0° Y-cut	-2.3 x 10 ⁻³	-3.7 x 10 ⁻⁵	0	-4.85	3.32 x 10 ⁻³	0	1.548 x 10 ⁻²	1.9 x 10 ⁻⁴	0
(81-2-15)	(15°) ^d		-2.31 x 10 ⁻³	-3.68 x 10 ⁻⁴	0	-4.85	-0.64	0	1.55 x 10 ⁻²	3.22 x 10 ⁻³	0
5	0.217	163.0° Y-cut	-3.34 x 10 ⁻³	-5.37 x 10 ⁻⁵	0	-7.06	5 x 10 ⁻³	0	2.25 x 10 ⁻²	2.78 x 10 ⁻⁴	0
(81-2-24)	(15°) ^d		-3.36 x 10 ⁻³	-5.33 x 10 ⁻⁴	0	-7.06	-0.93	0	2.26 x 10 ⁻²	4.67 x 10 ⁻³	0

^aAll gages listed here are oriented with Z' = 0°. See Table 1, footnote a.

^bThe results for these experiments can be scaled from the results for Experiment 3 (81-2-22).

^cThe two sets of results for the compression and shear experiments are explained in the text.

^dThe figures in parentheses refer to angle defined in Figure 2.

For compressive stresses below 7.6 kbar, the results of this model are in good agreement with the PMMA data of Barker and Hollenbach,²⁴ and Gupta.²⁵ In all the numerical simulations the PMMA buffer plate was modeled as 1 mm thick, which is slightly different from the actual thicknesses listed in Table 2. Because of the elastic nature of the calculation, this difference does not affect the wave amplitudes. Comparison with arrival times will require appropriate scaling. The results shown in Table 3 are based on zero tilt, that is, perfect alignment at impact. Hence tilt effects need to be separately accounted for.

For compression-only experiments in Table 3 there is only a single wave in the PMMA buffer plate. The stresses and strains are listed in the matrix notation. The results scale approximately with the projectile velocity; the scaling is not exact because of the nonlinear response of the PMMA. For the 165.5° Y-cut orientation, the LiNbO₃ strain response is nearly uniaxial. For the 163° Y-cut orientation, the shear strain, although small, can have significant contributions to the polarization, as discussed later. Because of the closeness of impact velocities, the results for Experiments 6 through 8 can be scaled from the results for Experiment 3.

The calculated results for the combined compression and shear experiments in Table 3 were results using a no-slip condition at both the impact and the PMMA/LiNbO₃ interface. The two sets of values for each experiment result from the two waves generated in the PMMA buffer plate. The first entry for each experiment represents the LiNbO₃ state after the compression wave arrival at the PMMA/LiNbO₃ interface; the second entry represents the final state after the arrival of the shear wave at the gage interface.

The shear strain ϵ'_6 and the corresponding stress and particle velocity are zero in Table 3. This result differs slightly from the numerical results presented in Table C-2 of Appendix C for Y-cut and 36°-rotated Y-cut crystals. The cause for this slight difference is the use of an X-cut quartz crystal as impactor in contrast to the use of PMMA as an impactor.

Table 4. Numerical simulation of LiNbO₃ experiments using C_{ij}^D from reference 4.

Experiment No.	Impact Velocity (mm/μs)	Gage Type ^a	LiNbO ₃ Strains			LiNbO ₃ Stresses (kbar)			LiNbO ₃ Particle Velocities (mm/μs)		
			ε ₂ ⁱ	ε ₄ ⁱ	ε ₆ ⁱ	σ ₂ ⁱ	σ ₄ ⁱ	σ ₆ ⁱ	u ₂ ⁱ	u ₃ ⁱ	u ₁ ⁱ
3 (81-2-22)	0.213	163.0° Y-cut	-3.41 x 10 ⁻³	-4.44 x 10 ⁻⁵	0	-7.2	4.34 x 10 ⁻³	0	2.298 x 10 ⁻²	2.32 x 10 ⁻⁴	0
	0.213	165.5° Y-cut	-3.41 x 10 ⁻³	1.13 x 10 ⁻⁶	0	-7.2	-1.1 x 10 ⁻⁴	0	2.3 x 10 ⁻²	-5.94 x 10 ⁻⁶	0
4 (81-2-23)	0.152	163.0° Y-cut	-2.35 x 10 ⁻³	-3.06 x 10 ⁻⁵	0	-4.96	2.89 x 10 ⁻³	0	1.58 x 10 ⁻²	1.61 x 10 ⁻⁴	0
	0.152	165.5° Y-cut	-2.35 x 10 ⁻³	7.82 x 10 ⁻⁷	0	-4.97	-7.39 x 10 ⁻⁴	0	1.59 x 10 ⁻²	-4.13 x 10 ⁻⁶	0

^aAll gages listed are oriented with z' = 0°. See Table 1, footnote a.

In Appendix B, we present the C_{ij}^D values from the work of Smith and Welsh⁵ and Warner et al.⁴ Except for the value of C_{12}^D the values for the other constants are quite close. To determine the effects of scatter in the C_{ij}^D values on our results, we performed a series of calculations for compression-only experiments using the C_{ij}^D values of Warner et al.⁴ The results are presented in Table 4. Comparing Tables 3 and 4 shows that the values of the compressive variables are almost identical. However, the values of the shear variables are different, and the larger relative differences observed for the 165.5° Y-cut orientation indicate that the two sets of constants give rise to somewhat different specific directions. However, both sets of constants show that the strain response along the 165.5° Y-cut is very nearly uniaxial. The ϵ_4' differences for 163° Y-cut orientation are not negligible and provide a measure of one source of scatter in comparing polarization values between theory and experiment. This is discussed in subsection 4.3.

4.2 ANALYSIS OF THE POLARIZATION MEASUREMENTS

The polarization along the gage thickness for a rotated Y-cut crystal can be written in the matrix notation as

$$P_2' = e_{22}' \epsilon_2' + e_{24}' \epsilon_4' \quad (2-23)$$

There is no contribution from the $e_{26}' \epsilon_6'$ term even when ϵ_6' is nonzero because for a Y-cut or a rotated Y-cut LiNbO_3 crystal e_{26}' is zero. Expressions for e_{22}' and e_{24}' are presented in Appendix D; the general expression for P_2' in terms of e_{ij}' is shown in equation (C.1).

Using the strain values cited in Table 3, the piezoelectric constants e_{ij}' , and equation (2-23), we can compare the calculated and measured polarization values, as shown in Table 5. In comparing these values, the following stipulations are important:

- (1) The measured current was converted to polarization using the uncoupled elastic-dielectric analysis of Section 2.2 because

Table 5. Comparison of polarization values (10^{-3} C/m^2).

Experiment No.	Gage Type	Z'-Axis Orientation ^a	Polarization Inferred From Measured Current Jumps ^b	Polarization Calculated From New e_{ij} Values ^c	Polarization Calculated From Old e_{ij} Values ^c
Compression-Only Experiments					
3	163.0° Y-cut	0°	0.4	1.6	0.44
(81-2-22)	165.5° Y-cut	0°	1.65	2.42	1.22
4	163.0° Y-cut	0°	0.42	1.1	0.3
(81-2-23)	165.5° Y-cut	0°	1.22	1.67	0.84
6	165.5° Y-cut	0°	1.93	2.35	1.18
(81-2-43)	165.5° Y-cut	90°	2.49	2.35	1.18
7	165.5° Y-cut	90°	1.33	2.275	1.14
(84-542)					
8	163.0° Y-cut	0°	0.22	1.535	0.416
(84-543)	163.0° Y-cut	90°	0.33	1.535	0.416
Combined Compression and Shear Experiments^d					
1	163.0° Y-cut	0°	0.31 (2.66)	1.40 (4.47)	0.38 (4.35)
(78-2-46)					
2	163.0° Y-cut	0°	0.56 (2.45)	1.09 (2.56)	0.3 (2.49)
(81-2-15)	163.0° Y-cut ^e	90°	1.17	1.09	0.3
5	163.0° Y-cut	0°	1.16 (3.45)	1.58 (3.71)	0.43 (3.6)
(81-2-24)					

^aSee Table 1, footnote a, for explanation of Z' values.
^bcf Table 2.

^cSee text for explanation.

^dFor the combined compression and shear experiments, the polarization values in parentheses are due solely to the shear wave.

^eFor this gage, the shear loading was along the X'-axis of the crystal to check the cross-axis sensitivity. The theory predicts no signal due to shear loading; the experiment also showed no shear signal.

ignoring the electromechanical coupling is reasonable for the initial jump. However, we have had to also ignore the contribution of the current i_E in equation (2-24) because we have no way of assessing it. This simplification of the analysis of Section 2.2 is equivalent to neglecting the off-diagonal elements of the permittivity tensor, or the \vec{E} field components normal to the gage thickness direction (see equation 2-22). Without a means of estimating i_E , it is difficult to assign error bars on the measured polarization value.

- (2) The polarization values listed in parenthesis in Table 5 are the shear contributions. In calculating these values, we assumed that the impact surface and the PMMA/LiNbO₃ interface bond can transmit the shear stresses.
- (3) The two sets of calculations reflect the two sets of e_{ij} values inferred from the literature. The main discrepancy is in the e_{22} constant, as discussed in Appendix C. The two set of values used in calculating P_2 from equation (2-23) are as follows:

Orientation	e'_{22} (C/m ²)	e'_{24} (C/m ²)
163° Y-cut	-8 x 10 ⁻³ (Old)	-3.76 (Old)
	-3.49 x 10 ⁻¹ (New)	-3.86 (New)
165.5° Y-cut	-3.58 x 10 ⁻¹ (Old)	-3.85 (Old)
	-7.12 x 10 ⁻¹ (New)	-3.94 (New)

These values are discussed in greater detail in Appendix D.

Comparison of the calculations with the experimental measurements leads to the following conclusions:

- (1) The observed shear contributions to polarization in Experiments 2 and 5* closely match the theoretical values.
- (2) The results of Experiment 2 suggest that there is no cross-axis sensitivity.
- (3) The agreement between the theory and experiment is not good for compression loading. Most of the compression loading data agree better with the old set of constants. However, some

*Experiment 1 is less reliable, as indicated in Section 3.

agree with the new set of constants; no systematic trends are obvious. The calculated compression response for 163° Y-cut crystals also depends markedly on the C_{ij}^D value chosen. For example, using the values in Table 4, the calculated polarization for Experiment 3 in Table 5 is 0.36 and not 0.44.

- (4) These inconsistencies and the inconsistencies among the data themselves (discussed in Section 3) suggest that contributions from the following sources of errors may be important: (a) finite tilt values, (b) deviations from the desired crystal orientation, (c) uncertainties in the knowledge of the piezoelectric constants and C_{12}^D , (d) the extra current term in the rotated-cut derivation discussed in Section 2.2, and (e) the contribution from electromechanical coupling due to tilt, which can introduce an error in the measured current jump e.g. Experiment 6. An estimate of the contributions from the first two sources is presented in the remainder of this section. The contribution from the last two sources can only be assessed after further theoretical work.

4.3 ASSESSMENT OF TILT EFFECTS

We were unable to develop a simple method to estimate tilt effects. Therefore, the analysis described in Appendix E was developed. However, this analysis is not exact because it treats the LiNbO_3 as an isotropic solid. Despite this limitation, we believe that the results of our tilt analysis provide a quantitative assessment. By using the compression and shear wave velocities that are pertinent to our crystal orientations, we can obtain reasonable values of ϵ_2' and ϵ_4' in the LiNbO_3 for use in equation (2-23). Also, the crystal orientations are fairly close to the specific direction.

As indicated in Appendix E, a finite tilt results in a compression and a shear wave inclined at an angle to the impact surface. The faster travelling compression wave reaches the PMMA/ LiNbO_3 interface and produces a compressive stress (σ_2') and a shear stress (σ_4'). We calculated the contribution to polarization from the shear stress (actually, shear strain). To convert the stresses into strains, we used the following moduli for LiNbO_3 : Longitudinal modulus = 2114 kbar and Shear modulus = 986 kbar. These values are equivalent to a longitudinal wave velocity of 6.75 mm/ μs and a shear wave velocity of 4.61 mm/ μs .

Both values are very close to the wave velocities calculated* by using the C_{1j}^D values and equation (B.6).

Because we are approximating the LiNbO_3 as an isotropic crystal, the other stresses will not be matched correctly. In the present analysis this is not important because the polarization contribution due to tilt arises from the ϵ_4' strain caused by the finite tilt. For both orientations (163° and 165.5° Y-cut), ϵ_4' has the same value for a particular impact experiment. To calculate the polarization, P_T' , we used a e_{24}' value of -3.85 C/m^2 . This value is reasonable because the e_{24}' value for the two orientations using either set of constants ranges from -3.76 to -3.94 C/m^2 .

In the analysis presented in Appendix E, we also calculated the effect of the slower travelling shear wave, generated at the impact surface, after it reaches the PMMA/LiNbO_3 interface. The effect of this shear wave is not included in this analysis of tilt effects because we are interested only in calculating the polarization at the first jump.

The results incorporating the effects of tilt are summarized in Table 6. The compressive strains, ϵ_2' , were derived from the oblique plate analysis described in Appendix E, using the longitudinal modulus value cited earlier. Although these values are not used for polarization calculations, they can be compared with the ϵ_2' values cited in Table 3. The shear strains ϵ_4' were calculated from the shear stress due to finite tilt. The tilt contributions to the polarization, P_T' , were calculated from

$$P_T' = -3.85 \epsilon_4' \text{ C/m}^2 \quad (4-2)$$

We interpret the tilt contribution as follows: the P_T' values represent a contribution to polarization that is present in the

*The eigenvalues for the 163° and 165.5° Y-cut orientation are within 0.2 percent of each other, and we use the average calculated values: $6.743 \text{ mm}/\mu\text{s}$ (P-wave) and $4.58 \text{ mm}/\mu\text{s}$ (S-wave).

experiments but not included in the theory. Hence, the P_T' values in Table 6 should be added to the calculated polarization values shown in Table 5. We used the polarization values in Table 5 based on the old e_{ij} constants to add to the P_T' values.* This calculated total is compared with the experimental measurements in the last two columns of Table 6. Except for Experiments 1 and 3, the addition of the tilt contribution improves the agreement between theory and experiment. It is noteworthy that most of the difference in the output of the two gages in Experiment 8 was due to tilt effects. Without tilt effects, the two gages ($Z' = 0^\circ$ and $Z' = 90^\circ$) would appear identical as expected. This result underscores the anomalous response of Experiment 6. Although differences remain between theory and experiment, the results are encouraging.

In Table 6, we did not calculate the tilt correction for the contribution of the shear strain to the polarization values shown in parenthesis in Table 5. First, we wanted to analyze only the initial jump; subsequent results are strongly influenced by the electromechanical coupling. Second, the S-wave due to finite tilt (not due to the shear deformation deliberately introduced by making $\theta \neq 0$ in Figure 2) on arrival at the PMMA/LiNbO₃ interface reduces the shear stress (or strain ϵ_4') to a small value. This effect is completely masked by the arrival of the main shear wave. Also, this result suggests that the tilt error is self-compensating for the shear polarization part. Note that remarks about tilt corrections at late times cannot be considered rigorous because of electromechanical coupling effects.

Comparisons of the measured and calculated polarization values after accounting for tilt effects in an approximate manner are summarized as follows:

*Using the other set would further increase the discrepancy between theory and experiment.

Table 6. Tilt contribution to polarization.^a

Experiment No.	Gage Type	Compressive ^b Strain, ϵ_2 (10^{-3})	Shear ^c Strain, ϵ_4 (10^{-5})	Tilt Contribution P_T (10^{-3} C/m ²)	Polarization (10^{-3} C/m ²)	
					Calculated ^d	Measured ^e
Compression-Only Experiments						
3	163.0° (Z' = 0°)	-3.22	-1.52	0.059	0.5	0.4
(81-2-22)	165.5° (Z' = 0°)	-3.22	-1.52	0.059	1.28	1.65
4	163.0° (Z' = 0°)	-2.30	-3.8	0.146	0.45	0.42
(81-2-23)	165.5° (Z' = 0°)	-2.30	-3.8	0.146	0.99	1.22
6	165.5° (Z' = 0°)	-3.11	-9.01	0.347	1.53	1.93
(81-2-43)	165.5° (Z' = 90°)	-3.11	-3.14	0.121	1.30	2.49
7	165.5° (Z' = 90°)	-3.02	-1.53	0.06	1.2	1.33
(84-542)	163.0° (Z' = 0°)	-3.07	4.53	-0.174	0.24	0.22
(84-543)	163.0° (Z' = 90°)	-3.07	2.61	-0.1	0.32	0.33
Combined Compression and Shear Experiments						
1	163.0° (Z' = 0°)	-3.02	-4.97	0.191	0.57	0.31
(78-2-46)	163.0° (Z' = 0°)	-2.32	-5.31	0.205	0.51	0.56
2	163.0° (Z' = 90°)	-2.32	-6.34	0.244	0.54	1.17
(81-2-15)	163.0° (Z' = 0°)	-3.27	-9.02	0.348	0.78	1.16
(81-2-24)	163.0° (Z' = 0°)					

^aThe gages listed here are the same as those listed in Table 3, and they are in the same order.

^bThe final two columns of this table present an overall comparison of theory and experiment.

^cThe compressive strain values are not used in the calculation; they are to be compared with the fourth column of Table 3.

^dFor Z' = 90°, the shear strain is ϵ_6 .

^eThese values are obtained by adding P_T to the last column in Table 5.

^fSame as the fourth column of Table 5.

- (1) The tilt contributions to polarization are significant because of the large shear sensitivity of the gage.
- (2) In six out of eight measurements, the incorporation of tilt effects reduces the discrepancy between theory and experiment.
- (3) The incorporation of tilt effects indicates that the old set of piezoelectric constants provides a better match to our data. The old set of constants are presented in Appendix D.

The analysis presented here is not exact. An improved analysis requires that the anisotropic response of LiNbO_3 be accounted for in calculating tilt effects. We also believe that our tilt measurements can be improved in future experiments.

4.4 DISCUSSION

The analyses presented in this section have answered some questions but also raised new ones.

On the positive side, the present work has confirmed the large sensitivity of the 163° Y-cut orientation to shear loading relative to compression loading. The one experiment designed to examine sensitivity to cross-axis shear suggests that the gage is not sensitive to cross-axis shear. As predicted, the compression sensitivity of the 165.5° Y-cut orientation is considerably higher than that of the 163° Y-cut orientation. A fairly complete theoretical framework has been developed to quantitatively analyze the gage response to well-defined loading. Detailed comparisons of theoretical predictions and experimental measurements have been presented. For shear loading, the theory and experiment show good agreement (within 3 percent).

On the negative side, quantitative agreement between theory and experiment is not good for compression loading (10 to 50 percent). Some of the inconsistencies among the experimental results have not been completely resolved. The results from Experiment 6 are believed to be anomalous (see Figure 5(f) and 5(g) in Section 3). Similarly, the differences between the first jump for the two gages in Experiment 2 (Table 5) are difficult to understand.

One is tempted to speculate that neglecting of the current i_E term [see equation (2-24)] in converting the current values to polarization may be a major source of error. However, this error is probably systematic because the experimental conditions are fairly similar. The random tilt variations can only explain part of the discrepancy. Hence, we are forced to conclude that the variability in the orientations of the crystals may be causing some of the observed inconsistencies. The supplier assured us that the orientations were within 0.2° . Although we cannot check the gages that have been impacted, the orientations of the remaining gages from that batch were independently measured.* These results indicated that the scatter in orientation ranged between 0° and $\pm 1.5^\circ$. To us this scatter seems high because the supplier[†] of these gages had considerable expertise in crystal orientation. Further experimental work is needed to unequivocally resolve this issue, as indicated in Section 5.

There is also the question of the two sets of piezoelectric constants. The main difference is in the e_{22} constant. The value cited in the literature⁵ (from ultrasonic experiments) is 2.43 C/m^2 . Our analysis of Graham's shock wave data,⁶ described in Appendix C, yields a value of 2.82 C/m^2 . Because the new set of constants (using $e_{22} = 2.82$) are based on impact results, one is tempted to believe these results. However, our present data are better matched by using the old set of constants ($e_{22} = 2.43$). Clearly, the value of e_{22} , because of its large influence on the results, has to be established accurately. There are two deficiencies in the analysis of Graham's data⁶. First, the extent of tilt effects is not known. Second, the conversion of the current jump to polarization does not account for the two-dimensional effect (i_E

* We are grateful to Mr. R. A. Graham of Sandia National Laboratories for these measurements. The standard deviation was estimated to be $\pm 0.5^\circ$ in these measurements.

[†] Now deceased.

term) discussed in Section 2.2. When this latter effect is not properly modeled, the shock response of rotated-cut crystals is suspect. Hence, we recommend using the old set of constants as defined in Appendix D.

An added complexity in interpretation arises because the new e_{22}' value of -0.349 C/m^2 along the 163° Y-cut orientation is comparable to the e_{22}' value based on the old constants but for a crystal misorientation of $\pm 0.2^\circ$ (see Appendix D). There is also the question of difference in the C_{12}^D values reported in References 4 and 5. As indicated at the end of subsections 4.1 and 4.2, this difference can markedly influence the compressive contribution to polarization for the 163° -rotated cut crystals. If the ϵ_4' value used in Equation (2.23) is taken from Table 4 instead of Table 3, the P_2' value for the compressive response of the 163° -rotated cut crystals would be decreased by approximately 15-20 percent.

It is obvious from the above remarks that improved reconciliation between theoretical predictions and experimental measurements will require further experimental and theoretical work, and an improved knowledge of the piezoelectric constant e_{22} and the elastic constant C_{12}^D . Because of the many potential sources of errors, it is hard to proceed further without additional information. The need for resolving the differences between the theoretical measurements and experimental results for developing a gage package and the specific steps to resolve these differences are discussed in the next section.

SECTION 5

CONCLUSIONS AND RECOMMENDATIONS

The objectives of this work, outlined in Section 1.2, have largely been met. A fairly complete theoretical framework has been developed to analyze the response of rotated-cut LiNbO_3 gages. The experimental work, designed to calibrate both the compression and shear response of the gage, showed the need for a better understanding of several effects not originally envisioned. Some of the difficulties encountered in interpreting the results are specific to the shear gage usage, but many of the difficulties are more fundamental. For example, the disagreement between the e_{22} value obtained from the shock work⁶ and the ultrasonic studies⁵ represents a major uncertainty in defining the optimal shear direction. Also, the value of C_{12}^D needs to be established accurately.

The main findings of the present work are summarized below:

- (1) The experimental data on 163° -rotated Y-cut LiNbO_3 confirm the large sensitivity to shear relative to compression. There does not appear to be a cross-axis sensitivity.
- (2) The current output from a 165.5° -rotated Y-cut gage is considerably higher than the output from a 163° Y-cut gage for the same compression loading. This result is in agreement with the theory.
- (3) Because of the large shear sensitivity of the gage, proper interpretation of the experimental data requires that the effects of both tilt and anisotropy be included in the analysis. An elastic-dielectric analysis has been developed for incorporating these effects in a quantitative manner in analyzing the data; including these effects leads to significant changes.
- (4) Experimental measurements of the shear contribution to polarization agree well with theoretical predictions to within 3 percent.
- (5) The quantitative agreement between theory and experiment is not good for compression loading. The inclusion of tilt effects makes a significant difference, but significant discrepancies (10 to 50 percent) remain.

- (6) The theoretical developments presented in this study have pointed out the complexity in analyzing the response of rotated-cut crystals. In particular, it is important to develop a quantitative understanding of the influence of the boundary conditions on the electrical fields, that is, evaluate the two-dimensional electrostatic effects.
- (7) Large electromechanical coupling effects (current ramping) were observed in the experiments, but these have not been modeled. Part of the discrepancy indicated above could be caused by electromechanical effects. Future work should incorporate these effects in the analysis.
- (8) We have developed a theoretical analysis to incorporate electromechanical coupling under combined compression and shear loading. Numerical procedures for analyzing experimental data, similar to the procedures in Reference 15, need to be developed.
- (9) Some of the inconsistencies in the experimental data have not been explained. Theoretical calculations for the 163° Y-cut orientation indicate that small errors in crystal orientations ($\pm 0.2^\circ$) can lead to large errors in the current output for compressive loading. This result suggests the need for an accurate knowledge of the gage orientation.
- (10) The extreme sensitivity of the gage output to crystal orientation for compression loading suggests that the gage orientation that is used should be a compromise between minimizing the compression output and accommodating the practical constraints on crystal orientation tolerances. Fortunately, the piezoelectric constant controlling the shear output is largely insensitive to changes in crystal orientation.
- (11) The optimal shear direction is highly sensitive to the value of the piezoelectric constant e_{22} . Analysis of Graham's impact data⁶ gives an e_{22} value of 2.82 C/m^2 in contrast to the ultrasonic value of 2.43 C/m^2 . This discrepancy needs to be resolved. For example, is it reasonable to neglect i_E in equation (2-24) in analyzing the impact data? The tilt contribution in Graham's experiments is not known. Based on our work, we recommend using an e_{22} value of 2.43 C/m^2 .
- (12) Because the compression response of the 163° Y-cut orientation depends strongly upon the C_{12}^D value, this constant needs to be established accurately.

These findings from the present work have resulted from a detailed examination of the shear gage concept, which was the main objective of this study. We believe that the development of a piezoelectric shear stress gage is a realistic undertaking. However, this development will require additional research to understand the piezoelectric response in detail. Some specific recommendations for further work, including the development of a gage package, are discussed below.

We believe that a basic necessity is to better understand and model the compression response of the gage. This assertion may be questioned because the shear response has been modeled reasonably well. The main reason for developing a better understanding of the compression response is that in most applications the gage will be subjected simultaneously to a compression and a shear stress. Even if the compression stress is independently known, the determination of the shear stress from the gage output requires that the sensitivity to compression stress should be both small and known accurately. This requirement is necessitated by two factors. First, in most applications the compressive stresses are much larger than shear stress. Second, the compressive response of the gage is very sensitive to the orientation of the crystal.

The general approach to studying the compression response of the gage should begin by developing a quantitative solution to the two-dimensional electrostatic problem presented in Section 2.2. The highest priority should be given to this assessment of the effects of the boundary conditions because it is necessary for evaluating the complete response of rotated-cut crystals including the current i_E in Eq. (2-24).

This analysis should be verified by modeling both shunted and shorted gage data for identical impact conditions and comparing these predictions with laboratory measurements on such gages. Additionally, numerical methods for incorporating into the data analysis the electro-mechanical coupling effects described in Section 2.3 should be developed.

If these tasks can be successfully completed, then further laboratory impact experiments should be conducted to determine the e_{22} constant very accurately. These experiments need to be of higher

precision than the present experiments and should incorporate the following changes: shunted or shorted gages should be used depending on the results of the electrostatic analyses; compression-only experiments without a buffer plate should be performed; the impactor material should be more nearly elastic; improved measurements of impact tilt should be obtained; crystal orientation should be determined accurately by several independent measurements. After the e_{22} constant is determined, the recommendation indicated in item (10) above should be performed. The crystal orientation that is selected should then be calibrated carefully under compressive loading.

Regarding the gage package development, an important first step is to develop analytic or numerical methods for approximating the stress and strain distributions expected in the gage in some typical applications. Because of the anisotropic response of the crystal, this is an involved undertaking.* Once the mechanical quantities are known, the polarization and electric field distributions can be determined. Just as for studying the compression response of LiNbO_3 in the laboratory, in developing a field gage package, it is important to develop a good understanding of the electrostatic response of the gage for the appropriate boundary conditions to evaluate deviations from the idealized response.

We cannot overemphasize the importance of identifying and understanding all the various contributions to the gage output before using the gage. Without a detailed understanding of these contributions, it will be nearly impossible to analyze the gage data.

Calculation of the mechanical quantities indicated above will also be useful in evaluating the inclusion problem: How is the mechanical

*The development of a numerical method to address this problem would also be useful in incorporating the crystal anisotropy in the tilt analysis.

state of the sensor related to the measurement of interest? The answer to this question is central to all gage measurements.

Finally, the development of a piezoelectric shear gage is dependent upon extending our basic understanding of piezoelectric phenomenon as indicated in this section. Hence, it is difficult to project accurately the likelihood of success or time duration for completion of an effort to develop a field gage package.

SECTION 6

LIST OF REFERENCES

1. Proceedings of the Conference on "Instrumentation for Nuclear Weapons Effects," M. J. Frankel, Editor, DNA-TR-82-17-V1 and V2 (July 1982).
2. Y. M. Gupta and W. J. Murri, "Development of a Piezoelectric Shear Stress Gage", DNA 4870F (1978).
3. Proceedings of the Institute of Radio Engineers, 14, 1378 (1949).
4. A. W. Warner, M. Onoe, and G. A. Coquin, J. Acoust. Soc. Amer. 42, 1223 (1967).
5. R. T. Smith and F. S. Welsh, J. Appl. Phys. 42, 2219 (1971).
6. R. A. Graham, J. Appl. Phys. 48, 2153 (1977).
7. F. W. Nielson, in Response of Metals to High Velocity Deformation (Interscience Publishers, New York, 1961), p. 273.
8. R. A. Graham, J. Appl. Phys. 32, 555 (1961).
9. O. E. Jones, F. W. Neilson, and W. B. Benedick, J. Appl. Phys. 33, 3224 (1962).
10. R. A. Graham, F. W. Neilson, and W. B. Benedick, J. Appl. Phys. 36, 1775 (1965).
11. R. A. Graham and G. E. Ingram, J. Appl. Phys. 43, 826 (1972).
12. R. A. Graham, Phys. Rev. B, 6, 4779 (1972).
13. R. A. Graham and R. D. Jacobsen, Appl. Phys. Lett. 23, 584 (1973).
14. P. J. Chen, L. Davison, and M. F. McCarthy, J. Appl. Phys. 47, 4759 (1976).
15. R. J. Lawrence and L. W. Davison, in Proceedings of the Symposium on Applications of Computer Methods in Engineering, L. C. Wellford, Jr., Editor, (University of Southern California, 1977).
16. R. A. Graham, J. Phys., Chem. Solids 35, 355 (1974).

17. The electrostatic equations presented here can be found in a standard text such as J. D. Jackson, Classical Electrodynamics (John Wiley & Sons, Inc., New York, 1962).
18. W. G. Cady, Piezoelectricity (Dover Publications, Inc., New York, 1964).
19. F. Borgnis, Phys. Rev. 98, 1000 (1955).
20. R. N. Thurston, in Handbuch Der Physik, Vol. VI a/4, S. Flugge, Editor, (Springer-Verlag, Berlin, 1974).
21. W. P. Mason, Crystal Physics of Interaction Processes (Academic Press, New York, 1966).
22. Y. M. Gupta, Calculation of P and S Waves (COPS): Wave Propagation Program (unpublished).
23. R. A. Graham, J. Appl. Phys. 46, 1901 (1975).
24. L. M. Barker and R. E. Hollenbach, J. Appl. Phys. 41, 4208 (1970).
25. Y. M. Gupta, J. Appl. Phys. 51, 5352 (1980).
26. Y. M. Gupta, D. D. Keough, D. R. Walter, K. C. Dao, D. Henley, and A. Urweider, Rev. Sci. Instr. 51, 183 (1980).
27. P. L. Flanders, "Test Sites and Instrumentation," Nuclear Geoplosics, Part III, DNA Report, DASA - 1285 (1964).
28. P. L. Coleman, et al., "Review and Development of Ground Motion and Airblast Instrumentation," DNA 4036F (1976).
29. Y. M. Gupta, Appl. Phys. Letters 29, 694 (1976).
30. Y. M. Gupta, "Development of a Method for Determining Dynamic Shear Properties," Draft Final Report submitted to DNA under Contract DNA 001-76-C-0384 (May 1978).
31. R. A. Graham, "Lithium Niobate Stress Transducers," in Sandia Technology, Sandia Laboratories Report SAND75-0426 (1975).
32. R. P. Reed, "The Sandia Field Test Quartz Gage, Its Characteristics and Data Reduction," Sandia Laboratories Report SC-CD-71-4529 (1971).
33. D. B. Hayes and Y. M. Gupta, Rev. Sci. Instr. 45, 1554 (1974).
34. D. R. Grine, "Hardened Quartz Gages for Ground Shock and Airblast Measurements," Presentation at DNA meeting, Vicksburg, Mississippi (October 1975).

35. W. P. Mason, Piezoelectric Crystals and Their Applications to Ultrasonics (D. Van Nostrand Company, New York, 1950).
36. D. A. Berlincourt, D. R. Curran, and H. Jaffe, in Physical Acoustics, Vol. I (A), Ed. W. P. Mason (Academic Press, New York, 1964); also see articles in subsequent volumes.
37. F. W. Neilson, et al., Les Ondes de Detonation (Editions due Centre National de la Recherche Scientifique, Paris, 1962).
38. R.F.S. Hearmon, An Introduction to Applied Anisotropic Elasticity (Oxford University Press, London, 1961).
39. J. N. Johnson, J. Appl. Phys. 42, 5522 (1971).
40. J. N. Johnson, J. Appl. Phys. 43, 2074 (1972).
41. G. R. Fowles, Private Communication (1980).

APPENDIX A

SYNOPSIS OF THE FEASIBILITY STUDY*

A.1 MOTIVATION AND OBJECTIVES

The determination of dynamic stresses and loads is fundamental to much of DNA field testing. The need for these measurements has led to the development and use of many different types of stress, particle velocity, acceleration, and displacement gages.^{27,28} Despite the large variety and quantity of existing dynamic measurements, field measurements of shear stress (or loads) are lacking. The inability to make dynamic shear measurements is an important shortcoming because shear measurements are needed for determining strength properties of both soils and structures in underground tests.

The need for shear measurements is well recognized by most workers involved in dynamic measurements. However, this development has been lacking due to the complexity of the problem: The desired shear stress gage must be usable under complex loading conditions, and suitable methods are needed to calibrate the gage to well-defined shear stresses. Most of the previous field gage techniques have been extended from laboratory concepts and measurements, but laboratory studies are also lacking in dynamic shear measurements.

The objective of our work was thus to examine the feasibility of developing a piezoelectric shear stress gage for use in DNA field tests. A combined analytic and laboratory experimental effort was

*The Introduction and Summary section of our feasibility work described in the DNA Report 4870F (December 1978) is presented here. To aid the reader, this Appendix has its own set of references. Because the report was written more than five years ago, not all the statements reflect the author's current thoughts.

undertaken to meet this objective. The bases for this work are recent developments at SRI relating to the study of dynamic shear properties of solids^{29,30} and the use of piezoelectric gages in studying dynamic compressive stresses.^{10,13,31-34}

A.2 BACKGROUND AND APPROACH

Piezoelectricity and the use of piezoelectric transducers and devices in acoustic applications is a major field of study.^{18,35,36} However, the use of piezoelectric transducers for measuring large stress amplitudes under dynamic loading is a more recent and specialized topic.³⁷ Studies during the past decade have led to the development of stress transducers for studying dynamic compressive stresses up to tens of kilobars in materials subjected to impact, explosive, and radiation loads.^{10,13,31-34} Studies by Graham and co-workers have clarified piezoelectric response at high stresses and established bounds on the use of stress gages.^{11,12,23} The formulation of nonlinear piezoelectric constitutive relations has also received increased attention.^{12,20} In many laboratory and field measurements, α -quartz is used as the gage material, but recent studies have also been conducted using lithium niobate (LiNbO_3).⁶ For low stresses (below 10 kbar), the larger electrical output of LiNbO_3 is advantageous.

Piezoelectric gages are used in two modes. The current or short-circuit mode measures fast rise time, short-duration stress pulses, and the useful recording time of the gage is the wave transit time through the gage. Laboratory shock wave experiments with zero lateral strains commonly use the current mode. In the charge or open-circuit mode, the gage is used to record slower rise time, long-duration (millisecond) pulses. This second mode is more commonly used under field conditions for recording stress pulses with wavelengths much greater than the gage thickness. That is, the gage in the charge mode acts like a static transducer in equilibrium with the surrounding material stresses. No fundamental differences exist between these modes with regard to the piezoelectric response, and the laboratory results are applicable to

field usage.* The differences in these modes are operational and reflect the mechanical boundary conditions most suited for using the gages in different applications. Further discussion of these two operational modes is given in Reference 31.

Despite the many laboratory and field developments in the use of the above-cited modes, measurements to date have been performed exclusively for compressive stresses. In the following paragraphs we discuss our approach for developing a piezoelectric shear stress gage for use in dynamic loading conditions in the presence of complex stresses.

The two general requirements in the development of a shear gage are: (a) knowledge of a material phenomenon (e.g., appropriate piezoelectric response) relating shear stress to a measurable quantity and (b) the ability to calibrate the gage for known shear stresses.

The first requirement is easily satisfied, in principle, because of the existence of many shear transducers in the field of ultrasonics.³⁵ Because the compressive stress gage is an extension of ultrasonic concepts, these concepts can be explored for the development of a shear stress gage. There are, however, complicating factors that do not allow a simple extension of ultrasonic concepts. In ultrasonics, pure shear waves are commonly created by using the converse piezoelectric effect. Thus, the measuring transducer is subjected to a pure shear motion. In most dynamic loading situations, a complex stress state exists--that is, superposed compression and shear states. Furthermore, because of the large stresses, the material in which the gage is placed undergoes inelastic deformations, and the relative magnitudes of the compression and shear stresses are expected to vary over the time range of interest. For the gage measurements to be useful, the electrical signal from the gage should be uniquely related only to the shear stress of interest. Because of the tensorial nature of piezoelectricity, this requirement is not met by most of the ultrasonic shear transducers.

*The electromechanical coupling will be different for the two cases.

To satisfy the above requirement in the presence of complex stresses (e.g., combined compression and shear), we developed an analytic approach that consists of simultaneously examining wave propagation and piezoelectric relations for materials of interest. The analytic approach chosen is general and provides criteria for determining the needed gage designs. We examine all possible crystal orientations to obtain the optimal directions for piezoelectric response and to determine pure mode directions ("specific directions") for stress wave propagation.¹⁹ Once the optimal gage designs have been analytically evaluated, we can conduct experiments to verify and calibrate these gage designs.

The second requirement, calibration of the gages, is met by experimentally studying the gage response to one-dimensional compression and shear waves using the recently developed IMPS* experimental facility.[†] In this method, the specimens are subjected to varying but controlled amounts of compression and shear stresses. By subjecting the gages to pure compression, we can ensure that there is not electrical output from the compressive stress. Increased amounts of shear stresses can then be superposed to calibrate the response to shear. Because this is a feasibility study, the present scope of the work is intended to experimentally verify the theoretical concepts. A detailed calibration would be performed after the feasibility of the shear gage has been established.

A.3 SUMMARY

The objective of the work reported here was to examine the feasibility of developing a piezoelectric shear stress gage sensitive only to shear loading. Using a combined analytic and experimental approach, we successfully demonstrated the feasibility of developing such a gage.

*Internal Measurement of P and S Waves.

[†]Work performed under DNA Contract DNA001-76-C-0384.

A simplified but general analysis of the mechanical and piezoelectric response was performed to provide criteria for a suitable shear gage. Mechanical wave propagation analysis in anisotropic electric media showed that, in general, three waves are propagated: one quasi-longitudinal and two quasi-transverse waves. Only for "specific directions" are the propagated waves purely longitudinal and/or purely transverse. To avoid mechanical coupling of strains, the gage thickness direction should be along a specific direction. The piezoelectric analysis showed that electrical polarization for the desired gage should be one-dimensional and along the gage thickness direction. Furthermore, this electrical polarization should be caused only by shear loads and not compressive loads.

The adequacy of a particular crystal type for meeting the above criteria can be easily and efficiently assessed by numerical calculations of the specific directions and the "piezoelectric matrix" for all possible orientations about the three crystallographic axes. When these calculations were performed for the different orientations of α -quartz and lithium niobate (LiNbO_3), only the 163° Y-cut LiNbO_3 appeared suitable for use as a shear gage. For this orientation, the shear-to-compression sensitivity ratio for the polarization is enhanced by more than two orders of magnitude. Furthermore, this orientation deviates only 2° from a specific direction and therefore has minimal mechanical coupling.

Impact experiments were conducted under combined compression and shear to verify the use of 163° Y-cut LiNbO_3 as a shear stress gage. The results of these experiments show that the gage, as desired, had negligible sensitivity to compressive stress and a very large sensitivity to shear stress.

Further development of gages for routine use in laboratory and field measurements requires calibration experiments that can be performed using the same impact facility. In addition, field usage requires development of proper packaging techniques.

APPENDIX B

WAVE PROPAGATION ALONG NONSPECIFIC DIRECTIONS

An important aspect of the present work involved elastic wave propagation along different crystal orientations. In this Appendix, we briefly describe and summarize analytic developments pertinent to the analysis of our experimental results. Studies by Borgnis,¹⁹ Hearman,²⁷ and Johnson²⁸ serve as a basis for the developments presented here.

As indicated in Section 2.2, the mechanical wave propagation cannot be uncoupled from the external electric circuit for a crystal such as LiNbO₃. However, the initial jump can be analyzed using elastic constants at constant electric displacement (C_{ij}^D). Here, we present some general developments, and calculations of specific directions; then we describe numerical calculations for analyzing impact data along non-specific directions. The relationship between C_{ij}^D and C_{ij}^E is also derived in this Appendix.

The rotation transformation of coordinate axes defined and used in this Appendix is not consistent with the other parts of the report.

B.1 GOVERNING EQUATIONS

We consider two coordinate systems:²⁸ x_i corresponds to the crystallographic system and x'_i corresponds to the wave propagation system. Wave propagation is described by

$$\rho \frac{\partial^2 u'_i}{\partial t^2} = C'_{ijkl} \frac{\partial^2 u'_k}{\partial x'_j \partial x'_l} \quad (\text{B-1})$$

where

ρ = density

u'_i = material displacement along the x'_i -direction



t = time
 C'_{ijkl} = second-order elastic constants in the primed system.

The transformation matrix between the unprimed and primed system is given by

$$a_{mn} = \vec{e}'_m \cdot \vec{e}'_n \quad (\text{B-2})$$

where \vec{e}'_m and \vec{e}'_n are unit vectors along the x'_m and x'_n directions.

Plane wave solutions for equation (B-1) for wave propagation along a direction \vec{b}' are given by

$$u'_i = A'_i f(t - b'_i x'_i / c') \quad (\text{B-3})$$

where

A'_i = displacement amplitude along x'_i
 c' = wave velocity.

Substitution of equation (B-3) in (B-1) gives the following equations:

$$(\lambda'_{ik} - \delta_{ik} \rho c'^2) A'_k = 0 \quad (\text{B-4})$$

where

$$\lambda'_{ik} = b'_j b'_l C'_{ijkl} \quad (\text{B-5})$$

and δ_{ij} is the Kronecker delta. For nontrivial solutions of equation (B-4), we have the condition

$$|\lambda'_{ik} - \delta_{ik} \rho c'^2| = 0 \quad (\text{B-6})$$

Equation (B-6) has three possible eigenvalues, each of which corresponds to an eigenvector A'_m . Each of the eigenvalues and eigenvectors represent the wave velocity and displacement amplitude associated with one of the three waves. These displacements are always mutually

orthogonal but can have an arbitrary orientation with respect to the wave propagation direction \vec{b}' . Only for specific directions (or isotropic materials) are the displacement directions either parallel (longitudinal waves) or perpendicular (shear waves) to the direction of wave propagation.¹⁹ In general, there is one quasi-longitudinal wave and two quasi-transverse waves.

In our experiments we are subjecting the gage to externally applied compressive and shear stresses. If the gage output is to be related to a particular stress component (shear stress in the present case), then coupling of the stresses within the gage must not occur. For the linear elastic behavior considered here, this coupling can arise only as a result of the anisotropy of the crystal. Therefore, the crystals used for gage development should be oriented along the specific directions for the compressive and shear waves of interest in our experiments.

In the remainder of this Appendix we restrict our analysis to the crystallographic Y-Z (X_2 - X_3) plane of LiNbO_3 crystals.

B.2 WAVE PROPAGATION IN THE Y-Z PLANE OF LiNbO_3

Let the direction of wave propagation be $\vec{b}' = (0, b_2, b_3)$. The components of λ'_{ik} of (B-5) are given by

$$\lambda'_{11} = b_2^2 (C_{11} - C_{12})/2 + b_3^2 C_{44} + 2b_2 b_3 C_{14}$$

$$\lambda'_{22} = b_2^2 C_{11} + b_3^2 C_{44} - 2b_2 b_3 C_{14}$$

$$\lambda'_{33} = b_2^2 C_{44} + b_3^2 C_{33}$$

$$\lambda'_{23} = b_2^2 C_{14} + b_2 b_3 (C_{13} + C_{44})$$

$$\lambda'_{12} = 0$$

$$\lambda'_{13} = 0$$

(B-7)

The eigenvalues Q ($= \rho c'^2$) of equation (B-6) are given by

$$Q_1 = \lambda'_{11} \quad (B-8)$$

$$(\lambda'_{22} - Q)(\lambda'_{33} - Q) - \lambda'^2_{23} = 0 \quad (B-9)$$

The solution of equation (B-9) gives the two eigenvalues Q_2 and Q_3 . Q_1 has an eigenvector along $(1, 0, 0)$; of the three waves that can propagate in any particular direction in the Y-Z plane, one is always pure shear wave with particle motion along $(1, 0, 0)$. The eigenvectors corresponding to Q_2 and Q_3 can be calculated using the usual procedures. We have written a program that calculates the eigenvalues and eigenvectors for wave propagation in the Y-Z plane for all orientations. Wave velocities needed in our work were calculated using this program. This program is also useful in determining the effects of small deviations from the specific directions.

In our work we have used the general procedure described by Borgnis¹⁹ for calculating specific directions. A vector \vec{p} that represents a specific direction is both parallel to \vec{b}' and is an eigenvector of equation (B-6). Hence, \vec{p} is one of the form $(0, p_2, p_3)$, satisfying the relation

$$\vec{p} \times \vec{b}' = p_2 b'_3 - p_3 b'_2 = 0 \quad (B-10)$$

and its components are given by

$$\lambda'_{22} b_2 + \lambda'_{23} b_3 = p_2 \quad (B-11)$$

$$\lambda'_{23} b_2 + \lambda'_{33} b_3 = p_3$$

Substituting equation (B-11) in (B-10) and using the values of λ'_{ik} from equation (B-7), we can write the equation for specific directions in the Y-Z plane

$$\left(\frac{b_3}{b_2}\right)^3 (C_{33} - 2C_{44} - C_{13}) + 3C_{14} \left(\frac{b_3}{b_2}\right)^2 + \frac{b_3}{b_2} (C_{13} - C_{11} + 2C_{24}) - C_{14} = 0 \quad (\text{B-12})$$

The solution to this cubic equation gives the specific directions. Using the C_{ij}^D values from Warner et al.,⁴ we calculated the three specific directions in the Y-Z plane for LiNbO_3 as follows:

$$(0, 165.44^\circ, 75.44^\circ)$$

$$(0, 45.99^\circ, -44.01^\circ)$$

$$(0, 104.08^\circ, 14.08^\circ)$$

B.3 IMPACT CALCULATIONS FOR ARBITRARY DIRECTIONS

Johnson²⁸ has described an analytic method for calculating the impact response of anisotropic solids. He was also the first to suggest the use of a Y-cut quartz crystal for generating large-amplitude compression and shear waves in other materials. In our present work we need to analyze the impact response of various rotated-cut crystals. Unlike Johnson, we chose to use a one-dimensional wave propagation program to perform the needed calculations. This numerical method is briefly described below.

Most one-dimensional wave propagation programs are restricted to uniaxial strain problems. The COPS code²² was developed to include both compression and shear wave propagation in solids. However, the code's treatment of the governing equations is not completely general, and the material is assumed to be isotropic. In adapting this program to our present needs, we had to make two changes: we generalized the treatment of the governing equations and wrote a subroutine to incorporate an

anisotropic constitutive relation. In conformity with the rest of our work, we are restricting our development to small strains. Changes to incorporate finite strain for the elastic deformations considered here are straightforward.

The direction of wave propagation is along the x_1' -axis.* The governing equations for the generalized one-dimensional wave propagation can be written as

$$\frac{\partial \sigma'_{11}}{\partial x_1'} = \rho \left(\frac{\partial v_1'}{\partial t} \right) \quad (\text{B-13})$$

$$\frac{\partial \epsilon'_{11}}{\partial t} = \frac{\partial v_1'}{\partial x_1'} \quad (\text{B-14})$$

$$\frac{\partial \epsilon'_{1i}}{\partial t} = \frac{1}{2} \left(\frac{\partial v_i'}{\partial x_1'} \right) \quad ; \quad i \neq 1 \quad (\text{B-15})$$

$$\rho \left(\frac{\partial \underline{\epsilon}}{\partial t} \right) = \sigma'_{1i} \left(\frac{\partial v_i'}{\partial x_1'} \right) \quad (\text{B-16})$$

Here, ρ is density, v_i' is the particle velocity (\dot{u}_i'), and $\underline{\epsilon}$ is the specific internal energy. The energy equation is not used in the remainder of our discussion.

The artificial viscosity relations are generalized by defining the viscous stress as follows²⁹ (repeated index notation is not used):

$$q'_{1i} = \rho \left[M_i (\Delta x_1') \left| \frac{\partial \dot{u}_i'}{\partial x_1'} \right|^2 + N_i (\Delta x_1') \left| \frac{\partial \dot{u}_i'}{\partial x_1'} \right| \right] \quad (\text{B-17})$$

M_i and N_i are coefficients for quadratic and linear viscosity, respectively; $\Delta x_1'$ is the spatial increment in the wave propagation solution. The viscous stresses are used in the usual manner.²⁹

*We chose this axis to conform to the existing notation in the COPS program. In using the results for our work, indices have to be changed appropriately.

The constitutive equation in the crystallographic system, assuming isentropic deformations is written as

$$\sigma_{ij} = C_{ijkl} \epsilon_{kl} \quad (\text{B-18})$$

This is the usual form of the linear elastic relation and is derived by expanding the internal energy function about an initial state. The elastic constants used in our calculations assume a constant electric displacement: C_{ijkl}^D .

Equation (B-18) can be used in the wave propagation program either by transforming equation (B-18) to the primed system or by transforming stresses and strains back and forth between the two systems. We found the latter procedure to be convenient. The subroutine ANELAS, written to implement this procedure*, consists of the following steps:

- (1) Transform the strains in the x_i' -system obtained from equations (B-14) and (B-15) into the crystallographic (x_i) system.
- (2) Change the strains into the matrix notation.
- (3) Evaluate stresses using the matrix form of equation (B-18).
- (4) Convert the stresses into the tensor notation and transform them back into the x_i' -system for use in the momentum equations (B-13) for the next time increment.

The conversion between the matrix and tensor notation can be avoided by developing a procedure for transformation using the matrix notation.

To minimize the modifications to the wave propagation program, we always chose x_1' -axis as the direction of wave propagation. This restriction coupled with the IRE convention³ for rotated-cut crystals leads to the following rotation transformation matrices.

*This subroutine is valid for crystals of three of the five classes of the trigonal system and for all crystals of higher symmetry.

Rotation about x_1 -axis: This notation defines the rotated Y-cut crystals. The x_1 - and x_3' -axes are taken to be coincident. The transformation matrix for going from the crystallographic to the primed system is given by

$$a_{ij} = e'_i e_j = \begin{bmatrix} 0 & \cos\theta & \sin\theta \\ 0 & -\sin\theta & \cos\theta \\ 1 & 0 & 0 \end{bmatrix} \quad (\text{B-19})$$

where θ the angle of rotation about the x_1 -axis. For most of our calculations, this rotation matrix was used with ($\theta = 163^\circ$ or 165.5°). The inverse transformation is given by the transpose of the matrix in (B-19). Thus, $x'_i = a_{ij} x_j$ and $x_i = a_{ji} x'_j$.

The results of the numerical calculation can be adapted to the convention used in the main text of the report by incrementing, as follows: $1 \rightarrow 2, 2 \rightarrow 3, 3 \rightarrow 1$.

Rotation about the x_2 -axis: The x_2 - and x_3' -axes coincide. The transformation matrix for going from the crystallographic system to the primed system is given by

$$a_{ij} = \begin{bmatrix} \sin\theta & 0 & \cos\theta \\ \cos\theta & 0 & -\sin\theta \\ 0 & 1 & 0 \end{bmatrix} \quad (\text{B-20})$$

The inverse transformation is given by the transpose of this matrix.

Rotation about the x_3 -axis: The x_3 - and x_3' -axes coincide. The transformation matrix analogous to the previous matrices is given by

$$a_{ij} = \begin{bmatrix} \cos\theta & \sin\theta & 0 \\ -\sin\theta & \cos\theta & 0 \\ 0 & 0 & 1 \end{bmatrix} \quad (\text{B-21})$$

The inverse transformation is given by the transpose of this matrix.

Several impact situations were simulated to ensure that the numerical procedure was correct. One particular calculation involved the simulation of Johnson's²⁸ analytic solution for the case of Y-cut quartz being impacted by X-cut quartz. In Figure B.1 the free-surface velocity-time profiles using Johnson's notation are compared with his analytic solution. As expected, the numerical solution showed the rounding due to the incorporation of artificial viscosity. The amplitudes are identical even for the small particle velocity component, v_2' . The wave velocities are in excellent agreement when the midpoint in the numerical solution is used.

B.4 RELATION BETWEEN C_{ij}^D AND C_{ij}^E

The paper by Smith and Welsh⁵ lists only the elastic constants at constant electric field C_{ij}^E . Because we need C_{ij}^D in our calculations, the relation between the two sets of constants is derived below. Taking the electric field and the strains as the independent variables, we write

$$\sigma_{ij} = \sigma_{ij}(E_m, \epsilon_{kl}) \quad (B-22)$$

Differentiating with respect to strains and keeping the displacement field constant, we have

$$\left(\frac{\partial \sigma_{ij}}{\partial \epsilon_{kl}} \right)_D = \left(\frac{\partial \sigma_{ij}}{\partial \epsilon_{kl}} \right)_{E_m} + \left(\frac{\partial \sigma_{ij}}{\partial E_m} \right)_\epsilon \left(\frac{\partial E_m}{\partial \epsilon_{kl}} \right)_D \quad (B-23)$$

Using the Maxwell relations - $(\partial \sigma_{ij} / \partial E_m) = (\partial D_m / \partial \epsilon_{ij})$, we obtain

$$C_{ijkl}^D = C_{ijkl}^E - \left(\frac{\partial D_m}{\partial \epsilon_{ij}} \right) \left(\frac{\partial E_m}{\partial \epsilon_{kl}} \right)_D \quad (B-24)$$

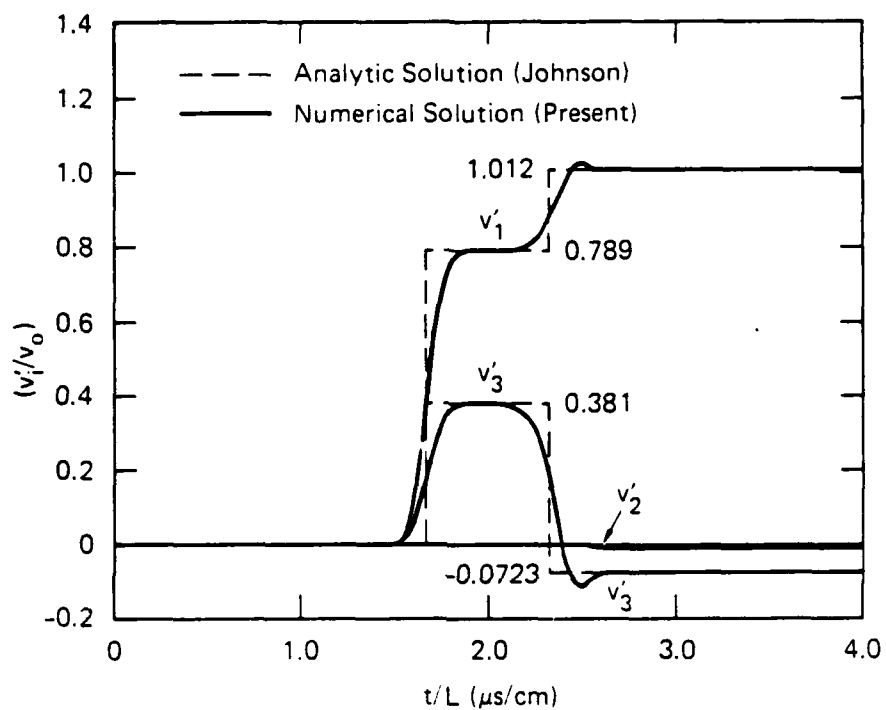


Figure B.1. Free-surface velocity in Y-cut quartz impacted by X-cut quartz. (The particle velocities have been normalized with respect to the impact velocity, and the propagation time has been divided by the sample thickness. For this calculation the direction of wave propagation was chosen to be along the x'_1 -axis in conformity with Johnson's notation. Note the small value of v'_2 .)

Because of the summation over "m" in the last term and because the permittivity is a tensor, care must be exercised in simplifying equation (B-24). For principal cuts in trigonal crystals, the permittivity tensor has only diagonal terms, and equation (B-24) can be simplified easily. Using the matrix notation and the definition of the piezo-electric constants, we can write* (no summation convention)

$$C_{\alpha\beta}^D = C_{\alpha\beta}^E + \frac{e_{1\alpha} e_{1\beta}}{\epsilon_{11}^\epsilon} + \frac{e_{2\alpha} e_{2\beta}}{\epsilon_{22}^\epsilon} + \frac{e_{3\alpha} e_{3\beta}}{\epsilon_{33}^\epsilon} \quad (\text{B-25})$$

where ϵ_{ij}^ϵ is permittivity at constant strain. In writing equation (B-25), the following relation involving partial derivatives is useful:

$$\left(\frac{\partial x}{\partial y}\right)_z \left(\frac{\partial y}{\partial z}\right)_x \left(\frac{\partial z}{\partial x}\right)_y = -1 \quad (\text{B-26})$$

We emphasize that equation (B-25) was derived by assuming that the electrical permittivity tensor has a diagonal form. Adapting equation (B-25) to rotated cuts requires care.

In Table B-1, we present the C_{ij}^D values calculated from the C_{ij}^E values of Smith and Welsh. To check our calculations, we also calculated the C_{ij}^D values using the C_{ij}^E values of Warner et al. Except for C_{12}^D , our calculated C_{ij}^D values match those of Warner et al.

*After equation (B-24) is written for a few terms, the general relation can be easily deduced.

Table B-1. Elastic constants at constant displacement.

C_{ij}^D (10^{11} N/m ²)	Smith and Welsh (Ref. 5)	Warner et al. (Ref. 4)
C_{11}^D	2.183	2.19
C_{12}^D	0.425	0.371
C_{13}^D	0.764	0.76
C_{14}^D	-0.148	-0.147
C_{33}^D	2.495	2.52
C_{44}^D	0.956	0.95

APPENDIX C

DETERMINATION OF PIEZOELECTRIC CONSTANTS FOR LiNbO_3

Graham⁶ performed an impressive series of impact experiments on three different orientations of LiNbO_3 crystals: Z-cut, Y-cut, and 36°-rotated Y-cut samples. His experiments with the Z-cut LiNbO_3 provide a direct determination of the e_{33} constant. Using the measured e_{33} value and the e_{31} value cited in the literature,* Graham also calculated the e_{22} and e_{15} constants from his Y-cut and 36°-rotated Y-cut data. Table C-1 lists the constants reported by Graham,⁶ Smith and Welsh,⁵ and Warner et al.⁴ Constants from other studies are listed in Table VI of Graham's paper.

In most of our work, we used the results of Smith and Welsh⁵ except for the e_{33} constant for which we used Graham's value.⁶ This was a reasonable procedure because the differences in the other two constants are small. In Appendix D we use these values to calculate the e'_{ij} matrix for rotated cuts of interest. Using all the constants from Graham's work gives 163.6° Y-cut as the optimal direction for a shear gage rather than the 163° Y-cut orientation that we used in our work. This difference borders on the accuracy with which these crystals can be cut.

* Because Graham's data were not appropriate for determining e_{31} , he used the e_{31} value given by Smith and Welsh.⁵ Because e_{31} is small, the other constants are not very sensitive to its value.

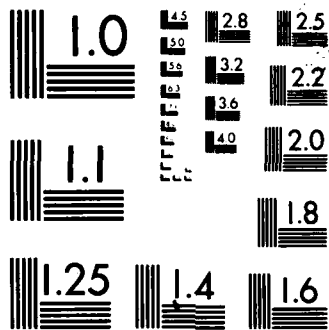
Table C-1. Second-order piezoelectric stress constants (C/m^2).

Author	e_{22}	e_{33}	e_{15}	e_{31}
Warner et al., 1967 (Ref. 4)	2.5	1.3	3.7	0.2
Smith and Welsh, 1971 (Ref. 5)	2.43	1.33	3.76	0.23
Graham, 1977 (Ref. 6)	2.37	1.80	3.83	0.23*

When analyzing our impact data, we realized that the analysis of wave propagation in a nonspecific direction requires a general anisotropic analysis. Such an analysis for one-dimensional wave propagation is discussed in Appendix B. In analyzing the Y-cut and 36° -rotated Y-cut crystals, Graham⁶ used a uniaxial strain analysis. Although his analysis was approximate, the small deviation from uniaxial strain was assumed to be insignificant. We reanalyzed the Y-cut and the 36° -rotated Y-cut data of Graham using the anisotropic analysis presented in the last Appendix. Our procedure, described below, leads to different values for e_{22} and e_{15} than those obtained by Graham.

For Y-cut and 36° -rotated Y-cut crystals a normal impact results in a quasi-longitudinal and two quasi-shear waves, not simply a longitudinal wave (uniaxial strain). For describing the response of these crystals, we consider the following coordinate system: X_1' is along the crystallographic X_1 -axis, X_2' is along the gage thickness direction, and X_3' is chosen to form a right-handed coordinate system.

* See footnote on previous page.



MICROCOPY RESOLUTION TEST CHART
NATIONAL BUREAU OF STANDARDS-1963-A

For plate impact loading, all the quantities vary only along the X_2' -direction and the strain tensor has three independent components: ϵ'_{22} , ϵ'_{21} ($= \epsilon'_{12}$), and ϵ'_{23} ($= \epsilon'_{32}$).

The polarization along the gage thickness direction, P_2' , can be written using the matrix notation*

$$P_2' = e'_{22} \epsilon'_{22} + e'_{24} \epsilon'_{44} \quad (2-23)$$

There is no contribution from the $e'_{26} \epsilon'_{66}$ term because e'_{26} is zero. In his approximate analysis Graham⁶ ignored the contribution of the second term in equation (2-23). Although ϵ'_{44} may be small, the large value of the piezoelectric constants requires that both terms be considered in analyzing the data.

Instead of analyzing all of Graham's experiments, we used the following averaging procedure.

- (1) Because we are not interested in constants beyond second order we used the six experiments for each orientation that gave a linear polarization-strain curve. The polarization/strain ratio was averaged over the six experiments to account for experimental scatter. These values, in Graham's notation, are as follows:

$$\begin{array}{l} \frac{P_2}{\eta} \Big|_{\text{Y-cut}} = -2.38 \text{ C/m}^2 \\ \frac{P_2}{\eta} \Big|_{36^\circ\text{-rotated}} = -4.65 \text{ C/m}^2 \end{array}$$

where η is a measure of finite strain.

- (2) One experiment for each cut that gave a P_2/η value close to each of these values was selected for simulation using the

*The difficulty of relating the current output to the polarization for a rotated-cut, discussed in Section 2.2, is ignored here as it was in Section 4.

anisotropic analysis. For the Y-cut crystals, we chose experiment No. Q-1056 that gave a value of 2.39, and for the 36°-rotated Y-cut crystals, we chose experiment No. Q-1095 that gave a value of 4.64. Using the average polarization/strain values given above, we calculated the polarization values for each of these two experiments. This procedure allows us to average over the various experiments and keep the polarization calculations independent of Graham's strain values.

Using our modified COPS code,²² we numerically calculated the mechanical variables for the two experiments cited above. The LiNbO₃ elastic constants C_{ij}^D used in these calculations were derived from the C_{ij}^E values reported by Smith and Welsh⁵ (see Appendix B).^{*} The results from these calculations, along with Graham's uniaxial strain calculations, are shown in Table C-2. The deviations from uniaxial strain are small. However, as noted earlier, the contributions of the ε₄' term to the polarization are significant.

Using the transformations for e_{ij}', we can express equation (C-1) in terms of e_{ij} values for rotations about the X₁-axis. After some algebraic manipulation, it can be shown that

$$\begin{aligned}
 P_2' = & e_{22} (c^3 \epsilon_2' - c^2 s \epsilon_4') + e_{33} (s^3 \epsilon_2' + cs^2 \epsilon_4') \\
 & + e_{31} (c^2 s \epsilon_2' - cs^2 \epsilon_4') + e_{15} (2c^2 s \epsilon_2' + c^3 \epsilon_4' - cs^2 \epsilon_4')
 \end{aligned}
 \tag{C-1}$$

where $c = \cos \theta$, $s = \sin \theta$, and θ is the angle of rotation about the X₁-axis. For Y-cut ($\theta = 0^\circ$) and Z-cut ($\theta = 90^\circ$) crystals, equation (C-1) is considerably simpler,

$$\begin{aligned}
 \text{Y-cut LiNbO}_3: P_2' &= e_{22} \epsilon_2' + e_{15} \epsilon_4' \\
 \text{Z-cut LiNbO}_3: P_2' &= e_{33} \epsilon_2'
 \end{aligned}
 \tag{C-2}$$

*When the C_{ij}^D values from Warner et al. were used, the calculated stresses and strains were close, as indicated in Table C-2.

Table C.2. Numerical simulation of Graham's LiNbO_3 data.^{a, b}

Experiment No.	Impact Velocity (m/s)	Impactor	Gage Type	Strains			Stresses (GPa)			Particle Velocities (m/s)		
				ϵ_2^i	ϵ_4^i	ϵ_6^i	σ_2^i	σ_4^i	σ_6^i	u_2^i	u_3^i	u_1^i
Q-1056	47.24	X-cut quartz	Y-cut	-2.24 x 10 ⁻³ (-2.21 x 10 ⁻³)	2.8 x 10 ⁻⁴	9.74 x 10 ⁻⁶	-0.485 (-0.486)	-0.638 x 10 ⁻²	0.857 x 10 ⁻³	15.28 (15.21)	-0.642	-0.0423
Q-1095	58.84	X-cut quartz	36° Y-cut	-2.38 x 10 ⁻³ (-2.47 x 10 ⁻³)	2.1 x 10 ⁻⁴	7.9 x 10 ⁻⁶	-0.623 (0.616)	-0.463 x 10 ⁻²	0.605 x 10 ⁻³	17.84 (18.12)	-0.466	-0.0321
Q-1056	47.24	X-cut quartz	Y-cut	-2.24 x 10 ⁻³	2.86 x 10 ⁻⁴	9.6 x 10 ⁻⁶	-0.486	-0.647 x 10 ⁻²	0.874 x 10 ⁻³	15.27	-0.651	-0.0425

^aThe first two calculations in the table are based on the C_{ij}^D values calculated from the data of Smith and Melah.⁵ For comparison, a third calculation, based on the C_{ij}^D values of Warner et al.⁴ is shown. The two sets of constants give comparable results.

^bThe values in parentheses are Graham's σ_6^i values based on a uniaxial strain approximation. Because of this approximation, the other stresses, strains, and particle velocities are zero in his analysis.

For other orientations, we have to consider all the terms in equation (C-1).

Using the strain values from Table C-2, the value of $e_{31} = 0.23$ C/m² from Smith and Welsh,⁵ and $e_{33} = 1.80$ C/m² from Graham's work,⁶ we can write the polarization for the two orientations as follows:

$$\text{Y-Cut (Q-1056): } 2.24 e_{22} - 0.28 e_{15} = 5.26 \text{ C/m}^2 \quad (\text{C-3})$$

$$36^\circ\text{-Rotated Y-Cut (Q-1095): } 0.99 + 1.34 e_{22} + 1.78 e_{15} = 11.47 \text{ C/m}^2$$

As indicated earlier, the polarization values on the right side of these equations represent an averaging over six experiments for each orientation. Thus, there are small differences between these polarization values and those reported in Graham's paper for these two shots. Solving the equations for e_{15} and e_{22} gives

$$\begin{aligned} e_{15} &= 3.76 \text{ C/m}^2 \\ e_{22} &= 2.82 \text{ C/m}^2 \end{aligned} \quad (\text{C-4})$$

The e_{15} value is identical to that of Smith and Welsh⁵ and is less than 2 percent different from the value reported by Graham.⁶ However, the e_{22} value is considerably different from the value calculated by Graham.

Although we have results for both 163°-rotated and 165.5°-rotated Y-cut orientations, we made no attempt to calculate e_{31} or a complete set of constants using our experimental results in conjunction with Graham's data because the two sets of experiments used different types of gages.

The analysis of Graham's data⁶ described here suggests that the following values be used for the second-order piezoelectric stress constants of LiNbO_3 .*

$$e_{22} = 2.82 \text{ C/m}^2$$

$$e_{33} = 1.80 \text{ C/m}^2$$

$$e_{15} = 3.76 \text{ C/m}^2$$

$$e_{31} = 0.23 \text{ C/m}^2$$

For developing a shear stress gage, this new set of constants gives 160.5°-rotated Y-cut, rather than 163°-rotated Y-cut, as the optimal crystal orientation. This point is discussed further in Appendix D.

*Recall that the complexities in analyzing results for rotated-cut crystals discussed in Section 2.2 have been ignored.

APPENDIX D

TRANSFORMATION OF PIEZOELECTRIC CONSTANTS

This appendix describes a simple and convenient method for determining the crystallographic orientations best suited for piezoelectric gage applications. Although considerable information exists on piezoelectric constants along particular directions, the method presented here is more general and convenient for the applications of interest.

The piezoelectric stress coefficients (e_{ijk}) and the piezoelectric strain coefficients (d_{ijk}) are defined by¹⁹

$$P_i = e_{ijk} \epsilon_{jk} \quad (D-1)$$

$$P_i = d_{imn} \sigma_{mn} \quad (D-2)$$

where the piezoelectric stress and strain coefficients are related by

$$e_{ijk} = d_{ipq} C_{pqjk} \quad (D-3)$$

Because the piezoelectric constants are third-rank tensors, they are transformed as

$$e'_{ijk} = a_{ip} a_{jq} a_{kr} e_{pqr} \quad (D-4)$$

For the rotated Y-cut crystals (rotation about the crystallographic X-axis) used in our work, the rotation matrix can be written as*

*This matrix is compatible with the coordinate system used in the main text. It is obtained from equation (B-19) by incrementing the indices of the coordinates in the manner given following equation (B-19).

$$a = \begin{bmatrix} 1 & 0 & 0 \\ 0 & \cos\theta & \sin\theta \\ 0 & -\sin\theta & \cos\theta \end{bmatrix} \quad (D-5)$$

For LiNbO_3 , combining (D-4) and (D-5) gives

$$e'_{22} = c^3 e_{22} + s^3 e_{33} + c^2 s (e_{31} + 2 e_{15}) \quad (D-6)$$

$$e'_{24} = -c^2 s e_{22} + (c^3 - c s^2) e_{15} + c s^2 (e_{33} - e_{31}) \quad (D-7)$$

where we have used the matrix notation; c and s denote $\cos\theta$ and $\sin\theta$, respectively.

To determine the optimal orientation for a shear gage we need to minimize the piezoelectric constant corresponding to the normal strain along that orientation and maximize the piezoelectric constant corresponding to the shear strain of interest. By using the numerical method outlined here, we can quickly determine the optimal orientation. Essentially, the method consists of implementing the transformations indicated in equations (D-3) and (D-4).

In defining the coordinate rotations for our work, we chose the Institute of Radio Engineers (IRE) conventions,³ instead of the usual solid angles. We numerically solved equations (B-1) and (B-2) for coordinate rotations between 0° and 180° about the crystallographic X-, Y-, or Z-axes. The numerical program has the following inputs.

- (1) The axis of rotation, denoted as 1, 2, or 3 for the crystallographic X-, Y-, or Z-axes, respectively.
- (2) The crystal type and the piezoelectric matrix (numerical values) in the crystallographic system.

The above input is used to determine the rotated constants as follows:

- (1) Change the piezoelectric constants from the matrix to tensor notation.

- (2) Construct the transformation matrices for the rotation angle.
- (3) Transform the piezoelectric tensor.
- (4) Convert the transformed tensor back to the matrix form.
- (5) Print out the angle of rotation and the transformed piezoelectric matrix.
- (6) Repeat the above steps for all desired angles.

The differences in converting e and d values from matrices to tensors and vice-versa are included.

The piezoelectric constant matrix for LiNbO_3 has the following form:

$$e_{ij} = \begin{bmatrix} 0 & 0 & 0 & 0 & e_{15} & -e_{22} \\ -e_{22} & e_{22} & 0 & e_{15} & 0 & 0 \\ e_{31} & e_{31} & e_{33} & 0 & 0 & 0 \end{bmatrix} \quad (\text{D-8})$$

As indicated in Appendix C, we initially used the piezoelectric constants cited by Smith and Welsh⁵ except for the e_{33} constant, which was taken from Graham's shock work.⁶ Of all the piezoelectric constants, the measurement of e_{33} from shock experiments is most reliable. Thus, the constants for the "old set" are

$$\begin{aligned} e_{22} &= 2.43 \text{ C/m}^2 \\ e_{33} &= 1.80 \text{ C/m}^2 \\ e_{15} &= 3.76 \text{ C/m}^2 \\ e_{31} &= 0.23 \text{ C/m}^2 \end{aligned} \quad (\text{D-9})$$

The e_{22} and e_{15} values are slightly different from Graham's values (see Table C-1).

Our examination of Graham's work indicated that some of his assumptions may not be valid. Hence, we reanalyzed his data as described in Appendix C. The "new set" of constants as calculated by the improved analysis have one significant difference: the value of e_{22} is 2.82 C/m^2 . The other constants were the same as indicated above.

As an example of the numerical procedure outlined in this Appendix, we show the piezoelectric stress matrix (e_{ij} values) for LiNbO_3 rotated about the crystallographic X-axis in Tables D-1 and D-2. The values shown are for the two sets of constants and for orientations between 162° Y-cut and 164° Y-cut. A scan of Table D-1 shows that, for gage thickness along the X_2' -axis, the constant e_{22}' is minimized for 163° Y-cut orientation. Small changes in orientation lead to significant changes in e_{22}' values. The e_{24}' value is relatively constant.

The new set of constants (only e_{22} is different) yield a significantly different value of e_{22}' for the 163° Y-cut orientation. The optimal direction using the new set of constants is the 160.5° Y-cut orientation with an e_{22}' value of $3.65 \times 10^{-3} \text{ C/m}^2$. These results highlight the need for an accurate determination of e_{22} .

Results shown in the two tables are useful in rapidly determining the effects of crystal orientation on the gage response. For example, the e_{24}' constant is relatively insensitive in contrast to the e_{22}' constant.

Table D.2. Transformed piezoelectric constants (C/m^2) for rotated Y-cut LiNbO₃ (new set).

162.1 DEGREE			
0.000E+00	0.000E+00	0.000E+00	3.473E+00
2.382E+00	1.229E-01	-1.515E-01	0.000E+00
5.228E-01	-3.576E-01	-2.318E+00	0.000E+00
162.3 DEGREE			
0.000E+00	0.000E+00	0.000E+00	3.463E+00
2.382E+00	1.017E-01	-1.793E+00	0.000E+00
5.238E-01	-3.630E-01	-2.313E+00	0.000E+00
162.5 DEGREE			
0.000E+00	0.000E+00	0.000E+00	3.453E+00
2.382E+00	7.440E-02	-1.777E+00	0.000E+00
5.155E-01	-3.683E-01	-2.301E+00	0.000E+00
162.7 DEGREE			
0.000E+00	0.000E+00	0.000E+00	3.443E+00
2.382E+00	4.701E-02	-1.759E+00	0.000E+00
5.072E-01	-3.734E-01	-2.290E+00	0.000E+00
162.9 DEGREE			
0.000E+00	0.000E+00	0.000E+00	3.433E+00
2.382E+00	1.954E-02	-1.741E+00	0.000E+00
4.989E-01	-3.784E-01	-2.279E+00	0.000E+00
163.1 DEGREE			
0.000E+00	0.000E+00	0.000E+00	3.423E+00
2.392E+00	8.001E-03	-1.722E+00	0.000E+00
4.905E-01	-3.833E-01	-2.268E+00	0.000E+00
163.3 DEGREE			
0.000E+00	0.000E+00	0.000E+00	3.413E+00
2.392E+00	-3.562E-02	-1.704E+00	0.000E+00
4.822E-01	-3.880E-01	-2.258E+00	0.000E+00
163.5 DEGREE			
0.000E+00	0.000E+00	0.000E+00	3.403E+00
2.392E+00	-6.831E-02	-1.685E+00	0.000E+00
4.738E-01	-3.926E-01	-2.247E+00	0.000E+00
163.7 DEGREE			
0.000E+00	0.000E+00	0.000E+00	3.393E+00
2.392E+00	-9.107E-02	-1.667E+00	0.000E+00
4.654E-01	-3.970E-01	-2.236E+00	0.000E+00
163.9 DEGREE			
0.000E+00	0.000E+00	0.000E+00	3.383E+00
2.392E+00	-1.189E-01	-1.648E+00	0.000E+00
4.571E-01	-4.013E-01	-2.226E+00	0.000E+00
164.1 DEGREE			
0.000E+00	0.000E+00	0.000E+00	3.373E+00
2.392E+00	-1.466E-01	-1.630E+00	0.000E+00
4.487E-01	-4.055E-01	-2.215E+00	0.000E+00
162.0 DEGREE			
0.000E+00	0.000E+00	0.000E+00	3.473E+00
2.382E+00	1.229E-01	-1.515E-01	0.000E+00
5.228E-01	-3.576E-01	-2.318E+00	0.000E+00
162.2 DEGREE			
0.000E+00	0.000E+00	0.000E+00	3.463E+00
2.382E+00	1.017E-01	-1.793E+00	0.000E+00
5.238E-01	-3.630E-01	-2.313E+00	0.000E+00
162.4 DEGREE			
0.000E+00	0.000E+00	0.000E+00	3.453E+00
2.382E+00	7.440E-02	-1.777E+00	0.000E+00
5.155E-01	-3.683E-01	-2.301E+00	0.000E+00
162.6 DEGREE			
0.000E+00	0.000E+00	0.000E+00	3.443E+00
2.382E+00	4.701E-02	-1.759E+00	0.000E+00
5.072E-01	-3.734E-01	-2.290E+00	0.000E+00
162.8 DEGREE			
0.000E+00	0.000E+00	0.000E+00	3.433E+00
2.382E+00	1.954E-02	-1.741E+00	0.000E+00
4.989E-01	-3.784E-01	-2.279E+00	0.000E+00
163.0 DEGREE			
0.000E+00	0.000E+00	0.000E+00	3.423E+00
2.392E+00	8.001E-03	-1.722E+00	0.000E+00
4.905E-01	-3.833E-01	-2.268E+00	0.000E+00
163.2 DEGREE			
0.000E+00	0.000E+00	0.000E+00	3.413E+00
2.392E+00	-3.562E-02	-1.704E+00	0.000E+00
4.822E-01	-3.880E-01	-2.258E+00	0.000E+00
163.4 DEGREE			
0.000E+00	0.000E+00	0.000E+00	3.403E+00
2.392E+00	-6.831E-02	-1.685E+00	0.000E+00
4.738E-01	-3.926E-01	-2.247E+00	0.000E+00
163.6 DEGREE			
0.000E+00	0.000E+00	0.000E+00	3.393E+00
2.392E+00	-9.107E-02	-1.667E+00	0.000E+00
4.654E-01	-3.970E-01	-2.236E+00	0.000E+00
163.8 DEGREE			
0.000E+00	0.000E+00	0.000E+00	3.383E+00
2.392E+00	-1.189E-01	-1.648E+00	0.000E+00
4.571E-01	-4.013E-01	-2.226E+00	0.000E+00
164.0 DEGREE			
0.000E+00	0.000E+00	0.000E+00	3.373E+00
2.392E+00	-1.466E-01	-1.630E+00	0.000E+00
4.487E-01	-4.055E-01	-2.215E+00	0.000E+00

APPENDIX E

OBLIQUE IMPACT OF ELASTIC PLATES

In this Appendix we describe the theoretical analyses for evaluating the effects of impact tilt (or misalignment) on the results of our experiment. This analysis is not exact because the LiNbO_3 is treated as an isotropic solid. Nevertheless, it provides considerable insight into the effects of tilt. Figure E.1 shows the experimental configuration we analyzed. The notation used here is not consistent with that in the rest of the report. However, the notation, as defined here, is self-consistent. The X_1' -system is defined such that the X_1' -axis is normal to Plates 2 and 3. Plate 1 has a velocity v_0 along the positive X_1' -direction. The tilt angle, θ , is zero for an ideal impact.* The situation depicted in Figure E.1 is valid for both compression-only and combined compression and shear experiments; θ is a measure of the deviation from parallelism at the instant of impact. Hence, the initial inclination of the plates to the direction of projectile motion is immaterial.

As indicated in Section 3, not only is the tilt angle important in analyzing the results but so is the orientation of the line of contact relative to the X_1' axes. Angle ϕ^\dagger defined in Figure E.1 determines the orientation of this line. The X_1 -system shown in Figure E.1 is

*The angle θ defined here denotes a different physical quantity than that defined in Figure 2 of Section 3.

†The two angles ϕ defined here and in Figure 6 of Section 3 both denote the orientation of the line of contact, but they are given relative to differing axes of reference.

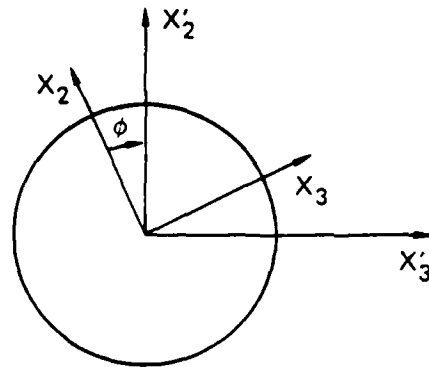
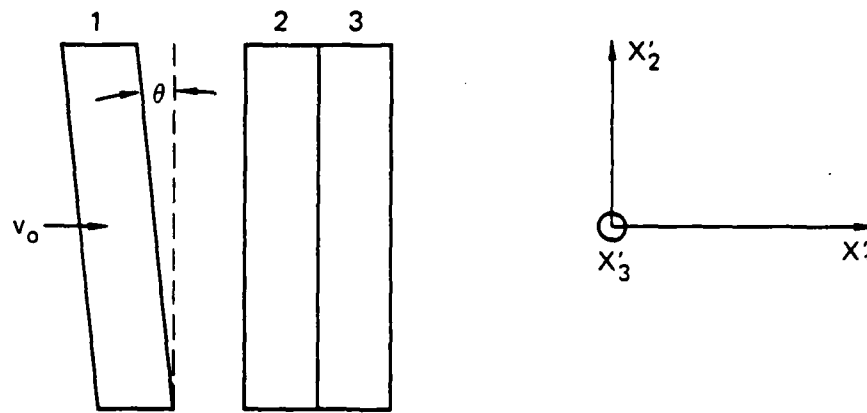


Figure E.1. Experimental configuration for evaluating tilt effects. (In the top figure, X'_3 is directed out of the plane of the figure. In the bottom figure, X'_1 is directed into the plane of the figure. Angle ϕ is counter-clockwise when looking from the positive X'_1 axis toward the origin. The X_1 - and the X'_1 -axes coincide.)

obtained by a counter-clockwise rotation through ϕ about the X_1' -axis when looking from the positive X_1' -axis (X_1 and X_1' coincide). The X_2 -axis is parallel to the direction in which the line of contact, traverses Plate 2. The X_1 -system is important because most of the analysis is performed for this system.

In our analyses we considered both "no slipping" and "complete slipping" at each of the two interfaces (between Plates 1 and 2 and between Plates 2 and 3). These represent the two extremes for conditions at these boundaries, and the extension to intermediate conditions is straightforward.

On impact of Plate 1 with Plate 2 two waves that propagate away from the interface are generated in each of the plates, as shown in Figure E.2. We have divided the analysis of the propagation of the two waves into Plates 2 and 3 into five parts: Part I analyzes the impact shown in Figure E.2; Part II analyzes the interaction of the compressional wave P(1) with the interface of Plate 2 and Plate 3; Part III analyzes the interaction of the shear wave S(2) with this interface; in Part IV, the stresses and particle velocities from the first three parts are summed in the X_1 -system; finally, in Part V, all the quantities are transformed to the X_1' -system.

Because of the numerous waves considered in the analysis, it is helpful to establish the nomenclature, then to review the general solution procedure.

E.1 NOMENCLATURE

D_{pi} = P-wave velocity in the i^{th} material

D_{si} = S-wave velocity in the i^{th} material

u_m = Normal particle velocity behind the m^{th} wave

v_m = Shear particle velocity behind the m^{th} wave

$Z_{pi} = \rho_i D_{pi}$ = Compression mechanical impedance for the i^{th} material

$Z_{si} = \rho_i D_{si}$ = Shear mechanical impedance for the i^{th} material

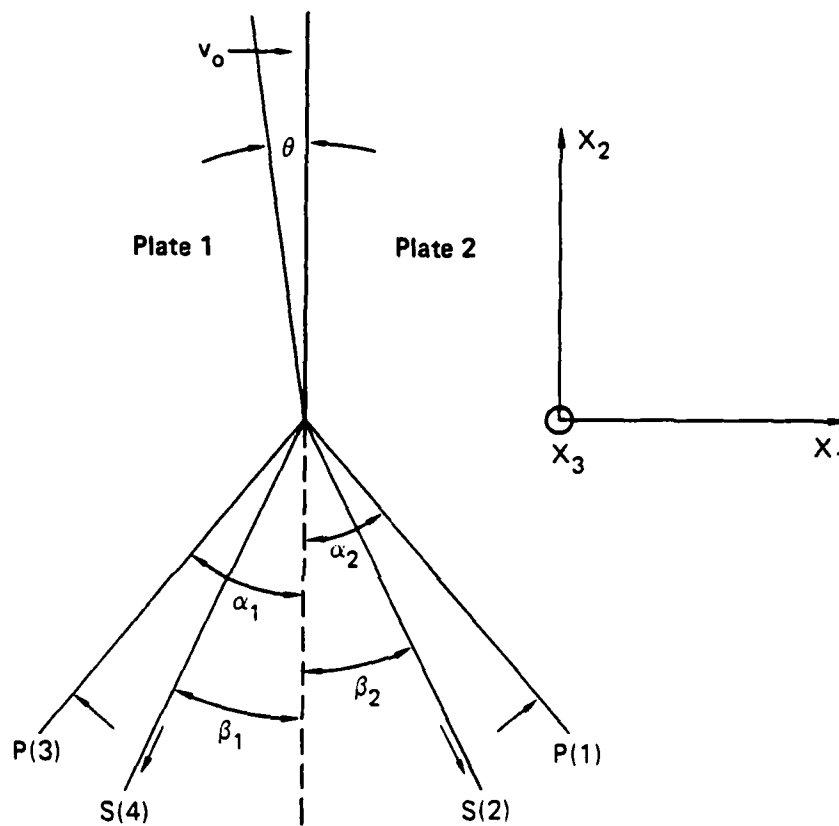


Figure E.2. Oblique impact of two elastic plates. (The four wave fronts generated upon impact are shown. The arrow behind a wave front represents the direction of particle motion caused by the particular wave.)

- α_i = Angle with the interface made by the P-wave in the i^{th} material
 β_i = Angle with the interface made by the S-wave in the i^{th} material
 λ_m = Normal stress behind the m^{th} wave; m is an odd number for P-waves
 ν_i = Poisson's ratio for the i^{th} material
 ρ_i = Density of the i^{th} material
 τ_m = Shear stress behind the m^{th} wave; m is an odd number for P-waves

Note, λ and u are unchanged by a shear wave, and τ and v are unchanged by a compression wave. The subscripts with λ and τ always identify the wave and do not imply the indices commonly used with the stress tensor.

E.2 SOLUTION PROCEDURE

The oblique impact shown in Figures E.1 and E.2 is analyzed using the attached-shock approximation. This approximation is valid for small tilt angles because the velocity of the point of contact is much larger than the wave velocities in the material*

$$v_c = \frac{v_o}{\tan\theta} \approx \frac{v_o}{\sin\theta} \quad (\text{E-1})$$

Two other approximations are used to simplify the mathematical analysis:† (1) the turning angle of the impact interface is neglected, as

* Even for the largest tilts in our experiments ($\theta \approx 0.1^\circ$), v_c is 116 mm/ μ s in contrast to a P-wave velocity of 3 mm/ μ s in PMMA.

† For the first part of the five-part analysis (given above) we analyzed a more general problem that avoids these assumptions. Because of the complexity of the equations, numerical results were not computed. However, the solution for the more general problem had no significant differences.

shown in Figure E.2, and (2) in choosing the S-wave velocity, we neglect the density changes behind the P-wave.

On impact, compression and shear waves are produced in both Plates 1 and 2. The inclination of these wave fronts can be written using Snell's law as

$$\frac{\sin\alpha_1}{D_{p1}} = \frac{\sin\beta_1}{D_{s1}} = \frac{\sin\alpha_2}{D_{p2}} = \frac{\sin\beta_2}{D_{s2}} = \frac{\sin\theta}{v_o} \quad (E-2)$$

The particle motion behind each wave is assumed to be that shown in Figure E.2. The choice of the particle motion directions is not important because these are determined from the final solution.

Throughout the discussion we use a right-handed coordinate system with the X_3 -axis coming out of the plane of Figure E.2. The coordinate systems needed for analyzing the flow behind each wave front are obtained by a counter-clockwise rotation of the X_1 -system about the X_3 -axis. Tensile stresses and strains are taken to be positive. The notation used for shear stresses and strains is compatible with this sign convention. The simplest procedure to ensure consistency of signs is to determine the signs using the flow equations and the definition of strain.

The solutions in the first three parts of the analysis are obtained by combining the linear elastic constitutive relations with the appropriate boundary conditions at each interface. In each part there are four unknowns,* and four boundary conditions are required to solve the problem. Two of these boundary conditions are common to all situations:

* Although there are several stresses and particle velocities, the problem always reduces to four unknowns because of the additional relations provided by the jump conditions and the constitutive equations.

- (1) The normal stress is continuous across the planar interface.
- (2) The normal particle velocity is continuous across the interface.

The two remaining boundary conditions depend on the frictional conditions assumed for the interface:

A. Complete Slipping

- (3) The tangential stress is zero along the interface in the first plate
- (4) The tangential stress is zero along the interface in the second plate

B. No Slipping

- (3) Tangential stress is continuous across the interface.
- (4) Tangential particle velocity is continuous across the interface.

C. Frictional Sliding

- (3) Tangential stress is continuous across the interface.
- (4) Tangential stress is related to the magnitude of the normal stress through a frictional law.

Here, we have analyzed only cases (A) and (B).

Note that a considerable amount of tedious algebra is involved in deriving the equations presented in this Appendix. For the sake of brevity, these derivations are not shown. The following relations were helpful in the algebraic manipulations. For each material, we can write

$$\frac{v}{1-v} = 1 - 2 \left(\frac{D_s}{D_p} \right)^2$$

$$\cos^2 \alpha + \frac{v}{1-v} \sin^2 \alpha = \cos 2\beta \quad (E-3)$$

$$\frac{2v-1}{2(1-v)} = - \left(\frac{D_s}{D_p} \right)^2$$

using the symbols defined in Subsection E.1.

E.3 IMPACT OF PLATES 1 AND 2 (PART I)

In this subsection we are concerned only with the four initial waves generated by the impact of Plate 1 with Plate 2, shown in Figure E.2. We developed the solution for this portion of the impact problem before we had settled on a consistent nomenclature. Thus, in this part of the analysis, the impact configuration we analyzed is slightly different from that shown in Figure E.2. This part of the analysis treats the flyer plate being tilted so that the four wave fronts in Figure E.2 are in the top half of the figure (A reflection about the X_1-X_3 plane in Figure E.2). Because the final result does not appear to depend on how the impact configuration is depicted in the problem, we have made no effort to rederive the relations leading to the results presented below.

E.3.1 Complete Slipping

The stresses and particle velocities behind each of the wave fronts and the flyer plate velocity are resolved parallel and perpendicular to the interface. For this case it is convenient to express the equations in terms of the stresses. Using a matrix representation, we can write these equations as

$$[A] \begin{bmatrix} \lambda_1 \\ \tau_2 \\ \lambda_3 \\ \tau_4 \end{bmatrix} = \begin{bmatrix} 0 \\ 0 \\ 0 \\ v_0 \end{bmatrix} \quad \begin{array}{l} \text{Tangential Stress Zero in Plate 2} \\ \text{Tangential Stress Zero in Plate 1} \\ \text{Normal Stress Continuous} \\ \text{Normal Velocity Continuous} \end{array} \quad (E-4)$$

here [A] is the 4 x 4 matrix

$$[A] = \begin{bmatrix} \frac{\sin 2\alpha_2}{\cos 2\beta_2} \frac{2v_2 - 1}{2 - 2v_2} & 1 & 0 & 0 \\ 0 & 0 & -\frac{\sin 2\alpha_1}{\cos \beta_1} \frac{2v_1 - 1}{2 - 2v_1} & 1 \\ \cos 2\beta_2 & \sin 2\beta_2 & -\cos 2\beta_1 & \sin 2\beta_1 \\ -\frac{\cos \alpha_2}{z_{p2}} & -\frac{\sin \beta_2}{z_{p2}} & -\frac{\cos \alpha_1}{z_{p1}} & \frac{\sin 2\beta_1}{z_{s1}} \end{bmatrix} \quad (E-5)$$

The boundary conditions that go with a particular equation are indicated in equation (E-4). Note that the indices for stress and particle velocity identify the wave, but the indices in the components of matrix [A] identify the plate.

In the coordinate system associated with each wave the stresses and particle velocities are related as follows:

$$\begin{aligned} \text{Plate 2: } \lambda_1 &= -z_{p2} u_1 \\ \tau_2 &= -z_{s2} v_2 \\ \text{Plate 1: } \lambda_3 &= -z_{p1} u_3 \\ \tau_4 &= z_{s1} v_4 \end{aligned} \quad (E-6)$$

In these equations, the particle velocities are to be taken as absolute quantities. Each of the above stresses refers to the stress immediately behind the particular wave.

The set of equations represented in equation (E-4) can be solved to determine the four stresses. These, in turn, can be used to determine the particle velocities from equation (E-6).

E.3.2 No Slipping

As before, the stresses and particle velocities are resolved along the interface. Because the tangential stresses are not zero on both sides, the equations are not as easily uncoupled. In the matrix representation we have

$$[A] \begin{bmatrix} \lambda_1 \\ \tau_2 \\ \lambda_3 \\ \tau_4 \end{bmatrix} = \begin{bmatrix} 0 \\ 0 \\ 0 \\ v_0 \end{bmatrix} \quad \begin{array}{l} \text{Tangential Stress Continuous} \\ \text{Normal Stress Continuous} \\ \text{Tangential Velocity Continuous} \\ \text{Normal Velocity Continuous} \end{array} \quad (E-7)$$

where the matrix [A] takes the form

$$[A] = \begin{bmatrix} \sin 2\alpha_2 \frac{2\nu_2 - 1}{2 - 2\nu_2} & \cos 2\beta_2 & \sin 2\alpha_1 \frac{2\nu_1 - 1}{2 - 2\nu_1} & -\cos 2\beta_1 \\ \cos 2\beta_2 & \sin 2\beta_2 & -\cos 2\beta_1 & \sin 2\beta_1 \\ \frac{\sin \alpha_2}{z_{p2}} & -\frac{\cos \beta_2}{z_{s2}} & -\frac{\sin \alpha_1}{z_{p1}} & -\frac{\cos \beta_1}{z_{s1}} \\ -\frac{\cos \alpha_2}{z_{p2}} & -\frac{\sin \beta_2}{z_{s2}} & -\frac{\cos \alpha_1}{z_{p1}} & \frac{\sin \beta_1}{z_{s1}} \end{bmatrix} \quad (E-8)$$

Once the stresses are known, the particle velocities can be calculated from the jump conditions indicated in equation (E-6).

E.3.3 Results

To gain some insight into the effects of tilt in our problem, consider the following example:^{*}

$$\text{PMMA: } \rho_0 = 1.185 \text{ g/cm}^3, D_p = 3 \text{ mm}/\mu\text{s}, D_s = 1.51 \text{ mm}/\mu\text{s} \quad (\text{E-9})$$

$$\text{LiNbO}_3: \rho_0 = 4.64 \text{ g/cm}^3, D_p = 6.75 \text{ mm}/\mu\text{s}, D_s = 4.61 \text{ mm}/\mu\text{s}$$

We assume the following representative values

$$v_0 = 0.15 \text{ mm}/\mu\text{s}, \theta = 2 \times 10^{-3} \text{ radian} \quad (\text{E-10})$$

Although LiNbO_3 is not an isotropic solid, we treated it as such and used the wave velocities pertinent to the crystal orientation of interest in our work. The results are as follows:

<u>Stress</u>	<u>Complete Slipping</u>	<u>No Slipping</u>	
λ_1	-4.775 kbar	-4.776 kbar	
λ_3	-4.778 kbar	-4.778 kbar	(E-11)
τ_2	-0.4 kbar	-0.395 kbar	
τ_4	0.097 kbar	0.105 kbar	

$$\alpha_1 = 2.29^\circ, \beta_1 = 1.15^\circ, \alpha_2 = 5.16^\circ, \beta_2 = 3.5^\circ$$

From these results we draw the following conclusions:

- (1) The solution for the slipping or no-slipping cases are nearly identical.[†] A significant amount of shear stress can be generated even for small tilt angles.

^{*}This does not match the experimental configuration treated in our work.

[†]Fowles³⁰ reported a similar result earlier.

- (2) The normal stress values are very close to the values predicted for $\theta = 0^\circ$. To a first approximation, compression stress behind the P-waves is independent of θ .
- (3) To a first approximation, the magnitude of the shear stress depends only on θ and is independent of v_0 .
- (4) At least for the complete slipping case, the direction of the shear motion can be specified a priori without solving the entire problem. The directions indicated in Figure E.2 are correct.

E.4 P-WAVE INCIDENT ON THE INTERFACE BETWEEN PLATES 2 AND 3 (PART II)

The compression wave generated by the impact considered in the previous subsection, denoted as P(1) in Figure E.2, interacts with the interface of Plates 2 and 3. The four waves shown in Figure E.3 are produced by this interaction. The orientation of the normal to a particular wave front is again calculated using Snell's law; we found that equation (E-2) determines all the angles in the problem including those considered in Part III of the analysis. As before, we present the equations in the matrix representation without presenting all the algebraic manipulation.

E.4.1 Complete Slipping

The stresses and particle velocities are resolved along the interface.

$$[A] \begin{bmatrix} \lambda_7 \\ \tau_8 \\ \lambda_5 \\ \tau_6 \end{bmatrix} = \begin{bmatrix} -\lambda_1 \cos 2\beta_2 \\ -\lambda_1 \left(\frac{D_{s2}}{D_{p2}} \right)^2 \sin 2\alpha_2 \\ 0 \\ \frac{\lambda_1}{Z_{p2}} \cos \alpha_2 \end{bmatrix} \begin{array}{l} \text{Normal Stress Continuous} \\ \text{Tangential Stress Zero in Plate 2} \\ \text{Tangential Stress Zero in Plate 3} \\ \text{Normal Velocity Continuous} \end{array} \quad (E-12)$$

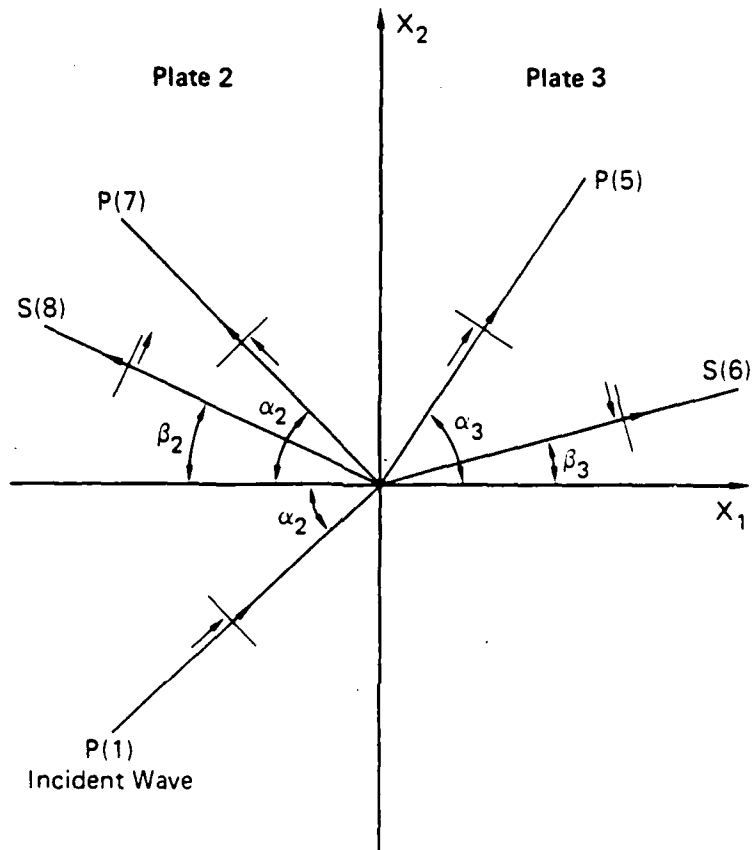


Figure E.3. P-wave interaction with the interface. [The normals to the wave fronts are shown with the wave fronts themselves indicated by the short line segments intersecting the normals. The arrow ahead of the wave front indicates the direction of wave propagation. The arrow behind the wave front indicates the direction of particle motion. The incident wave is the P(1) wave shown in Figure E.2.]

where the matrix [A] is given by

$$[A] = \begin{bmatrix} \cos 2\beta_2 & \sin 2\beta_2 & -\cos 2\beta_3 & \sin 2\beta_3 \\ -\left(\frac{D_{s2}}{D_{p2}}\right)^2 \sin 2\alpha_2 & \cos 2\beta_2 & 0 & 0 \\ 0 & 0 & \left(\frac{D_{s3}}{D_{p3}}\right)^2 \sin 2\alpha_3 & \cos 2\beta_3 \\ \frac{\cos \alpha_2}{Z_{p2}} & \frac{\sin \beta_2}{Z_{s2}} & \frac{\cos \alpha_3}{Z_{p3}} & -\frac{\sin \beta_3}{Z_{s3}} \end{bmatrix} \quad (E-13)$$

The stresses and particle velocities are related by

$$\begin{aligned} \text{Plate 2: } \lambda_1 &= -Z_{p2} u_1 \\ \lambda_7 &= -Z_{p2} u_7 \\ \tau_8 &= +Z_{s2} v_8 \\ \text{Plate 3: } \lambda_5 &= -Z_{p3} u_5 \\ \tau_6 &= +Z_{s3} v_6 \end{aligned} \quad (E-14)$$

As before, equation (E-12) is solved by determining $[A]^{-1}$ and multiplying the right side of equation (E-12) by it. The particle velocities are calculated from equation (E-14).

E.4.2 No Slipping

The equations for this case were written in terms of particle velocities

$$[A] \begin{bmatrix} u_7 \\ v_8 \\ u_5 \\ v_6 \end{bmatrix} = \begin{bmatrix} -u_1 \cos \alpha_2 \\ -u_1 \sin \alpha_2 \\ +Z_{p2} u_1 \cos 2\beta_2 \\ +Z_{s2} u_1 \frac{D_{s2}}{D_{p2}} \sin 2\alpha_2 \end{bmatrix} \begin{array}{l} \text{Normal Velocity Continuous} \\ \text{Tangential Velocity Continuous} \\ \text{Normal Stress Continuous} \\ \text{Tangential Stress Continuous} \end{array} \quad (E-15)$$

where [A] is given by

$$[A] = \begin{bmatrix} -\cos \alpha_2 & \sin \beta_2 & -\cos \alpha_3 & -\sin \beta_3 \\ \sin \alpha_2 & \cos \beta_2 & -\sin \alpha_3 & \cos \beta_3 \\ -Z_{p2} \cos 2\beta_2 & Z_{s2} \sin 2\beta_2 & Z_{p3} \cos 2\beta_3 & Z_{s3} \sin 2\beta_3 \\ Z_{s2} \frac{D_{s2}}{D_{p2}} \sin 2\alpha_2 & Z_{s2} \cos 2\beta_2 & Z_{s3} \frac{D_{s3}}{D_{p3}} \sin 2\alpha_3 & -Z_{s3} \cos 2\beta_3 \end{bmatrix} \quad (E-16)$$

Multiplying both sides of Equation (E-15) by $[A]^{-1}$, we obtain u_7 , v_8 , u_5 , and v_6 in terms of u_1 . The stresses corresponding to these particle velocities can be calculated using the jump conditions in equation (E-14).

E.5 S-WAVE INCIDENT ON THE INTERFACE BETWEEN PLATES 2 AND 3 (PART III)

Figure E.4 shows the reflection and transmission of the shear wave, denoted as S(2) in Subsection E.3, from the interface between Plates 2 and 3. In accordance with the approximations set forth in Subsection E.2, the four waves generated at the interface by S(2) are taken to have the same propagation direction as the waves generated by P(1) shown in Figure E.3. This procedure simplifies the derivation of

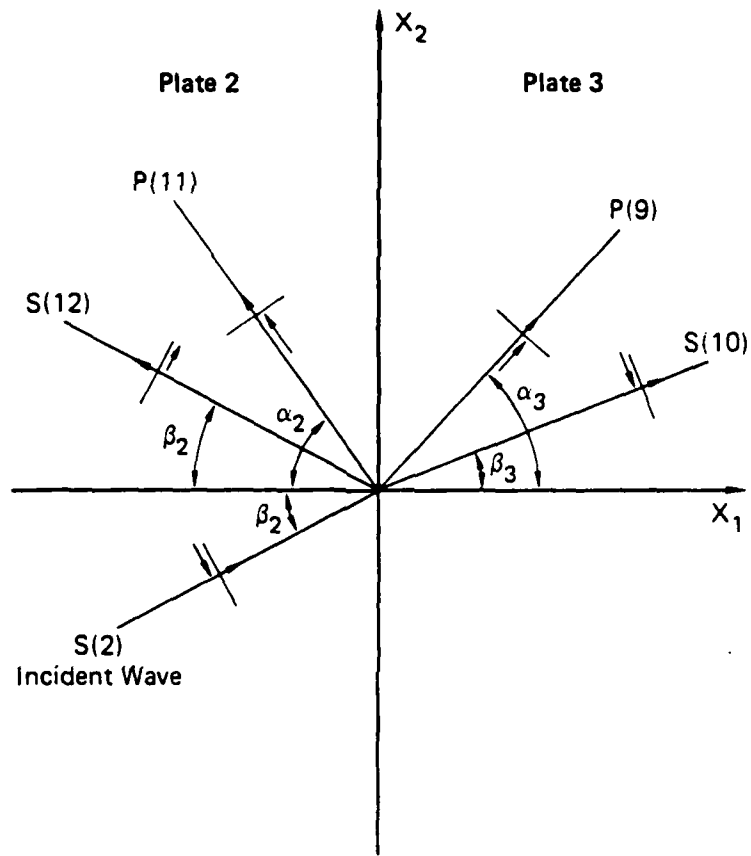


Figure E.4. S-wave interaction with the interface. [The normals to the wave fronts are shown with the wave fronts themselves indicated by the short line segments intersecting the normals. The arrow ahead of the wave front indicates the direction of wave propagation. The arrow behind the wave front indicates the direction of particle motion. The incident wave is the S(2) wave shown in Figure E.2.]

the equations. The angles made by the wave front normals will be the same as in Subsection E.4.

Except for the contributions from the incident wave, the other terms can be written directly from Subsection E.4 by incrementing the wave identification numbers by 4. Because the plates are the same as those in subsection E.4, the [A] matrices will also be the same.

E.5.1 Complete Slipping

The four equations for this case are

$$[A] \begin{bmatrix} \lambda_{11} \\ \tau_{12} \\ \lambda_9 \\ \tau_{10} \end{bmatrix} = \begin{bmatrix} \tau_2 \sin 2\beta_2 \\ -\tau_2 \cos 2\beta_2 \\ 0 \\ -\frac{\tau_2}{Z_{s2}} \sin \beta_2 \end{bmatrix} \begin{array}{l} \text{Normal Stress Continuous} \\ \text{Tangential Stress Zero in Plate 2} \\ \text{Tangential Stress Zero in Plate 3} \\ \text{Normal Velocity Continuous} \end{array} \quad (E-17)$$

where the A matrix is given by equation (E-13).

The jump conditions are given by substituting

$$\tau_2 = Z_{s2} v_2 \quad (E-18)$$

for the relation involving λ_1 in equation (E-14). The wave identification subscripts for the other four equations are to be incremented by 4 to conform to Figure E.4.

E.5.2 No Slipping

The equations for this case are

$$[A] \begin{bmatrix} u_{11} \\ v_{12} \\ u_9 \\ v_{10} \end{bmatrix} = \begin{bmatrix} -v_2 \sin \beta_2 \\ v_2 \cos \beta_2 \\ Z_{s2} v_2 \sin 2\beta_2 \\ -Z_{s2} v_2 \cos 2\beta_2 \end{bmatrix} \begin{array}{l} \text{Normal Velocity Continuous} \\ \text{Tangential Velocity Continuous} \\ \text{Normal Stress Continuous} \\ \text{Tangential Stress Continuous} \end{array} \quad (E-19)$$

where [A] is given by equation (E-16). The stresses are determined from the particle velocities using equation (E-18) and the procedure indicated above.

E.6 STRESSES AND PARTICLE VELOCITIES IN THE X_1 -SYSTEM (PART IV)

In this part, the stresses and particle velocities from the previous parts are resolved and added in the X_1 -system. Because we are interested in the gage response, we restrict our calculations to Plate 3. At the end of Part I of this analysis, the stresses and particle velocities in Plate 3 are zero. Hence, in calculating the response of Plate 3 we are concerned only with Parts II and III of this analysis. As before, only the results are presented.

We use σ_{ij} to denote stresses and w_m to denote particle velocities in the X_1 -system.

E.6.1 Part II Contributions

The P(5) wave is resolved in the X_1 -system using a clockwise rotation through α_3 about the X_3 -axis. The rotation matrix is

$$P(5) \text{ Rotation Matrix} = \begin{bmatrix} \cos\alpha_3 & -\sin\alpha_3 & 0 \\ \sin\alpha_3 & \cos\alpha_3 & 0 \\ 0 & 0 & 1 \end{bmatrix} \quad (E-20)$$

The S(6) wave is resolved using a clockwise rotation through β_3 about the X_3 -axis. The rotation matrix has the same form as the one above with β_3 is substituted for α_3 .

The components of the stresses and particle velocities existing at the end of Part II of this analysis are obtained by summing up the contributions from the resolved P(5) and S(6) waves. Thus, in the X_1 -system the stresses are

$$\begin{aligned}
\sigma_{11} &= \lambda_5 \cos 2\beta_3 - \tau_6 \sin 2\beta_3 \\
\sigma_{22} &= \lambda_5 (\sin^2 \alpha_3 + Q_3 \cos^2 \alpha_3) + \tau_6 \sin 2\beta_3 \\
\sigma_{33} &= Q_3 \lambda_5 \\
\sigma_{12} = \sigma_{21} &= -\frac{1}{2} (Q_3 - 1) \lambda_5 \sin 2\alpha_3 + \tau_6 \cos 2\beta_3
\end{aligned} \tag{E-21}$$

where

$$Q_3 = \frac{v_3}{1 - v_3}$$

The particle velocities are given by

$$\begin{aligned}
w_1 &= u_5 \cos \alpha_3 + v_6 \sin \beta_3 \\
w_2 &= u_5 \sin \alpha_3 - v_6 \cos \beta_3 \\
w_3 &= 0
\end{aligned} \tag{E-22}$$

In these equations the u_i , v_i , λ_i , and τ_i refer to the coordinate system associated with the i^{th} wave.

E.6.2 Part III Contributions

Because waves P(9) and S(10) have the same orientation as P(5) and S(6), respectively, the rotation matrices resolving each of them in the X_i -system are those used above. The expressions for the components of σ_{ij} and w_m existing at the end of Part III of this analysis are obtained by incrementing by 4 the wave identification subscripts, appearing on the variables u_i , v_i , λ_i , and τ_i , in Eqs. (E-21) and (E-22).

E.6.3 Total Contributions Existing at the End of Part III

The total stresses and particle velocities in the X_1 -system are

$$\begin{aligned}
 \sigma_{11} &= \cos 2\beta_3(\lambda_5 + \lambda_9) - \sin 2\beta_3(\tau_6 + \tau_{10}) \\
 \sigma_{22} &= (\sin^2 \alpha_3 + Q_3 \cos^2 \alpha_3)(\lambda_5 + \lambda_9) + \sin 2\beta_3(\tau_6 + \tau_{10}) \\
 \sigma_{33} &= Q_3(\lambda_5 + \lambda_9) \\
 \sigma_{12} = \sigma_{21} &= -\frac{1}{2}(Q_3 - 1)(\lambda_5 + \lambda_9)\sin 2\alpha_3 + (\tau_6 + \tau_{10})\cos 2\beta_3 \\
 \sigma_{13} = \sigma_{31} &= 0 \\
 \sigma_{23} = \sigma_{32} &= 0
 \end{aligned} \tag{E-23}$$

$$\begin{aligned}
 w_1 &= \cos \alpha_3(u_5 + u_9) + \sin \beta_3(v_6 + v_{10}) \\
 w_2 &= \sin \alpha_3(u_5 + v_9) - \cos \beta_3(v_6 + v_{10}) \\
 w_3 &= 0
 \end{aligned} \tag{E-24}$$

with Q as defined above.

E.7 STRESSES AND PARTICLE VELOCITIES IN THE X_1' -SYSTEM (PART V)

Finally, the stresses and particle velocities are transformed to the X_1' -system indicated in Figure E.1. To go from the X_1 -system to the X_1' -system involves a counter-clockwise rotation through the angle ϕ about the X_1 -axis (looking at origin from the positive X_1 -axis). The rotation matrix is given by

$$a_{ij} = \begin{bmatrix} 1 & 0 & 0 \\ 0 & \cos \phi & \sin \phi \\ 0 & -\sin \phi & \cos \phi \end{bmatrix} \tag{E-25}$$

The stresses and particle velocities in the X_1' -system are

$$\sigma_{ij}' = a_{im} a_{jn} \sigma_{mn} \tag{E-26}$$

$$w_m' = a_{mn} w_n \tag{E-27}$$

where the σ_{mn} and w_n are given in equations (E-23) and (E-24), respectively.

We developed a program called ELPLAT* to implement the steps outlined in this Appendix; the program closely matches the calculation sequence indicated here. The input to this program consists of specifying the densities and elastic wave velocities for each of the three plates, the flyer plate velocity v_0 along the X_1 -axis, the angles θ and ϕ , and the slipping condition at each interfaces. Actually, only the second interface condition is important because the solution in Part I is independent of the interface condition.

The analysis presented here is not exact for our experiments because Plate 3 (LiNbO_3) is treated as an isotropic solid. Despite this limitation, an assessment of the tilt effects on the particular compression and shear stresses of interest can be ascertained. However, the contribution to the other stresses cannot be determined. We have performed preliminary work to extend our analysis to anisotropic plates. This will be completed in a future study.

In the theoretical analysis presented in this Appendix, time is not included as a variable. Comparisons with time-resolved measurements will require a determination of the wave transit times through Plate 2. When calculating these times, it is important to account for the wave fronts not being parallel to the interfaces.

*The author is grateful to T. Radzekewicz for his assistance in writing the program. A copy of this program is available from the author.

APPENDIX F

DETAILS OF MEASURED WAVE PROFILES

Details of the voltage- or current-time profiles from the different experiments are presented here. The experimental parameters corresponding to these profiles are listed in Tables 1 and 2 of Section 3.

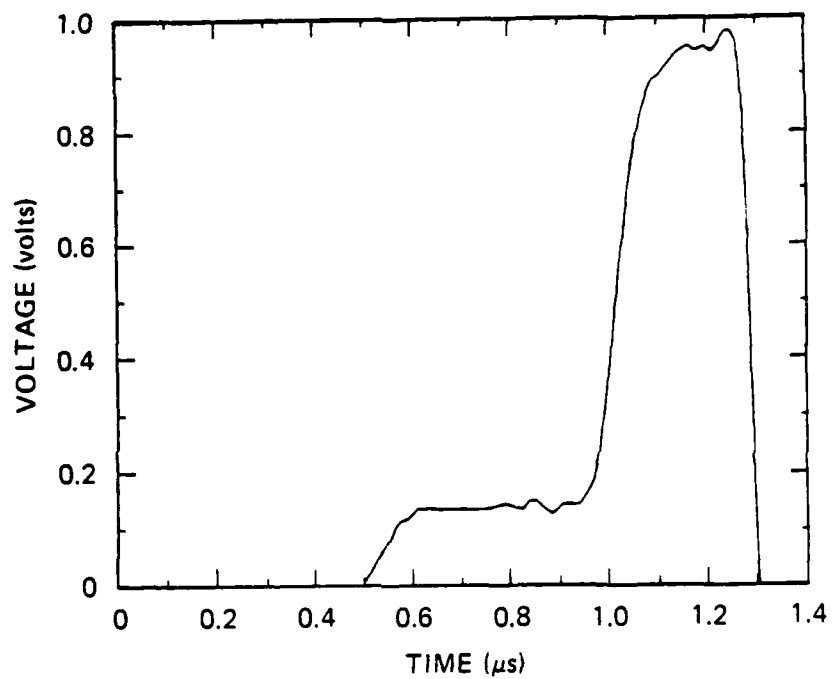
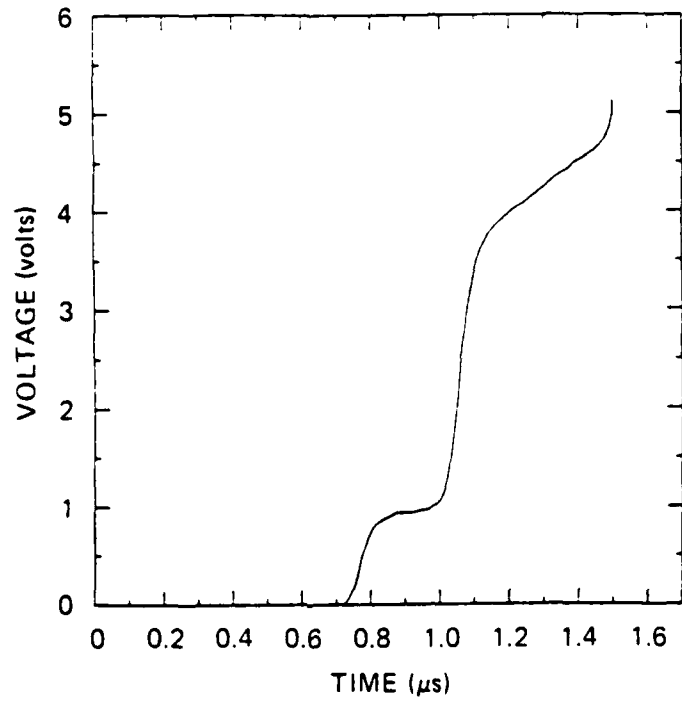
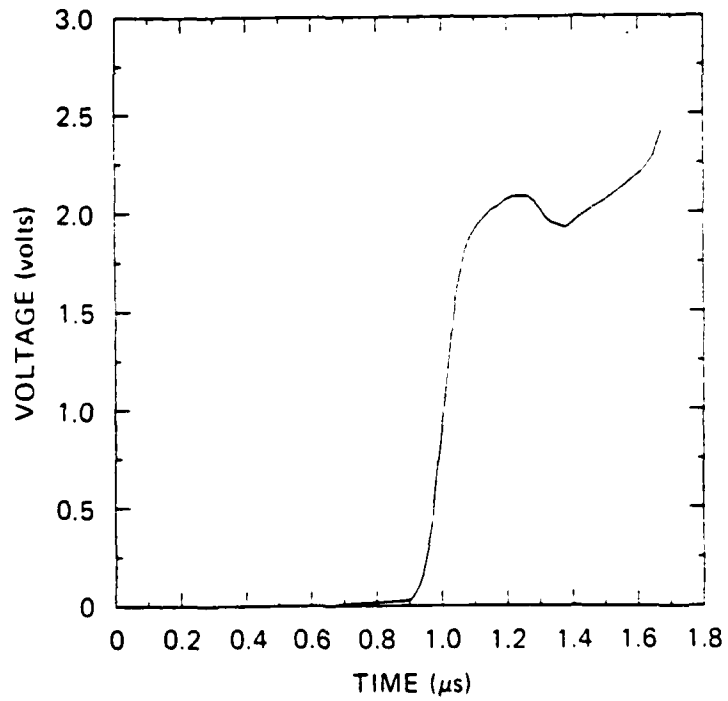


Figure F.1. Voltage-time profile for experiment 1 (78-2-46).
[163° Y-cut ($Z' = 0^\circ$)].

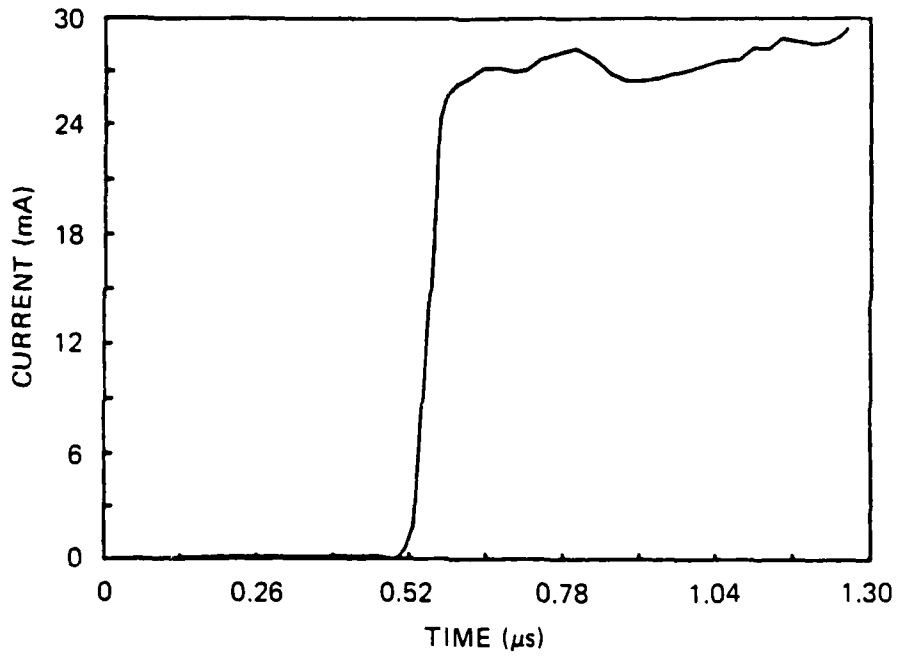


(a) 163° Y-Cut ($Z' = 0^\circ$)

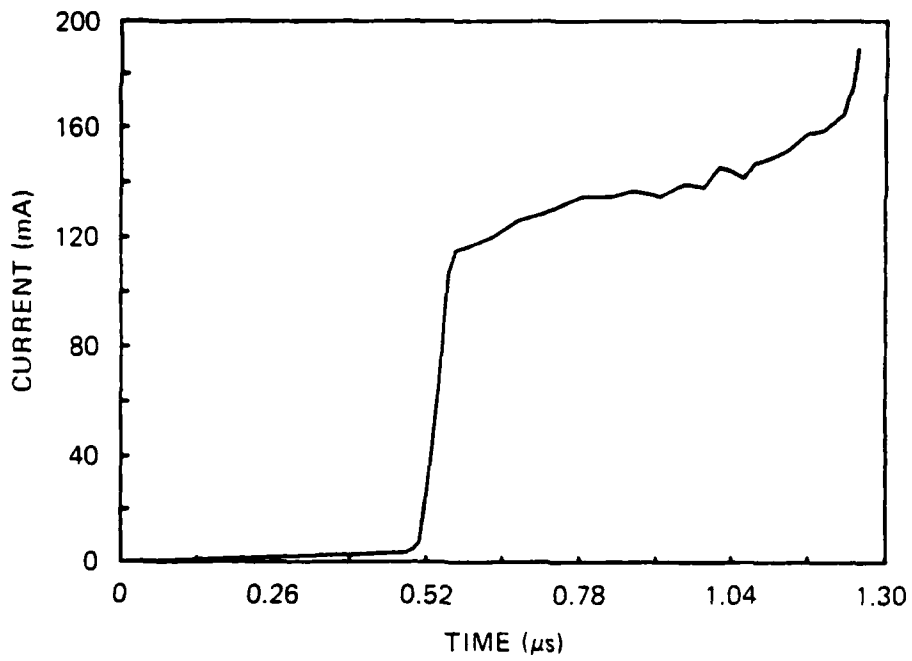


(b) 163° Y-Cut ($Z' = 90^\circ$)

Figure F.2. Voltage-time profiles for experiment 2 (81-2-15).

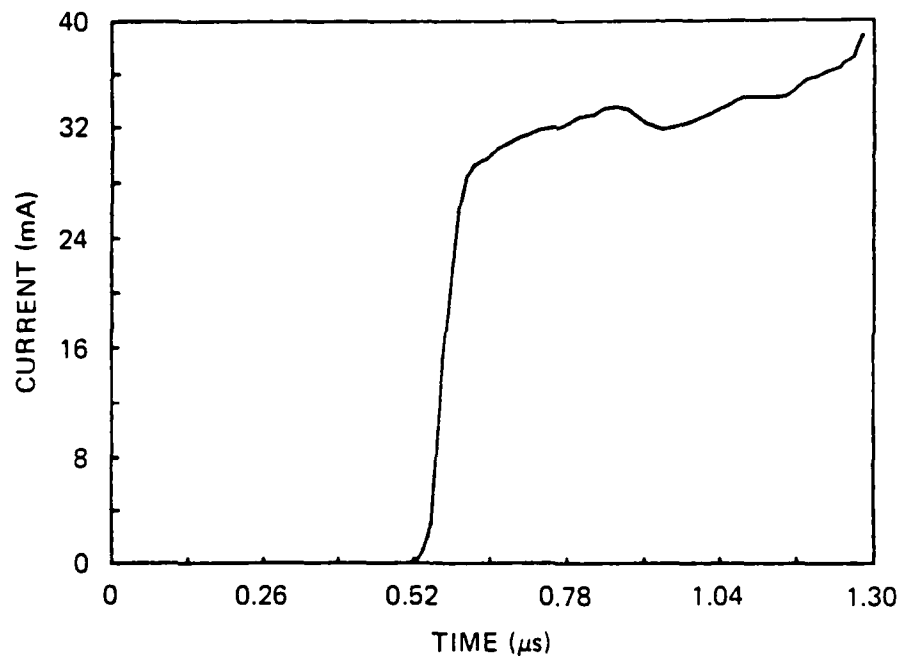


(a) 163° Y-Cut ($Z' = 0^\circ$)

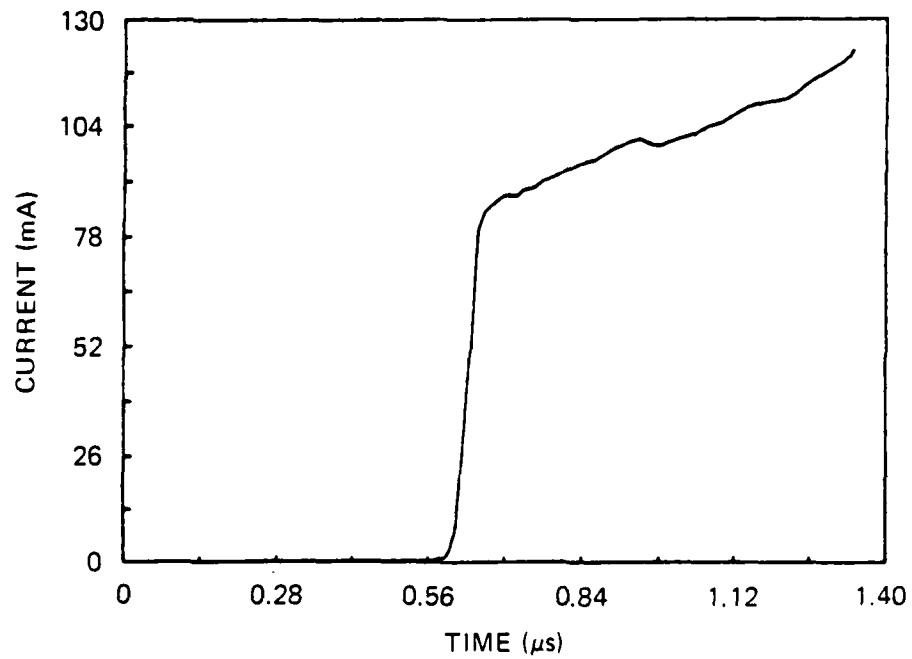


(b) 165.5° Y-Cut ($Z' = 0^\circ$)

Figure F.3. Current-time profiles for experiment 3 (81-2-22).

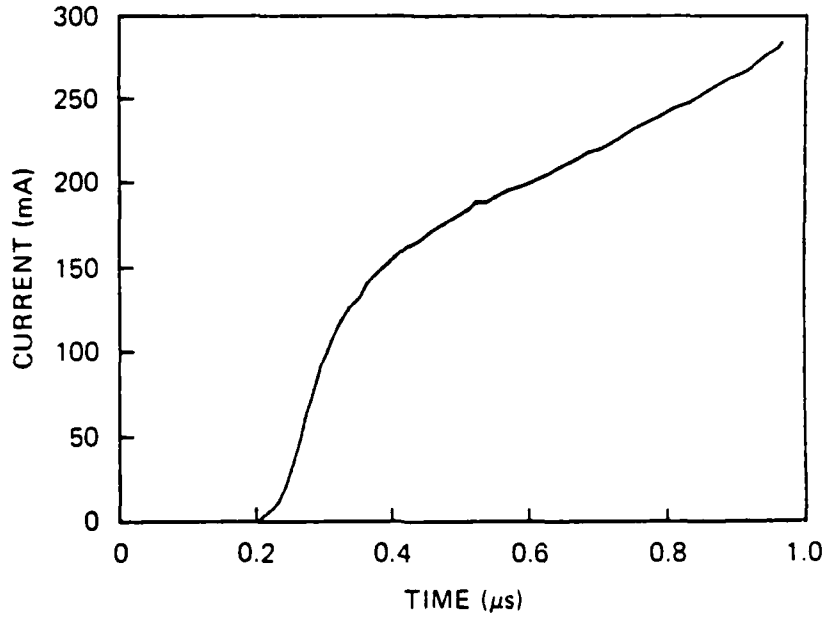


(a) 163° Y-Cut ($Z' = 0^\circ$)

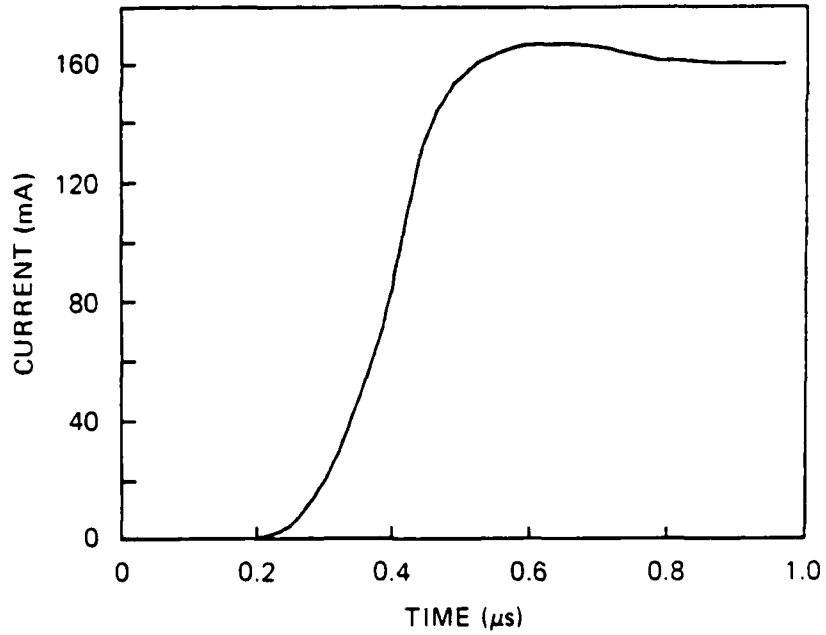


(b) 165.5° Y-Cut ($Z' = 0^\circ$)

Figure F.4. Current-time profiles for experiment 4 (81-2-23).



(a) 165.5° Y-Cut ($Z' = 0^\circ$)



(b) 165.5° Y-Cut ($Z' = 90^\circ$)

Figure F.5. Current-time profiles for experiment 6 (81-2-43).

DISTRIBUTION LIST

DEPARTMENT OF DEFENSE

ASST TO THE SECY OF DEFENSE ATOMIC ENERGY
ATTN: EXECUTIVE ASSISTANT

DEFENSE INTELLIGENCE AGENCY
ATTN: RTS-2B

DEFENSE NUCLEAR AGENCY
2 CYS ATTN: SPSS
ATTN: SPTD
4 CYS ATTN: STTI-CA

DEFENSE TECHNICAL INFORMATION CENTER
12 CYS ATTN: DD

FIELD COMMAND DNA DET 2
LAWRENCE LIVERMORE NATIONAL LAB
ATTN: FC-1

FIELD COMMAND DEFENSE NUCLEAR AGENCY
ATTN: FCT
ATTN: FCTT
ATTN: FCTT W SUMMA
ATTN: FCTXE

UNDER SECY OF DEF FOR RSCH & ENGRG
ATTN: STRAT & SPACE SYS (OS)

DEPARTMENT OF THE ARMY

HARRY DIAMOND LABORATORIES
ATTN: SCHLD-NW-P

U S ARMY BALLISTIC RESEARCH LAB
ATTN: SLCBR-SS-T TECH LIB

U S ARMY COLD REGION RES ENGR LAB
ATTN: CRREL-EM

U S ARMY ENGR WATERWAYS EXPR STATION
ATTN: D DAY WESSE
ATTN: G P BONNER WESJV-Z
ATTN: J INGRAM WESSER
ATTN: TECHNICAL LIBRARY

U S ARMY MATERIAL COMMAND
ATTN: DRXAM-TL TECH LIB

U S ARMY NUCLEAR & CHEMICAL AGENCY
ATTN: LIBRARY

US ARMY WHITE SANDS MISSILE RANGE
ATTN: STEWS-TE-N K CUMMINGS

DEPARTMENT OF THE NAVY

DAVID TAYLOR NAVAL SHIP R & D CTR
ATTN: CODE 1770
ATTN: TECH INFO CTR CODE 522.1

DEPARTMENT OF THE AIR FORCE

AIR FORCE IS/INT
ATTN: INT

AIR FORCE INSTITUTE OF TECHNOLOGY
ATTN: LIBRARY/AFIT/LDEE

AIR FORCE WEPABORATORY, AFSC
ATTN: NTE M PLAMONDON
ATTN: NTED J RENICK
ATTN: SUL

AIR UNIVERSITY LIBRARY
ATTN: AUL-LSE

BALLISTIC MISSILE OFFICE/DAA
2 CYS ATTN: ENSN

DEPARTMENT OF ENERGY

UNIVERSITY OF CALIFORNIA
LAWRENCE LIVERMORE NATIONAL LAB
ATTN: L-53 TECH INFO DEPT LIB

SANDIA NATIONAL LABORATORIES
ATTN: EDUC AND TECH LIB DIV

SANDIA NATIONAL LABORATORIES
ATTN: DIV 7111 B VORTMAN
ATTN: TECH LIB 3141 RPTS RCVG CLRK

OTHER GOVERNMENT

CENTRAL INTELLIGENCE AGENCY
ATTN: OSWR/NED

DEPARTMENT OF THE INTERIOR
ATTN: D RODDY

FEDERAL EMERGENCY MANAGEMENT AGENCY
ATTN: OFC OF RSCH/NP H TOVEY

DEPARTMENT OF DEFENSE CONTRACTORS

ACUREX CORP
ATTN: J SAPERSTEIN

DEPT OF DEFENSE CONTRACTORS (CONTINUED)

AEROSPACE CORP
ATTN: LIBRARY ACQ M1/199

APPLIED RESEARCH ASSOCIATES, INC
ATTN: D PIEPENBURG

APPLIED RESEARCH ASSOCIATES, INC
ATTN: R FRANK

BDM CORP
ATTN: A VITELLO
ATTN: CORPORATE LIB

CALIFORNIA RESEARCH & TECHNOLOGY, INC
ATTN: K KREYENHAGEN

CALIFORNIA RESEARCH & TECHNOLOGY, INC
ATTN: F SAUER

CUSHING ASSOCIATES, INC
ATTN: V CUSHING

DEVELCO, INC
ATTN: L RORDEN

GENERAL RESEARCH CORP
ATTN: E STEELE
ATTN: R PARISSÉ

GEO CENTERS, INC
ATTN: H LINNERUD
ATTN: L ISAACSON

H-TECH LABS, INC
ATTN: B HARTENBAUM

IIT RESEARCH INSTITUTE
ATTN: DOCUMENTS LIBRARY

KAMAN SCIENCES CORP
ATTN: LIBRARY

KAMAN TEMPO
ATTN: DASIAC

KAMAN TEMPO
ATTN: DASIAC

MERRITT CASES, INC
ATTN: J MERRITT
ATTN: LIBRARY

MITRE CORP
ATTN: J FREEDMAN

PACIFIC-SIERRA RESEARCH CORP
ATTN: H BRODE, CHAIRMAN SAGE

PHYSICS APPLICATIONS, INC
ATTN: DOCUMENT CONTROL

R & D ASSOCIATES
ATTN: J LEWIS
ATTN: TECH INFO CENTER

R & D ASSOCIATES
ATTN: G GANONG

RAND CORP
ATTN: P DAVIS

RAND CORP
ATTN: B BENNETT

S-CUBED
ATTN: D GRINE
ATTN: LIBRARY

SCIENCE & ENGRG ASSOC., INC
ATTN: B CHAMBERS

SCIENCE & ENGRG ASSOCIATES, INC
ATTN: J STOCKTON

SCIENCE APPLICATIONS INTL CORP
ATTN: K SITES

SCIENCE APPLICATIONS INTL CORP
ATTN: TECHNICAL LIBRARY

SCIENCE APPLICATIONS INTL CORP
ATTN: W LAYSON

SOUTHWEST RESEARCH INSTITUTE
ATTN: A WENZEL

SRI INTERNATIONAL
ATTN: D KEOUGH
ATTN: P DE CARLI

TELEDYNE BROWN ENGINEERING
ATTN: D ORMOND
ATTN: F LEOPARD

TERRA TEK, INC
ATTN: S GREEN

TRW ELECTRONICS & DEFENSE SECTOR
2 CYS ATTN: N LIPNER
ATTN: TECH INFO CTR DOC ACQ

TRW ELECTRONICS & DEFENSE SECTOR
ATTN: E WONG, BLDG SB1
ATTN: P DAI

WASHINGTON STATE UNIVERSITY
2 CYS ATTN: PHYSICS DEPT/Y M GUPTA

DEPT OF DEFENSE CONTRACTORS (CONTINUED)

**WEIDLINGER ASSOC, CONSULTING ENGRG
ATTN: J ISENBERG**

**WEIDLINGER ASSOC, CONSULTING ENGRG
ATTN: T DEEVY**

**WEIDLINGER ASSOC, CONSULTING ENGRG
ATTN: M BARON**

ENM

// - 86

DTIC